

THRUST SCALING IN APPLIED-FIELD
MAGNETOPLASMADYNAMIC THRUSTERS

WILLIAM J. COOGAN

A DISSERTATION
PRESENTED TO THE FACULTY
OF PRINCETON UNIVERSITY
IN CANDIDACY FOR THE DEGREE
OF DOCTOR OF PHILOSOPHY

RECOMMENDED FOR ACCEPTANCE
BY THE DEPARTMENT OF
MECHANICAL AND AEROSPACE ENGINEERING
ADVISER: PROFESSOR EDGAR Y. CHOUEIRI

SEPTEMBER 2018

© Copyright by William J. Coogan, 2018.

All rights reserved.

Abstract

A theoretical and experimental investigation of the scaling of thrust of applied-field magnetoplasmadynamic thrusters (AF-MPDTs) with geometric and operational parameters is undertaken. The thrust of an AF-MPDT consists of applied-field, gasdynamic, and self-field components. Because the first of these components is dominant under nominal operating conditions, and therefore most relevant to optimizing the performance of this thruster for a given mission’s requirements, the applied-field thrust component is the focus of this work.

In the canonical applied-field thrust model, the thrust coefficient, which is the ratio of the measured thrust to the modeled thrust, is assumed to be constant. It is shown in this work that there exists a governing “confinement parameter,” which represents the ratio of the inward to outward radial forces acting on the plasma, and which depends on the total current, applied magnetic field, mass flow rate, acoustic velocity at the anode throat, the ratio of specific heats, and the thruster geometry. It is shown that this parameter defines two different modes of operation, and that the thrust coefficient is only constant on the boundary between these two modes, where the confinement parameter is equal to one. When the confinement parameter is greater than unity, the inward radial forces are larger than the outward radial forces, and the plasma is in a magnetic-confinement mode. In this mode, the plasma is pinched inward from the anode wall, reducing the volume on which the Lorentz force acts to generate thrust. It is demonstrated, using data from the literature, that increasing the pinching forces in this mode of operation reduces the thrust.

When the confinement parameter is less than unity, the outward radial forces exceed the inward radial forces, and the plasma is in the anode-confinement mode. In this mode, it is demonstrated that, for a given thruster, the thrust coefficient depends solely on the confinement parameter. Increasing the confinement parameter decreases the plasma density near the anode wall and increases the density near the thrust axis,

which increases pressure on the tip of the cathode, and the rate of rotation of the plasma column. Both the increase in pressure, and the increase in azimuthal kinetic energy, result in increased applied-field thrust. The scaling of the thrust coefficient with the confinement parameter is demonstrated using measurements of total thrust for a number of thrusters in the literature. However, in order to demonstrate that this scaling is not affected by self-field or gasdynamic thrust components, a method for directly measuring the applied-field thrust component is devised and used to verify that the dependence is correct.

Acknowledgements

The work contained in this thesis would not have been possible without the support of others. I would like to first acknowledge my advisor, Professor Edgar Choueiri. Eddie, I have never met someone so ruthless in his pursuit of the truth as you are. Thank you for setting an example as a scientist, and for setting a high bar for the work of your students.

I would still be trying to get my thruster working if it weren't for the help of Bob Sorenson. Bob, you are among the most talented troubleshooters I have ever known. You taught me how to design, how to machine, and how to track down problems. You retired two years ago, but your lessons are still serving me well as an engineer and as a person.

Thank you to all of those who have spent hours on committee meetings and who have provided comments on this thesis. Professor Julia Mikhailova, Professor Sam Cohen, Professor Egemen Kolemen, Dr. Mikhail Schneider, and Dr. Dan Lev—your advice and guidance have been extraordinarily helpful. Danny, in particular, was always willing to take an emergency call in the middle of the night in Israel, and his work on the LiLFA prior to my arrival at PU saved me years of effort. Thank you for volunteering so much of your time.

My fellow EPPDyL students made numerous contributions to this thesis. Thank you all for your guidance and friendship. Justin, you are the party king. Matthew, thank you for teaching me what a plasma is. Chris, thank you for all of your help with LabVIEW and for teaching me about Tikz. Pierre-Yves, thank you for being an amazing coauthor and for teaching me about Python. Seabass, thank you for always helping me find the one character in my code that was making my plots not-quite perfect. Mike, thank you for all of your help repairing and renovating the LiLFA facilities, and for putting up with me when I occasionally threw a wrench in your direction. Pat and Tall Matt, thank you both for your help through the first two

years preparing for generals. Thank you also to all of the undergraduate researchers who contributed to the LiLFA and ALFA projects: Nick, Jeremy, Brannon, Brittany, Josh, and Jack.

I would never have pursued a degree in science if it weren't for the support of my family, especially my wife, Anna, and two daughters, Rhea and Della, my mother, my father, Christina, Sarah, Rob, James, Z, Elsa, Russ, and all the East Coast Coogans and Rés who have come to visit me in Princeton. My wife, in particular, made this pursuit possible. Anna, at the most stressful points in the program—before generals, and before my FPO—you made sure I had a baby to hold. Thank you for all your work taking care of me and our children, and for helping me to keep things in perspective. The pages in this thesis represent a great deal of time that I should have been spending with you.

The research in this dissertation was carried out with the support of the Princeton Plasma Physics Laboratory's Program in Plasma Science and Technology. This dissertation carries T#3356 in the records of the Department of Mechanical and Aerospace Engineering.

Contents

Abstract	iii
Acknowledgements	v
List of Tables	xi
List of Figures	xii
List of Symbols	xv
1 Introduction	1
1.1 Thrust mechanisms	3
1.1.1 Applied-field thrust component	3
1.1.2 Self-field thrust component	3
1.1.3 Gasdynamic thrust component	4
1.2 Impact of present work	4
1.3 Thesis structure	5
2 Review of Previous Thrust Models	7
2.1 Models of the applied-field thrust component	8
2.1.1 JB_{Ar} models	8
2.1.2 Non- JB_{Ar} models	11
2.2 Model of the self-field thrust component	16
2.3 Model of the gasdynamic thrust component	16
2.4 AF-MPDT database	17

2.4.1	Data catalogued	17
2.4.2	Determination of data validity	19
2.5	Method of evaluation	20
2.5.1	Comparison method	21
2.5.2	Filtering method	24
2.5.3	Parameters investigated	24
2.5.4	Application of data to models	26
2.6	Investigation of background pressure effects	26
2.7	Comparison of predictive accuracy	28
2.8	Summary	36
3	Empirical Model	38
3.1	Π-product-corrected Model	38
3.1.1	Method	38
3.1.2	Results	40
3.2	Physical interpretation of empirical model	41
3.3	Summary	46
4	Derivation of Thrust Scaling Parameters	47
4.1	Modified rigid-rotor model	47
4.1.1	Assumptions	48
4.1.2	Thrust	51
4.1.3	Moment of inertia	52
4.1.4	Angular frequency	55
4.2	Radius of flow separation from the anode	59
4.2.1	Convective terms	60
4.2.2	Gasdynamic pressure gradient	62
4.2.3	Lorentz force density	63

4.2.4	Comparison of radial forces	65
4.3	Applied-field thrust due to pinching forces	69
4.3.1	Effect of radial forces on pinching thrust component	69
4.3.2	Effect of radial forces on swirl thrust component	70
4.4	Summary	71
5	Verification with Reported Experimental Data	73
5.1	Confinement modes	74
5.2	Scaling of C_T with the confinement parameter	76
5.3	Applied-field thrust scaling	80
6	Applied-Field Thrust Component Measurements	86
6.1	Direct measurement of the applied-field thrust component	87
6.1.1	Thrust stand	87
6.1.2	Thrust measurement procedure	89
6.1.3	Initial test	91
6.2	Measurements of ΔT_{AF} with constant EM tare force	93
6.3	Results of applied-field thrust measurements	94
7	Conclusions	96
7.1	Significant contributions	96
7.1.1	Data comparison methodology and assembly of data catalog .	96
7.1.2	Method of directly measuring the applied-field thrust	97
7.1.3	Analytical and experimental findings	97
7.2	Future work	98
A	Propellant Properties	101
B	Catalogued Thrusters	103

C Experimental Apparatus	109
C.1 Steady-state MPDT facility	109
C.1.1 Vacuum	109
C.1.2 Cooling	110
C.2 The lithium Lorentz force accelerator	113
C.2.1 Lithium loading and cleaning procedures	114
C.2.2 Lithium feed system	116
C.2.3 Power	117
C.3 The argon Lorentz force accelerator	118
C.3.1 Argon mass flow control system	120
C.3.2 Power and ignition procedure	120
C.4 Diagnostics	121
C.4.1 Data acquisition system	121
C.4.2 Current and magnetic field strength measurements	121
C.4.3 Argon mass flow and background pressure measurements	123
D Gasdynamic Thrust Component Contribution	124
Bibliography	128

List of Tables

2.1	Mean prediction and error of each thrust model in the literature	30
2.2	Results of analysis of thrust models in the literature	31
3.1	Evolution of empirical model over successive iterations of Π products	40
3.2	Results of analysis of empirical thrust models	41
5.1	Design features of each thruster referenced in analysis	75
5.2	Constants derived from data for MAI thrusters	83
6.1	Results of different applied-field thrust component measurement techniques	93
A.1	Propellant properties used in analysis	102
B.1	Catalogued thrusters and their operating regimes	104

List of Figures

1.1	Force densities in SF- and AF-MPDTs	2
2.1	Thruster geometry definitions	18
2.2	Thrust as a function of background pressure	19
2.3	Demonstration of thrust model comparison method	22
2.4	Background pressure effects on thrust	27
2.5	Thrust prediction comparison by thruster	28
2.6	Thrust dependence on anode radius	32
2.7	Thrust dependence on the ratio of electrode radii	33
2.8	Thrust dependence on solenoid radius	33
2.9	Solenoid radius as a function of anode radius	34
2.10	Thrust dependence on the contour of the anode to the magnetic field	35
2.11	Thrust dependence on ionization energy	35
3.1	Comparison of empirical model to measurement	42
3.2	Schematic of the effective anode radius using either the surface of constant flux or the physical anode dimensions	43
3.3	The relative standard deviation as a function of the choice in effective anode radius	44
3.4	Effective anode radius dependence on the plasma beta parameter . .	45

4.1	Schematic of the geometry relevant to the separation of the plasma flow from the anode wall	54
4.2	Illustration of assumed velocity distribution	61
4.3	Radial force densities at the anode wall as a function of axial position	66
4.4	Radial Hall force component densities at the anode wall as a function of axial position	68
5.1	Thrust coefficient dependence on \bar{f} for the 200 kW Alta argon thruster	77
5.2	Thrust coefficient dependence on \bar{f} for the 12 kW H2-4F hydrogen thruster	78
5.3	Thrust coefficient dependence on the confinement parameter for the 30 kW MAI lithium thruster	79
5.4	Thrust coefficient dependence on the confinement parameter for the 150 kW MAI lithium thruster	80
5.5	Thrust coefficient dependence on \bar{f}_p for the 100 kW LeRC-A argon thruster	81
5.6	Thrust measurement versus prediction for the 30 kW MAI lithium thruster	82
5.7	Thrust measurement versus prediction for the 150 kW MAI lithium thruster	83
6.1	Solenoid thrust stand	88
6.2	Schematic of thrust stand calibration system	90
6.3	LVDT voltage as a function of scale position and known force	91
6.4	Parallel and antiparallel tare force thrust measurements	92
6.5	Thrust coefficient dependence on \bar{f}_p for the ALFA	94
C.1	Steady-state MPDT facility	110
C.2	Schematic of vacuum system	111

C.3	Schematic of cooling system	113
C.4	Cross-section of the LiLFA	114
C.5	Schematic of lithium feed system	116
C.6	Picture of the ALFA	119
C.7	Cross-section of the ALFA	119
C.8	Different magnetic field configurations for the ALFA	120
C.9	ALFA mass flow controller	121
C.10	Schematic of the power supply for the ALFA	122
C.11	Magnetic field strength as a function of solenoid current	123
D.1	Thrust coefficient dependence on \bar{f} for the 30 kW MAI lithium thruster where the applied-field thrust is calculated using the highest estimate in the literature for gasdynamic thrust	125
D.2	Thrust coefficient dependence on \bar{f} for the 150 kW MAI lithium thruster where the applied-field thrust is calculated using the highest estimate in the literature for gasdynamic thrust	126
D.3	Thrust coefficient dependence on \bar{f} for the 200 kW Alta argon thruster where the applied-field thrust is calculated using the highest estimate in the literature for gasdynamic thrust	127

List of Symbols

a_0	Speed of sound, m/s
B	Magnetic field, T
B_A	Applied magnetic field, T
B_{a0}	Magnetic field at the anode throat or backplate, T
B_{ae}	Magnetic field at the anode exit plane, T
B_{SF}	Self-induced magnetic field, T
\mathbf{B}	Maxwell stress tensor, Pa
e	Elementary charge, C
E	Electric field strength, V/m
f	Force density, N/m ³
f_{cent}	Centrifugal force density, N/m ³
f_H	Force density resulting from Hall currents, N/m ³
f_{in}	Inward radial force density, N/m ³
f_{out}	Inward radial force density, N/m ³
f_{SF}	Force density resulting from self-induced magnetic field, N/m ³
\bar{f}	Confinement parameter defined by the ratio of inward radial forces to outward radial forces within the anode
\bar{f}_p	Confinement parameter defined by the ratio of pressure gradient to centrifugal force density within the anode
F	Force, N
I	Moment of inertia, kgm ²
j	Current density, A/m ²
C_T	Applied-field thrust coefficient
J	Current, A
J_B	Current to solenoid, A

k	Thrust coefficient
$k_{\text{Albertoni}}$	Thrust coefficient used by Albertoni et al.
k_{GD}	Gasdynamic thrust coefficient
k_{Tikhonov}	Thrust coefficient used by Tikhonov et al.
k_{B}	Boltzmann constant, J/K
l_a	Anode length, m
l_c	Cathode length, m
m	Mass of rotating plasma column in anode, kg/s
\dot{m}	Mass flow rate, kg/s
m_e	Electron mass, kg
M_i	Ion mass, kg
n_e	Electron density, m ⁻³
n_i	Ion density, m ⁻³
$\hat{\mathbf{n}}$	Unit normal
p_b	Background pressure, Pa
p_{GD}	Gasdynamic pressure, Pa
p_{flow}	Gasdynamic pressure resulting from the modeled flow, Pa
$p_{\Sigma f}$	Gasdynamic pressure resulting from the sum of radial force densities, Pa
P_θ	Power applied to rotating plasma column, W
r	Radial coordinate
r_a	Anode radius, m
$r_{a-\text{eff}}$	Effective anode radius
r_{a0}	Anode throat radius, m
r_{ae}	Anode exit plane radius, m
$r_{ae-\text{eff}}$	Effective anode exit plane radius, m

$r_{ae-\Phi}$	Radius at the anode exit plane of a flux tube beginning at the anode throat, m
r_B	Solenoid radius, m
r_{Bi}	Inner solenoid radius, m
r_{Bo}	Outer solenoid radius, m
r_c	Cathode radius, m
r_{sep}	Radius at which plasma flow separates from the anode, m
r^*	Effective electrode radius for Sasoh thrust model
\bar{r}	Ratio of anode radius to cathode radius
\bar{r}_ω	Geometric parameter used to determine the angular frequency
\hat{r}_{a-0}	Fractional distance between the anode throat and the anode exit plane
$\hat{r}_{a-\Phi}$	Fractional distance between the surface of constant magnetic flux and the anode surface
\hat{r}_a^*	Value of $\hat{r}_{a-\Phi}$ at which the relative standard deviation is minimized
Re	Reynolds number
\hat{s}	Relative standard deviation
$\hat{s}_{Tikhonov}$	Relative standard deviation found using the Tikhonov et al. model
S	Surface, m ²
t	Time, s
T	Total thrust, N
T_{AF}	Applied-field component of thrust, N
$T_{Albertoni}$	Applied-field component of thrust as modeled by Albertoni et al., N
$T_{Coletti}$	Thrust as modeled by Coletti, N
$T_{Fradkin}$	Applied-field component of thrust as modeled by Fradkin et al., N
T_{GD}	Gasdynamic component of thrust, N
T_H	Hall component of thrust, N

T_{Herdrich}	Applied-field component of thrust as modeled by Herdrich et al., N
$T_{\text{Mikellides}}$	Applied-field component of thrust as modeled by Mikellides and Turchi, N
T_{Myers}	Applied-field component of thrust as modeled by Myers, N
$T_{\text{AF-pinch}}$	“Pinch” component of the applied-field thrust, N
T_{Sasoh}	Thrust as modeled by Sasoh, N
T_{SF}	Self-field component of thrust, N
T_{SW}	“Swirl” component of thrust, N
T_{Tikhonov}	Applied-field component of thrust as modeled by Tikhonov et al., N
\bar{T}	Dimensionless thrust parameter
$\hat{\bar{T}}$	Normalized thrust parameter
\mathcal{T}_{e}	Electron temperature, K
\mathcal{T}_{i}	Ion temperature, K
u	Velocity, m/s
$u_{z,\text{ae}}$	Axial ion velocity at the anode exit plane, m/s
μ	Viscosity, Pa·s
U	Voltage, V
V	Volume, m ³
x	Arbitrary parameter
\bar{Y}	Ionization factor
z	Axial distance from anode backplate or throat, m
z_{sep}	Axial distance from anode backplate or throat at which plasma flow separates from the anode, m
Z	Charge number
α	Angle of anode with respect to thrust axis
β_{ae}	Ratio of gasdynamic to magnetic pressure evaluated at the anode exit plane

γ	Adiabatic index
ϵ_0	Vacuum permittivity, C/V·m
ϵ_i	Ionization energy, J
η_θ	Efficiency of conversion of azimuthal energy to directed kinetic energy in the magnetic nozzle
θ	Azimuthal coordinate
θ_{div}	Angle of the magnetic field at the detachment plane with respect to the thrust axis
ι	Degree of ionization
κ_i	Scaling constant for i^{th} Π product
μ_0	Permeability of free space, N/A ²
ν_{ei}	Electron-ion collision frequency, s ⁻¹
ν_i	Ion collision frequency, s ⁻¹
ξ	Additive constant
Π_i	i^{th} Π product
ρ	Mass density, kg/m ³
σ	Conductivity, S/m
ς	Detachment parameter, s ⁶ /m ⁹
τ	Torque, Nm
$\tau_{z,\text{aw}}$	Torque on anode wall, Nm
$\tau_{z,\text{bp}}$	Torque on thruster back plate or throat, Nm
$\tau_{z,c}$	Torque on cathode tip, Nm
Φ_{a0}	Magnetic flux through the anode throat or backplate, T·m ²
Φ_{ae}	Magnetic flux through the anode exit plane, T·m ²
$\bar{\Phi}$	Contour of anode to magnetic field
ω	Angular frequency, s ⁻¹

Chapter 1

Introduction

SINCE the 1960s, the applied-field magnetoplasmadynamic thruster (AF-MPDT) has proven to be a high-thrust density alternative to other forms of electric propulsion [1]. As such, it has been proposed as a candidate for missions requiring the transfer of large payloads in short timeframes, including manned missions to the Moon, Mars, and beyond [2, 3, 4]. Although the power requirements for this thruster have made it an infeasible option for space exploration up until the present, the projection for as much as 200 kW of solar power for spacecraft [5, 6] may make AF-MPDT operation possible in the near- to mid-term. However, questions remain as to how to optimize the performance of this thruster for the requirements of a given mission. A useful tool for this optimization would be a scaling parameter that is relevant to thrust generation over a large and varied parameter space.

MPDTs are a class of electromagnetic thruster. They are typically coaxial devices with a cylindrical or conical anode surrounding a central cathode. Gas is injected into the thruster through the cathode, the inner face of the anode, and/or an insulator separating the two. The gas is ionized when a voltage is applied between the electrodes, allowing current to pass through the resulting plasma. In a self-field (SF) MPDT, typical currents are on the order of 10,000 A, and these currents gen-

erate a self-induced azimuthal magnetic field, as is illustrated in Fig. 1.1 (a). An *applied-field* MPDT also has an externally applied diverging axial magnetic field, as is shown in Fig. 1.1 (b), with typical applied-field values being less than 0.5 T. Operating currents for AF-MPDTs span a large range compared to the SF-MPDT, from 10 to 20,000 A [7]. For both thrusters, Lorentz forces resulting from the interaction of currents through the plasma with the magnetic field accelerate the plasma, and when this acceleration is along the thrust axis, it produces thrust. The ability of the AF-MPDT to operate efficiently at comparatively low current and power levels, while maintaining a high thrust density, is what makes it an excellent candidate for near-term missions requiring rapid acceleration.

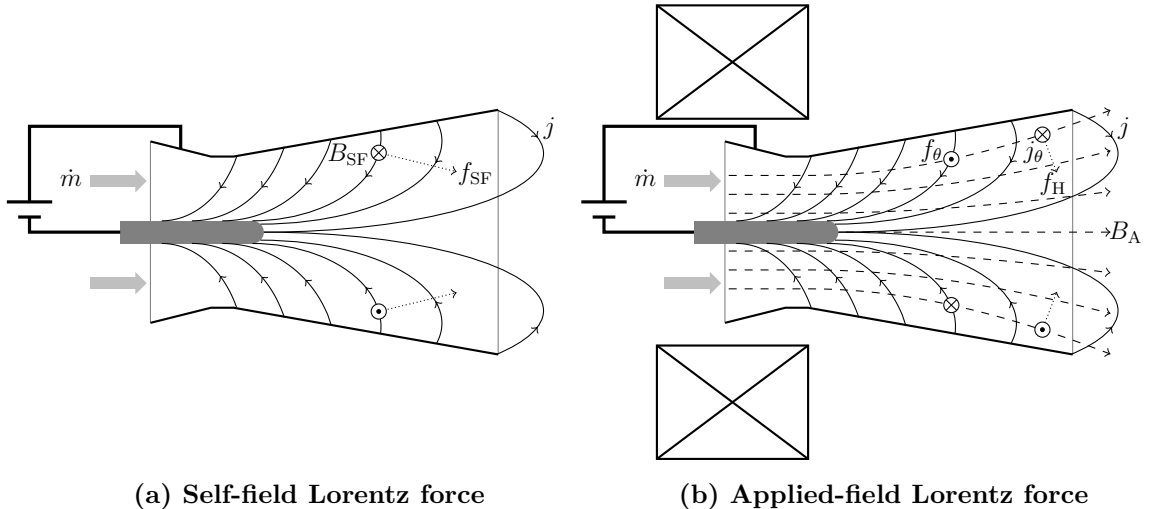


Figure 1.1: Lorentz forces resulting from a self-induced magnetic field (a) and from an external magnetic field (b) shown in schematic cross-sections of MPDTs. The external magnetic field adds azimuthal and Hall-effect force densities (f_θ and f_H respectively) to the self-field force density (f_{SF}).

Many AF-MPDT thrust models have been put forth to date [1, 8, 9, 10, 11, 12, 13, 14, 15], however each of these models has shortcomings, and for one reason or another fails to fully describe the measured thrust for all thrusters and operating regimes. Our goal is to determine thrust scaling as a function of controllable parameters. These parameters include both operating parameters (such as current, applied field strength,

propellant, and mass flow rate) and geometric ones (such as electrode and solenoid length scales). The hurdles to developing such a model are significant—the current distribution within the thruster is difficult to determine without measurement, and the current distribution in turn alters the magnetic field and temperature distribution within the plasma. In addition, there are several competing thrust mechanisms.

1.1 Thrust mechanisms

The thrust of an AF-MPDT is typically assumed to be the sum of the applied-field, self-field, and gasdynamic thrust components [14, 15, 16, 17]. The volumetric Lorentz force densities are illustrated in Fig. 1.1.

1.1.1 Applied-field thrust component

As shown in Fig. 1.1 (b), the mostly axial external magnetic field crossed with the radial component of the current swirls the plasma. This bulk swirling motion is converted into axial thrust as the rotating body expands through the diverging applied field and then detaches from the field lines. The swirling motion also results in an azimuthal Hall current due to the collisional nature of AF-MPDTs, which preferentially allows electrons to travel azimuthally. This Hall current crossed with the radial component of the diverging applied magnetic field generates additional thrust. It is these two thrust mechanisms, resulting from the applied field, that are the focus of this thesis, and which are the dominant thrust producing mechanisms in most AF-MPDTs.

1.1.2 Self-field thrust component

The self-field thrust component is generated by the cross product of the radial current through the plasma with the self-induced azimuthal magnetic field, which is generated

by the enclosed axial current. This component is illustrated in Fig. 1.1 (a). The primary thrust producing mechanism is the “blowing” component of the Lorentz force, which is parallel to the thrust axis, however, Choueiri [18] demonstrated that the inward or “pinching” component of the Lorentz force generates a gasdynamic pressure distribution that also produces thrust.

1.1.3 Gasdynamic thrust component

The gasdynamic thrust component results from the conversion of thermal energy into directed kinetic energy by means of a nozzle. While it is often assumed to be negligible in a high-power regime, at low currents and applied-field strengths, or high mass flow rates, the gasdynamic thrust component can be substantial or even dominant. This component is dependent on the mass flow rate, the velocity at the injection site, the gasdynamic pressure inside the nozzle, and the nozzle area over which that pressure is applied.

1.2 Impact of present work

Our ultimate goal is to determine how the thrust of an AF-MPDT scales with controllable parameters. Along with a voltage model for this thruster [19], a thrust model will enable the optimization of thruster design for a given set of operating conditions. With this goal in mind, we will attempt to answer the following questions:

- *Which operating and geometric parameters influence the thrust?*

We will assemble all of the thrust data in the literature into a single database. Through an analysis of approximately 60 years worth of AF-MPDT data, we will determine which controllable parameters influence the thrust, as well as the relative importance of each parameter. This analysis will also allow us to

compare the prediction of each thrust model in the literature to the measured thrust in order to demonstrate the strengths and shortcomings of each model.

- *What are the underlying physical mechanisms responsible for thrust generation?*

Using the results of our analysis of the literature data as a starting point, we will derive an empirical model using physically-meaningful nondimensional parameters. Then, based on the prediction of this empirical model and the demonstrated thrust scaling, we will gain insight into the underlying physics involved. Specifically, we will show that the primary shortcoming of previous thrust models is a poor estimation of the thrust coefficient, which is a function of the radial forces within the anode. We will then derive a theoretical model as a result of this insight.

- *How do we determine the balance of the thrust mechanisms in a given thrust measurement?*

In order to determine if a theoretical model correctly predicts the thrust, we must compare the prediction to measurement, but since we are only interested in the applied-field thrust component, and measurements are typically of the total thrust, such a comparison has limitations. We will validate a new method of making an isolated measurement of the applied-field thrust component, and compare measurements made using this technique to the predicted thrust scaling.

1.3 Thesis structure

We begin in Chapter 2 by reviewing thrust models from the literature. We assemble a database of all thrust data in the literature, create metrics for determining the reliability of that data (particularly concerning background pressure and the dominance of the applied-field component of thrust), and compare the ability of each model to

predict the measured value across a large and varied parameter space. In Chapter 3, we use dimensional analysis to empirically derive a new thrust model based on the findings of the previous chapter. This empirical model is used as a starting point for understanding the physical mechanisms responsible for the discrepancies between the prediction of models in the literature and measurement under certain operating conditions. Using this insight, we derive in Chapter 4 a “confinement parameter,” which describes two different modes of AF-MPDT operation, and which plays a significant role in determining the applied-field thrust. In Chapter 5, we compare thrust data from the literature to the predictions made for our scaling parameter. In Chapter 6, we describe an applied-field thrust component measurement system and verify that conclusions in the previous chapter are not due to the influence of gasdynamic and self-field thrust components. Finally, in Chapter 7 we provide a summary of our significant findings and possible avenues of future research.

Chapter 2

Review of Previous Thrust Models¹

For an AF-MPDT operating under typical operating conditions, the applied-field component of the thrust is dominant. For this reason, we focus in this thesis on the applied-field thrust component. However, before adding to the long list of thrust models in the literature, we must first establish the *need* for a new model. In this chapter, we review all analytical applied-field thrust component models. We assemble a database of all AF-MPDT thrust measurements in the literature and compare the predictions of each model to the data. We develop the metrics necessary both to ascertain the validity of the data in the database and to quantitatively compare the predictive accuracy of one model against any other.

Although our focus is on applied-field thrust component models, some of these models and the model we will develop in Chapter 4 are inseparable from other thrust components, and so we provide descriptions of the most commonly implemented self-field and gasdynamic thrust components as well.

¹This chapter is based on work being prepared to be submitted for publication and previously presented in [20]: W. J. Coogan and E. Y. Choueiri, “A Critical Review of Thrust Models for Applied-Field Magnetoplasmadynamic Thrusters,” In *AIAA Propulsion and Energy 2017*, AIAA-2017-4723, Atlanta, GA, July 10–12, 2017. doi:10.2514/6.2017-4723

2.1 Models of the applied-field thrust component

The applied-field thrust component includes any thrust generated as the result of the application of an applied magnetic field. Many models of the applied-field thrust are similar in nature, predicting that $T_{\text{AF}} \propto JB_A r$, where T_{AF} is the applied-field thrust component, J is the current, B_A is the applied field strength, and r is a characteristic electrode length scale. We categorize these as “ $JB_A r$ ” models. In addition, there are three models which assume a more complicated relationship between thrust and the parameters upon which it depends. These we categorize as “non- $JB_A r$ ” models.

2.1.1 $JB_A r$ models

Fradkin et al.

Fradkin et al. [8] assume a strictly axial magnetic field in the thruster volume, derive the torque resulting from the radial current and the applied field, and then assume this torque acts to rotate the plasma inside the thruster as a rigid rotor. Assuming all of the resulting azimuthal kinetic energy is converted into axial kinetic energy, they find that

$$T_{\text{Fradkin}} = JB_A \frac{r_a^2 - r_c^2}{\sqrt{2(r_a^2 + r_c^2)}}, \quad (2.1)$$

where T_{Fradkin} is the predicted upper limit for the applied-field component of the thrust, B_A is the applied magnetic field strength (assumed to be constant in the thruster volume), r_a is the anode radius, and r_c is the cathode radius.

Fradkin et al. derive this equation for a particular geometry that may not be relevant to all thrust data used in this survey. A cylindrical rotating body is assumed, with a hollow core accounting for a cathode that extends through the anode volume. Many thrusters have anodes whose radii vary axially and/or cathodes that do not extend into the anode volume. Further, the assumption of a constant, purely axial

magnetic field is less valid for smaller solenoid radii unless the anode is completely enclosed by the solenoid. The largest solenoid in the literature that does not enclose the anode is that employed by the Moscow Aviation Institute for the 150 and 200 kW Li thrusters, for which the magnetic field strength decreases by a factor of 2 in the span of the anode length, indicating significant divergence.

Myers

Using the Fradkin et al. model as a starting point, Myers derives an expression for the applied-field thrust component [9] empirically based on his experiments with 100 kW class AF-MPDTs using a variety of different electrode geometries. He finds that

$$T_{\text{Myers}} = JB_A \frac{r_a^2}{500 r_c l_c}, \quad (2.2)$$

where l_c is the length of the cathode and the constant 500 has dimensions of m^{-1} . This model predicts an influence of the cathode geometry that is significant, whereas that predicted by Fradkin et al. can be neglected for $r_a \gg r_c$. Myers incorporates his observation that thrust decreases with cathode length in the regime in which he operated, however this makes the expression inapplicable to thrusters with recessed cathodes, for which $l_c \leq 0$.

Albertoni et al.

Albertoni et al. [15] apply an empirically-derived dimensionless scaling constant, $k_{\text{Albertoni}}$, to the Fradkin et al. model to fit the data for a given thruster, so that

$$T_{\text{Albertoni}} = k_{\text{Albertoni}} T_{\text{Fradkin}}. \quad (2.3)$$

This constant can be determined experimentally for each thruster and is representative of the degree to which the conversion of azimuthal motion to axial motion

takes place within the magnetic nozzle. In our application of this model, we set $k_{\text{Albertoni}} = 0.25$, which is reported in Ref. [15] to result in good general agreement between prediction and the measurements against which the model was originally compared.

Tikhonov et al.

In contrast to the model presented by Fradkin et al., which assumes a constant magnetic field in the thruster volume, Tikhonov et al. derive an analytical model [10, 21, 22] assuming that the thrust is the result of the Hall current crossing the radial component of the diverging magnetic field. They find that

$$T_{\text{Tikhonov}} = k_{\text{Tikhonov}} J B_A r_a. \quad (2.4)$$

where k_{Tikhonov} is a scaling constant. While they provide an explicit expression for the scaling constant in terms of the length of the cathode and the magnetic flux at two axial positions within the anode, the inverse dependence on cathode distance from the anode exit plane makes the expression unsuitable for thrusters with cathodes extending through the anode volume. Tikhonov et al. give a value [16, 17, 23, 24, 25] of $k_{\text{Tikhonov}} \simeq 0.2$ and note that k_{Tikhonov} can be experimentally determined for any given thruster. However, since we seek a model than can predict measurement *a priori*, we treat the coefficient as a constant.

Despite being based on different acceleration mechanisms, in the limit where $r_a \gg r_c$, this model and that of Fradkin et al. agree to within a scaling constant. Outside of this limit, we expect the absence of any r_c dependence in this model to make r_c an important parameter for comparing the predictive power of the two models. We note that under typical operating conditions the thrust due to the expansion of the swirling plasma in the magnetic nozzle is approximately an order of magnitude greater than the Hall thrust [26, 27, 28].

Herdrich et al.

The model of Herdrich et al. [14] uses the model of Tikhonov et al. as a starting point, but they model the coefficient as a function of r_a , which they obtain from the data using a power law fit, yielding the equation

$$T_{\text{Herdrich}} = 2.924 J B_{\text{Ar}} r_a^{1.6577}, \quad (2.5)$$

where the scaling constant has dimensions of $\text{m}^{-0.6577}$. While this yields better agreement with the data, it is unclear whether this agreement is due to a more accurate representation of the effects of the anode radius itself, rather than the solenoid radius or cathode radius, that frequently scale with anode radius.

Krülle

In his model, Krülle [1] uses resistive magnetohydrodynamics and assumes that the plasma swirls as a rigid rotor, but notes that his measured thrust depends linearly on magnetic field strength, rather than quadratically as is predicted by his model. He attributes this discrepancy to current outflow beyond the anode exit plane. Because he points out this discrepancy, we mention this model for completeness, but do not include it in the statistical analysis at the end of the chapter.

2.1.2 Non- $J B_{\text{Ar}}$ models

Mikellides and Turchi

Mikellides and Turchi derive a model [12] that is based on results from MACH2, a numerical simulation tool, which they used to simulate a 100 kW class argon thruster. Their model assumes that the Lorentz force rotates the plasma, generating a shear due to the plasma viscosity. The primary acceleration mechanism in this model is the

conversion of thermal energy from viscous heating into directed kinetic energy. They obtain

$$T_{\text{Mikellides}} = \frac{25}{M_i^{1/4}} \sqrt{\frac{r_c}{l_c \bar{Y}}} \frac{\bar{r}(\bar{r}+1)\sqrt{\bar{r}-1}\sqrt{\dot{m}JB_A}}{\sqrt{\bar{r}^{3.8}-1}}, \quad (2.6)$$

where \bar{r} is the ratio of anode radius to cathode radius, \dot{m} is the mass flow rate, M_i is the atomic mass (values given Appendix A), and \bar{Y} is the ionization factor. This ionization factor is a measure of the ionization states in the plasma, and is defined by

$$\bar{Y} = \sum_i \left(\frac{\iota_i}{\sum_j \iota_j^2 Z_i^2 Z_j^2} \right), \quad (2.7)$$

where ι is the degree of ionization and Z is the charge number. While Ref. [12] provides \bar{Y} values for H₂, Li, and Ar, we cannot determine \bar{Y} analytically without knowing the degree of ionization for each state, which Mikellides and Turchi find through their numerical simulation. Since we are using data for a multitude of propellants, including heteronuclear species, and further since thrust depends weakly on \bar{Y} for typical ionization fractions, we let $\bar{Y} = 1$ for all of our calculations. This assumes that the plasma is completely and singly ionized. We therefore expect any disagreement between this model and our implementation of it to be correlated with ionization energy, ϵ_i , of a given propellant, and consequently test the predictions of each model against measurement as a function of ϵ_i in Sec. 2.7.

This model makes two unique predictions. First, thrust is predicted to have a strong dependence on \dot{m} , resulting from the modeled influence of plasma viscosity. Second, Mikellides and Turchi predict $T_{\text{AF}} \propto \sqrt{JB_A}$ whereas it has long been assumed and repeatedly verified experimentally to be proportionate to JB_A [1, 9, 29, 30, 31]. Also worth noting is that the inverse dependence on l_c , as with the Myers model, makes this model incompatible with certain thruster geometries.

Sasoh and Arakawa

Sasoh and Arakawa [11] use energy conservation, as well as Ohm's law, to derive the total work done within the anode. Then, they assume that this work is converted into directed kinetic energy, generating thrust. They find the total thrust to be

$$T_{\text{Sasoh}} = \frac{T_H + T_{\text{SF}}}{2} + \sqrt{\left(\frac{T_H + T_{\text{SF}}}{2}\right)^2 + T_{\text{SW}}^2}, \quad (2.8)$$

where T_H , T_{SF} , and T_{SW} are the thrust components due to the Hall effect, the self-field, and the azimuthally accelerated (or “swirled”) plasma respectively. This expression differs from our previous description of the total thrust as the sum of several components. This is due to its derivation from an energy balance rather than a momentum balance. The result is that T_{SF} as described here is not necessarily the same as that described by Eq. 2.13.

The individual expressions Sasoh and Arakawa provide for the thrust components have too many dependencies to express in a concise form appropriate to a review, so we summarize the assumptions we made in our application of this model and direct the reader to Ref. [11] for the explicit expressions.

Our primary difficulty implementing this model as a *predictive* one stems from its dependence on terms for which we require measurement, such as electron temperature or density, or for which no procedure is provided, such as a characteristic length scale. The Hall parameter, for instance, depends on the collision frequency between electrons and ions, ν_{ei} . We use the relation [32]

$$\nu_{\text{ei}} = 3.64 \times 10^{-6} \frac{n_e \ln(1.24 \times 10^7 \sqrt{\mathcal{T}_e^3/n_e})}{\mathcal{T}_e^{1.5}}. \quad (2.9)$$

to determine this parameter, where \mathcal{T}_e is electron temperature in K and n_e is electron density in m⁻³. Because electron temperatures from 1–10 eV have been reported for

AF-MPDTs [17, 19, 33, 34], we solve for the thrust using this full range of temperatures, giving a range of possible thrust values.

We model n_e using the continuity equation and assume that $n_i = n_e$. The area of the anode exit plane and \dot{m} are known, but we require the axial component of the ion velocity through this plane, $u_{z,ae}$. The ion velocity exiting the anode volume is T/\dot{m} , but because we need this density estimation in order to determine T , we use the full range of possible exit velocities found in the database, 0.8–86 km/s. Our final expression is

$$n_e = \frac{\dot{m}}{\pi r_{ae}^2 M_i u_{z,ae}}, \quad (2.10)$$

where r_{ae} is the anode exit plane radius. As with temperature, the range of possible exhaust velocity values results in a range of calculated thrust values.

The Sasoh and Arakawa model requires a characteristic length scale which they denote as r^* . It is unclear how this value is determined, but in the example they provide in Ref. [11], the given value is approximately 1/10th the distance from the cathode radius to the anode radius, and so we use the expression

$$r^* = r_c + \frac{r_a - r_c}{10}. \quad (2.11)$$

In order to solve for the radial and axial components of the magnetic field, we use the Biot Savart law for a solenoid [35].

Coletti

While the model of Fradkin et al. predicts the amount of thrust *possible* from the swirling plasma being redirected in a magnetic nozzle, Coletti [13] models the degree to which this redirection occurs by deriving the plasma velocity and trajectory at the

point of detachment. Detachment is assumed to occur when the Alfvén velocity is reached [36].

Coletti's derivation divides the thrust mechanisms into two distinct physical regions: the anode volume, where plasma acceleration is the result of self-field and applied-field forces, and the magnetic nozzle downstream of the anode volume, where conservation of both energy and the magnetic moment redirect the velocity along the magnetic field lines. He finds the velocity parallel to the magnetic field at the point of detachment, which, along with the angle of the field with respect to the thrust axis, θ_{div} , determines the total thrust. This angle is found from the divergence of the magnetic field at the point of detachment [37]. He determines the thrust to be

$$T_{\text{Coletti}} = \frac{1}{2} \left(u_{z,\text{ae}} + \sqrt{u_{z,\text{ae}}^2 + \omega^2 r_a^2 - \omega^8 r_a^8 \frac{r_B^3}{\varsigma} \cos(\theta_{\text{div}})} \right) \dot{m}, \quad (2.12)$$

where $u_{z,\text{ae}}$ is the ion velocity at the anode exit plane found using the Maecker formula (Eq. 2.13), r_B is the solenoid radius, ω is the angular velocity of the plasma inside the thruster volume, and ς is a function of the rotational velocity of the plasma and the axial position at detachment. The angular velocity is found from the radial current crossed with the axial applied magnetic field, with the assumption that the plasma rotates rigidly.

The Coletti model reduces to the Maecker formula (Eq. 2.13) when $B_A \rightarrow 0$, however there are instances in which the third term under the square root can result in a predicted thrust less than that predicted by Eq. 2.13. In these instances, we use the value predicted by Eq. 2.13 as is prescribed in Ref. [13]. Relevant to this model is the recent research by Ahedo and Merino [38], which shows that the plasma detachment conditions assumed in this model do not apply to propulsive magnetic nozzles. Nonetheless, without an alternative detachment model, we use the Coletti model as it stands for all reported results.

2.2 Model of the self-field thrust component

The self-field thrust component is often assumed to be

$$T_{\text{SF}} = \frac{\mu_0}{4\pi} \left[\ln \left(\frac{r_a}{r_c} \right) + \frac{3}{4} \right] J^2, \quad (2.13)$$

as modeled by Maecker [39]. Maecker did not originally include the constant $3/4$, but Jahn showed how constants on the order of unity can be assumed depending on the cathode geometry [40], and $3/4$ tends to provide the best agreement with data at high current levels [41].

The Maecker formula does not fully describe the performance of SF-MPDTs. The discrepancy between prediction and measurement has been well-described in Ref. [18], which shows that at low J^2/\dot{m} values, the thrust measured can be as high as double that predicted by the Maecker formula. This is attributed to a gasdynamic pressure created by the pinching component of the volumetric Lorentz force.

2.3 Model of the gasdynamic thrust component

The gasdynamic thrust component, T_{GD} , is the result of the conversion of thermal energy into directed kinetic energy by means of a nozzle. It is usually described as

$$T_{\text{GD}} = k_{\text{GD}} \dot{m} a_0, \quad (2.14)$$

where k_{GD} is a dimensionless coefficient on the order of unity [14, 15, 16, 17, 42, 21] and a_0 is the ion sound speed. The magnitude of k_{GD} has been modeled as being dependent on the angle of the gas flow with respect to the thrust axis [42] or as a function of a pressure acting over the area of the injection site [43]. Ref. [43] determines $k_{\text{GD}} = 1 + 1/\gamma$ for a 100 kW lithium thruster with mass injection through the cathode, where γ is the adiabatic index. For polyatomic propellants, γ is poorly

defined, but the range of this value is small enough not to change the order of the value predicted by Eq. 2.14.

Determination of the ion sound speed requires the ion temperature. There are few measurements of ion temperature, T_i , in MPDTs, but those that exist [44, 45, 46] indicate that operating temperatures are in the range of 2 to 20 eV.

2.4 AF-MPDT database

In order to compare predicted performance with experimental results, we require data for which a number of parameters have been recorded, as well as metrics for determining data validity.

2.4.1 Data catalogued

We performed a thorough survey of the literature and collected all data which included measurements of each of the following: thrust (T), electrode current (J), electrode voltage (U), magnetic field strength (B_A), propellant, mass flow rate (\dot{m}), background pressure (p_b), inner and outer solenoid radii (r_{Bi} and r_{Bo}), and electrode geometry. The electrode geometry recorded includes the anode length (l_a), the anode radius at the throat or backplate (r_{a0}), the anode radius at the exit plane (r_{ae}), the cathode length (l_c), and the cathode radius (r_c), as is illustrated in Fig. 2.1.

For some configurations, multiple anode lengths were recorded as defined by distinct changes in contour (eg. Fig. 2.1 (c), (e), and (f)), here denoted as l_{a1} and l_{a2} . Some configurations feature a change in contour, but the site of propellant injection implies the dominance of the exit region and so only the exit length is recorded (eg. Fig. 2.1 (b)). If thrust error and electrode material were reported, that information was also recorded. If the magnetic field strength was reported at multiple locations, that recorded in the database is from the tip of the cathode. Where measurements

were not explicitly listed, they were deduced if at all possible (eg. if thrust, efficiency, and current are known, the voltage can be deduced).

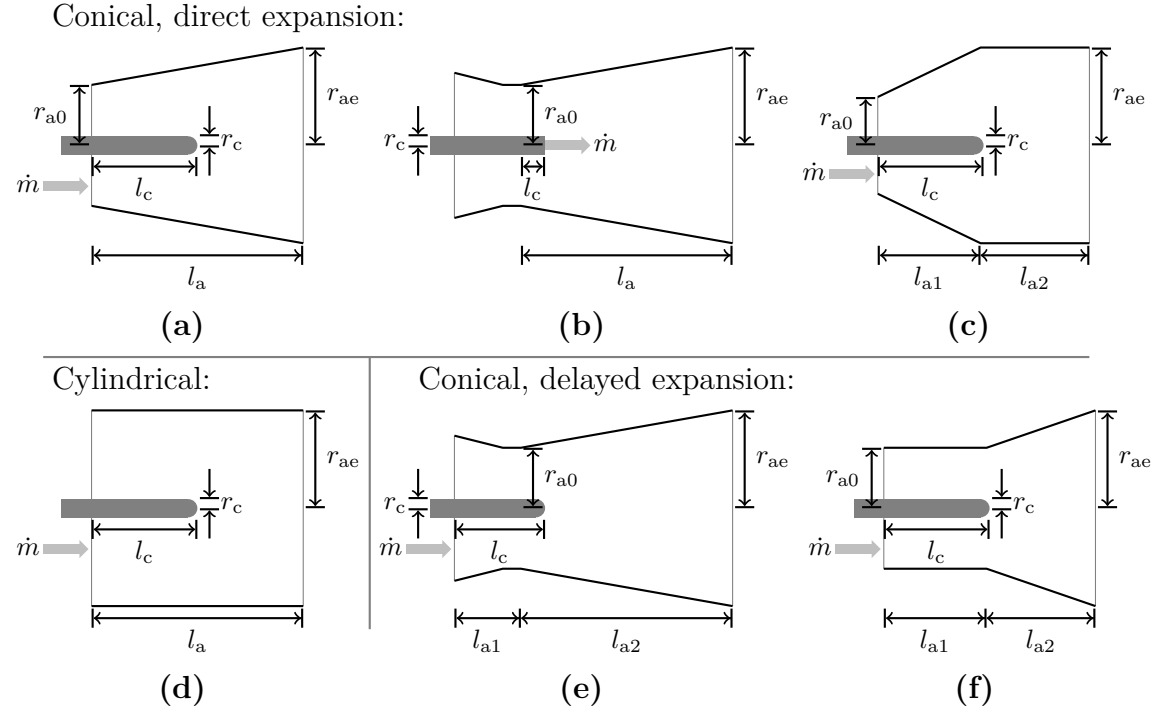


Figure 2.1: Characterization of the geometry for each of the thrusters in the AF-MPDT database.

Measurements that were made using multiple species simultaneously were not recorded. Also omitted were thrusters using configurations that are not conducive to use with the thrust models of interest, such as rectangular MPDTs [47, 48], the hybrid plasma thruster [49], and thrusters using permanent magnets [50].

More than 2700 thrust measurements and corresponding operating parameters were collected in this survey. Each thruster for which we have data is listed in Appendix B, along with typical operating conditions and citations for the gathered data. The full data collection can be accessed online [7].

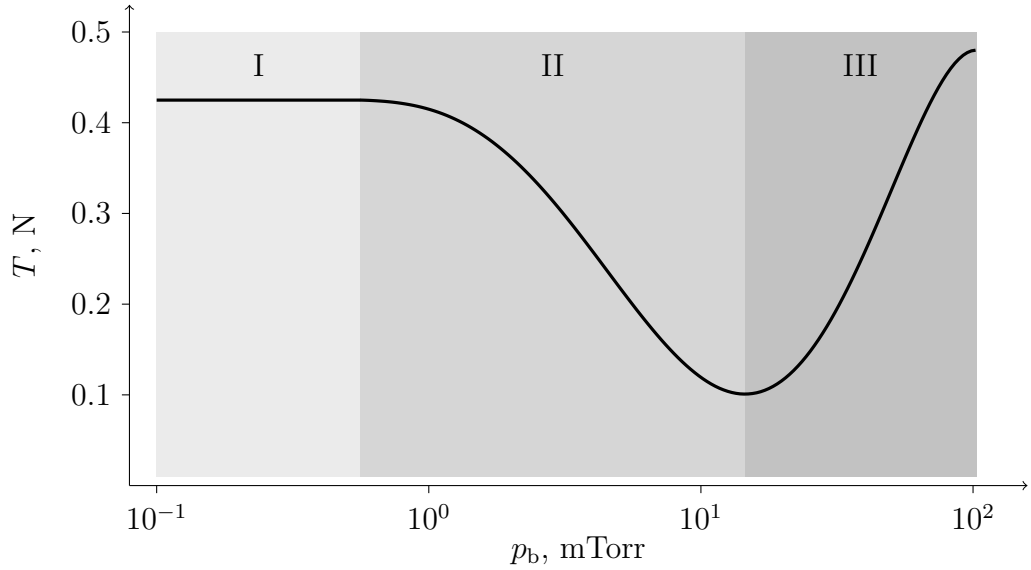


Figure 2.2: Typical thrust variation as a function of background pressure with three distinct regimes.

2.4.2 Determination of data validity

It has been previously demonstrated that background pressures above a given threshold influence thruster performance [31, 51, 52, 53, 54, 55, 56, 57]. A comprehensive review of this influence is provided in Ref. [58]. Because only two thrusters [52, 56, 57] have data for which background pressure is shown to have no influence, we need to determine which of the collected measurements are affected by high background pressures.

An interpolation of the data collected to determine background pressure effects in Ref. [57] is shown in Fig. 2.2. We see that there are three distinct regions, denoted here as I, II, and III. Region I shows no influence of background pressure on thrust, indicating that below a given threshold, just under 1 mTorr in this case, the thrust data are representative of that expected for an actual spacecraft. Region II shows a decrease in thrust. This is due to collisions in the plume that interfere with the expansion through the magnetic nozzle [51, 55, 59]. In Region III, the thrust increases

with pressure due to mass entrainment in the thruster, effectively increasing the mass flow rate [51, 55, 59].

Cann et al. performed the same test as that in Ref. [57] on the same model thruster, but using potassium propellant instead of sodium [56]. Again, they showed that the thrust was unaffected by background pressure up to 1 mTorr. The only other data that show a distinctly level region were in Ref. [52], where effects of pressure on thrust were minimal up to 0.9 mTorr with argon propellant.

Sovey et al. [51] report 0.3 mTorr as a safe upper-limit for operation without facility pressure effects on performance. However, their primary metric for this determination was the thrust-to-power ratio measured as a function of background pressure. We make the distinction that we are interested only in the effects of pressure on *thrust* because voltage is not a variable in the thrust models under review. Based on the limited thrust data available, it appears that 1 mTorr is a sufficiently low pressure to minimize any influence on thrust, however we separately analyzed the data collected at or below 0.1 mTorr and that collected at or below 1 mTorr with the results given in Table 2.1 and Fig. 2.5. Performance across a wide range of facility pressures is given in Fig. 2.4.

2.5 Method of evaluation

Using the database, while excluding data collected at high pressure, we could compare the prediction of any given model with any single given measurement, however we seek a method that will allow us to make a comparison en masse over a large and varied parameter space. We have developed a method by which a model's ability to predict measurement as a function of a controllable parameter can be tested. Furthermore, due to the previously stated discrepancies between the prediction of the Maecker formula and measurement, we apply this method without invoking self-

field or gasdynamic thrust models (except where implicitly prescribed by a particular applied-field model) by limiting our analysis to measurements for which the applied-field component is dominant.

2.5.1 Comparison method

To evaluate the degree to which each model predicts measurement, we nondimensionalize each prediction for a given set of parameters with the measured thrust,

$$\bar{T}_{\text{model}} = \frac{T_{\text{model}}}{T_{\text{measured}}}. \quad (2.15)$$

A perfect model would yield $\bar{T} = 1$ for every data point, however a more predictive model is one that predicts trends rather than magnitude, and so we normalize the nondimensional thrust for each model such that

$$\hat{\bar{T}}_{\text{model}} = \frac{\bar{T}_{\text{model}}}{\langle \bar{T}_{\text{model}} \rangle}, \quad (2.16)$$

where the bra–ket notation indicates an average over all measurements.

Figure 2.3 shows five examples of what this procedure might produce for a given model as a function of the arbitrary parameter x . Figure 2.3 (a) is what one would typically use to illustrate that a model correctly describes thrust as a function of x when measurements are made with all other parameters held fixed. Because different measurements across the database have different parameters held fixed, (b) is more representative of what this same method would yield in our case. In both (a) and (b), it is difficult to compare one model’s effectiveness to another, and we can only tell that model A consistently predicts the measured value. The nondimensionalization and normalization procedures applied in (c) and (d) clarify how well each model predicts

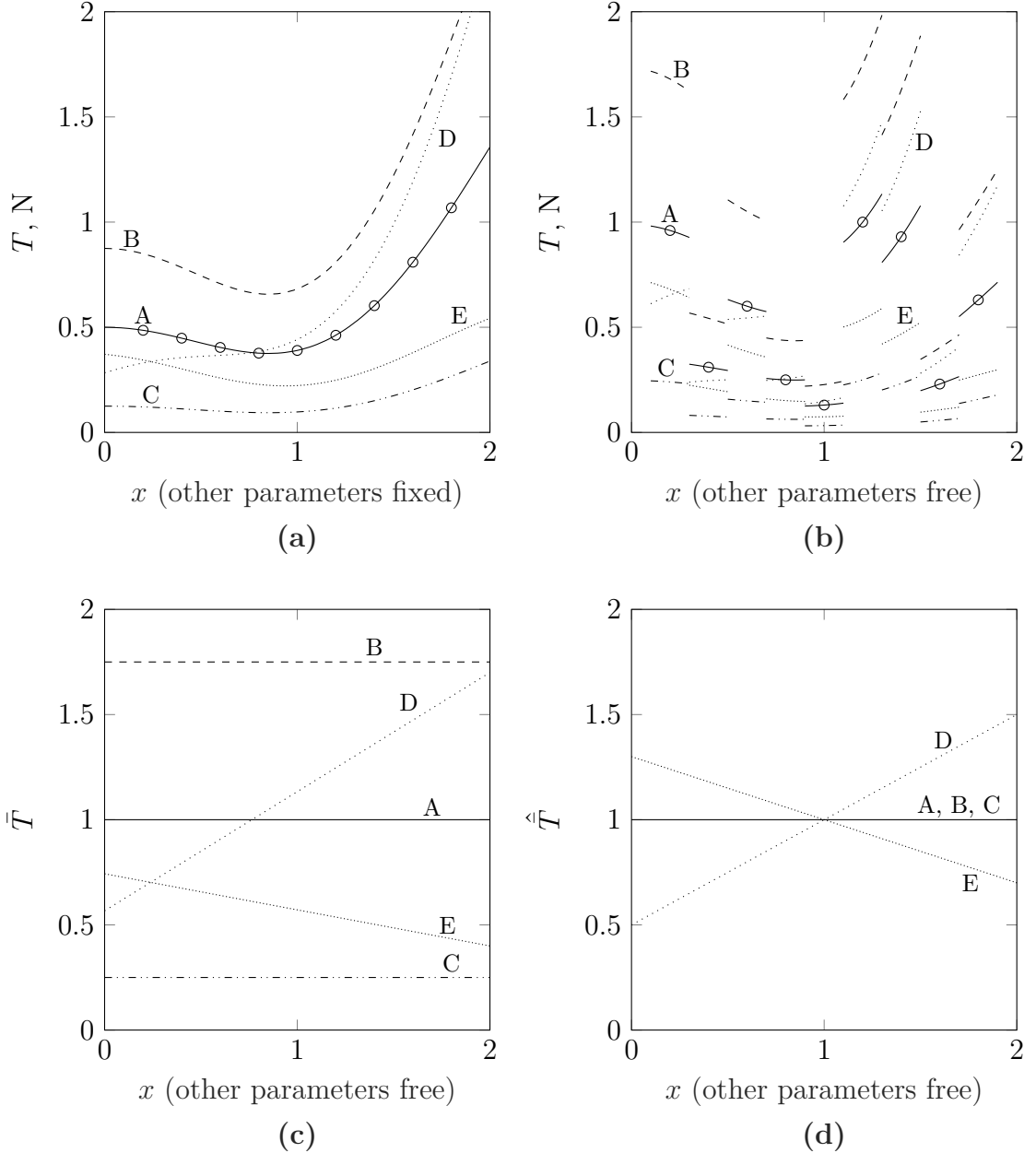


Figure 2.3: In (a), examples of how models A–E of T vary as a function of the arbitrary parameter x compared to data where all other parameters are held fixed. In (b), the same is shown except that parameters other than x are different for each measurement. Bottom, examples of how T and \hat{T} vary for those same models, showing only models D and E have incorrectly described the dependence of T on x .

the magnitude of thrust, and thrust scaling, respectively, as a function of x . From (c) and (d), we are able to deduce the following about models A–E:

- A. The model predicts the magnitude of the measurement, as well as how thrust varies as a function of x .
- B. The model overpredicts thrust, but correctly predicts how thrust varies as a function of x .
- C. The model underpredicts thrust, but correctly predicts how thrust varies as a function of x .
- D. The model overpredicts thrust, and predicts a different thrust dependence on x than that which is represented by the data.
- E. The model underpredicts thrust, and predicts a different thrust dependence on x than that which is represented by the data.

Because normalization decreases the slope of D, but increases the slope of E, we are able to compare the predictions of the two models. Otherwise, models that underpredict thrust will tend to have smaller slopes, as is illustrated by Fig. 2.3 (c).

We apply this methodology to examine how \hat{T} scales as a function of each controllable parameter of interest. In most cases, there are not enough data points for us to determine any high-order or periodic dependence of \hat{T} on a given controllable parameter, so we seek only to determine if \hat{T} is monotonically increasing or decreasing. Such behavior indicates that the thrust dependence is not captured by the model of interest.

For each parameter investigated, we make a linear fit of \hat{T} as a function of that parameter using a χ^2 test for goodness of fit. We weight each measurement by the inverse of the square of the error on that measurement. If the fit function for the parameter has a slope, and if the 95% confidence interval on that slope does not include 0, we conclude that the model over- or underpredicts thrust as a function of that parameter.

The database includes two types of controllable parameters: those that are discrete, such as geometrical terms, for which there are relatively few values recorded, and those that are continuous, such as current. For simplicity, the figures show only the mean \hat{T} value for each value of the discrete parameters, with error bars denoting the interquartile region. However, the linear fit of \hat{T} is to the total dataset as it is for continuous parameters.

2.5.2 Filtering method

In order to test the various models of the applied-field thrust component, we filter the thrust database for measurements for which that component dominates. To filter the data, we use the Tikhonov et al. model of the applied-field thrust, which has been most verified experimentally [14, 15, 22, 60], to establish whether the applied-field component is significant. If the prediction of the Tikhonov et al. model for a set of parameters is found to be a significant fraction of the thrust measurement, we can assume that the applied-field thrust component is dominant, and the models should all closely match the data, whether they predict the applied-field component or the sum of several components.

Due to the demonstrated effects of background pressures over 1 mTorr, we have the additional requirement that all data analyzed was gathered at or below this pressure except for in our investigation of background pressure effects, as is noted in Table 2.1 and Figs. 2.4 and 2.5. We chose the thresholds

$$\frac{T_{\text{Tikhonov}}}{T_{\text{measured}}} > 0.9 \text{ and } p_b \leq 1 \text{ mTorr.} \quad (2.17)$$

2.5.3 Parameters investigated

With data spanning a sufficiently varied parameter space, it is possible to determine which of these models correctly predicts thrust scaling as a function of a given

controllable parameter. For example, we can determine if $T_{\text{AF}} \propto r_a$ as predicted by Tikhonov et al. or if $T_{\text{AF}} \propto r_a^{1.6577}$ as Herdrich et al. predicted. In Sec. 2.7 we show how each model's prediction-to-measurement ratio varies as a function of each controllable parameter.

In addition to dimensional parameters such as J or B_A , we investigate several nondimensional parameters, most of which are geometric in nature, such as the anode to cathode radius, r_a/r_c . One nondimensional parameter that has not previously been explored with respect to AF-MPDTs describes the degree to which the anode inner surface follows the magnetic field contour. Contouring of the anode to the magnetic field was claimed by Tikhonov et al. to improve performance [10, 16], and this claim was experimentally verified by Tahara [61]. In order to describe the degree to which the anode geometry matches the magnetic field topology, we first model the on-axis magnetic field using the Biot-Savart law for a solenoid,

$$B(z) = B_{a0} \frac{r_B^3}{(r_B^2 + z^2)^{3/2}}, \quad (2.18)$$

where z is the axial distance from the end of the solenoid. To a reasonable approximation, an anode which is contoured to the magnetic field is one for which the magnetic flux through the anode throat, Φ_{a0} , is equal to the flux through the anode exit plane, Φ_{ae} . We define the nondimensional value

$$\bar{\Phi} = \frac{\Phi_{ae}}{\Phi_{a0}} = \frac{r_{ae}^2 r_B^3}{r_{a0}^2 (r_B^2 + l_a^2)^{3/2}}. \quad (2.19)$$

Physically, $\bar{\Phi} = 1$ represents an anode that is contoured to the magnetic field, while $\bar{\Phi} > 1$ represents an anode that diverges more rapidly than the magnetic field.

2.5.4 Application of data to models

Each of the models depends on r_a , but many thrusters have flared anodes for which we need to determine which anode radius to use. In all cases where the models do not specify otherwise, we use the average radius, $r_a = \frac{1}{2}(r_{a0} + r_{ae})$. Similarly, because solenoids have both inner and outer radii, we define $r_B = \frac{1}{2}(r_{Bi} + r_{Bo})$. We use the total anode length (either l_a or $l_{a1} + l_{a2}$) except in Eq. 2.19 for parameter $\bar{\Phi}$, where l_{a2} is used for delayed expansion conical anodes. The cathode length is determined by the propellant injection location as is described in Sec. 2.4.1. For B_A , we use the magnetic field strength that is reported at the tip of the cathode.

Error was not reported for all measurements. In order to lessen the bias on our conclusions by measurements without reported error, we assume the error on these values to be 15% of the measurement. This percentage is the largest reported error in the analyzed data.

2.6 Investigation of background pressure effects

We first examine the effects of background pressure on all measurements for which $\frac{T_{\text{Tikhonov}}}{T_{\text{measured}}} > 0.9$. Fig. 2.4 shows how $\hat{T}_{\text{Tikhonov}}$ behaves as a function of background pressure. We fit $\hat{T}(\log p_b)$ with a moving average over $1/10^{\text{th}}$ the span of $\log(p_b)$. Data outside six mean absolute deviations is ignored.

Despite the effects of background pressure on thrust demonstrated by Refs. [52, 56, 57], we see no significant upward or downward trend in the behavior of \hat{T} as a function of p_b . We attribute this observation to the symmetrical behavior illustrated in Fig. 2.2. We cannot assume, based on the results from only two thrusters, that the minimum on the border of regions II and III is at a fixed pressure for all thrusters and facilities. Furthermore, we do not have any data with all parameters other than p_b fixed that spans beyond region III with which to speculate about behavior in higher

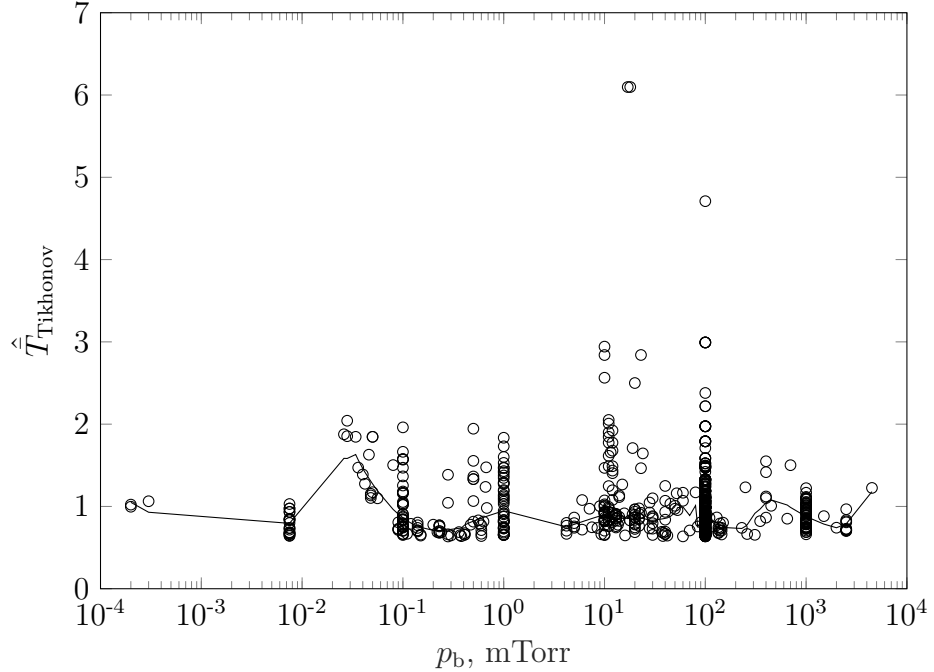


Figure 2.4: All data for which $\bar{T}_{\text{Tikhonov}} > 0.9$ as a function of background pressure. There is no upward trend between 1 and 10 mTorr despite the observation of such a trend for data gathered in Refs. [52, 56, 57].

pressure regimes. The only conclusion we can draw from Fig. 2.4 is that the pressure at which thrust is minimized is not universal across facilities, otherwise we would observe a local maximum about that pressure. Since there is no consistent pressure threshold below which data can be considered valid, verification of the absence of background pressure effects needs to be more highly prioritized in future experimental publications.

Because most measurements for a given thruster are recorded at a constant background pressure, we examine, in Fig. 2.5, the average $\hat{\bar{T}}$ value for each thruster operating at or below 0.1 mTorr, and for each thruster operating in the range of $0.1 \text{ mTorr} < p_b \leq 1 \text{ mTorr}$. We observe different average $\hat{\bar{T}}$ values for each thruster, but no correlation with pressure. Furthermore, Table 2.1 shows that for most models the relative standard deviation, \hat{s} , of the average nondimensionalized prediction, $\langle \bar{T} \rangle$, changes very little when the higher pressure data (≤ 1 mTorr) is included in

the analysis. This observation justifies our use of data gathered at ≤ 1 mTorr for all of the following results.

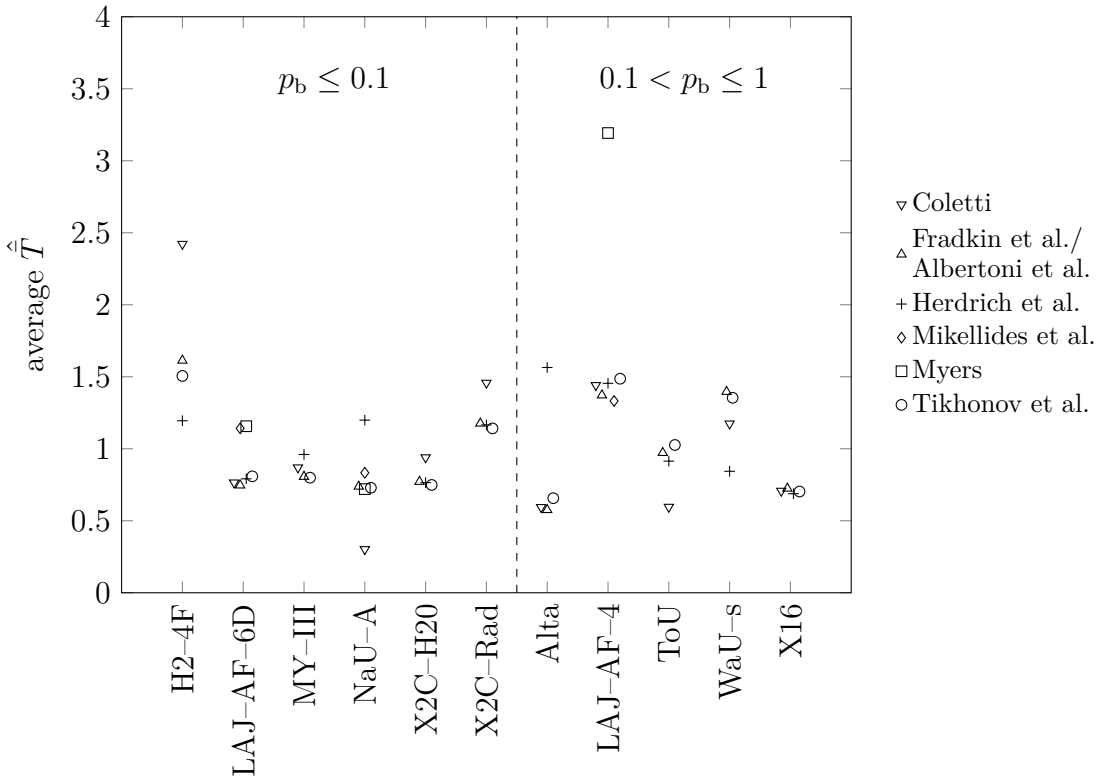


Figure 2.5: The average \hat{T} value for each thruster in the specified background pressure regimes (in mTorr) is shown for each model. There are larger differences in individual thrusters than in distinct pressure regimes.

2.7 Comparison of predictive accuracy

In Table 2.1, we show the average nondimensionalized prediction, $\langle \bar{T} \rangle$, and the relative standard deviation, \hat{s} , for each model. We see that the Alberttoni et al. model comes closest to predicting the average measurement value. This is as expected, since this model scales the Fradkin et al. model by a constant, $k_{\text{Alberttoni}}$, such that $k_{\text{Alberttoni}} \langle \bar{T}_{\text{Fradkin}} \rangle = 1$. Because $\langle \bar{T}_{\text{Fradkin}} \rangle$ was found by Alberttoni et al. using a different dataset than is used here, we find a different average value, which results in an

average overprediction of 14% by their model. The Mikellides and Turchi model also comes close to predicting the measured value, but was limited to a smaller dataset due to its inability to accommodate recessed cathodes.

The models of Herdrich et al. and Mikellides and Turchi yield the smallest relative standard deviation. The model by Sasoh and Arakawa yields the largest relative standard deviation. The range of values reported in Table 2.1 for this model correspond to the temperatures and exhaust velocities yielding the smallest and largest relative standard deviations. For data gathered at ≤ 1 mTorr, we found the smallest relative standard deviation corresponds to $T_e = 0.9$ eV and $u_{z,ae} = 0.8$ km/s. The largest relative standard deviation corresponds to $T_e = 1.5$ eV and $u_{z,ae} = 86$ km/s. We conclude that more developed models are needed to determine all input values based on controllable parameters.

The results of our tests for the missed dependencies of each model are given in Table 2.2. By missed dependency, we mean the degree to which a model over- or underpredicts thrust as a function of a given parameter. Examples of the analyses are shown in Figs. 2.6, 2.7, 2.8, 2.10, and 2.11. For most models, few missed dependencies were confirmed within a 95% confidence interval. The exceptions are the Myers and Mikellides and Turchi models, which each miss dependencies on each parameter tested, however some of the geometric parameters are likely correlated, since larger thrusters tend to be larger in all dimensions. The Sasoh and Arakawa model also has many missed dependencies. The values for this model correspond to the minimum and maximum slopes found using the full range of possible ion temperatures and exhaust velocities. Due to the wide range of possible slopes for most parameters, this model is excluded from all figures. The models of Tikhonov et al., Fradkin et al., and Albertoni et al. have the fewest missed dependencies.

The largest deviations between prediction and experiment over the domain for which we have data occur for the dependence of \hat{T} on electrode radii. Figure 2.6

Table 2.1: Mean \bar{T} value and relative standard deviation (\hat{s}) for each model.

p_b (mTorr)	Albertoni et al.	Coletti et al.	Fradkin et al.	Herdrich et al.	Mikellides and Turchi	Myers	Sasoh et al.	Tikhonov et al.
≤ 1	$\langle \bar{T} \rangle$ \hat{s}	1.14 0.38	2.40 0.67	4.54 0.38	1.33 0.29	0.86 0.29	5.08 0.48	0.51–9.7 0.82–3.1
≤ 0.1	$\langle \bar{T} \rangle$ \hat{s}	1.24 0.38	3.27 0.53	4.97 0.38	1.42 0.27	0.75 0.23	5.96 0.37	0.66–8.7 0.64–3.5

Table 2.2: Calculated slope of linear fit of \hat{T} of each model for each parameter using data gathered at ≤ 1 mTorr. Entries with a 95% confidence bounds of a non-zero slope are shown in bold.

Coletti	Fradkin et al./Albertoni et al.	Herdrich et al.	Mikelbäck and Turchi	Myers	Sasoh et al.	Tikhonov et al.
r_c (cm $^{-1}$)	-0.23	-0.18	0.45	-1.2	-3.4	-0.91, -0.0066
l_c (cm $^{-1}$)	-0.033	-0.016	0.0089	-0.034	-0.073	-0.065 , 1.4e-8
r_a (cm $^{-1}$)	-0.068	-0.059	0.18	-0.17	-0.47	-0.25, -0.0012
l_a (cm $^{-1}$)	-0.027	-3.5e-4	0.019	-0.022	-0.063	-0.012 , 0.066
r_B (cm $^{-1}$)	-0.073	-0.049	0.098	-0.20	-0.58	-0.24, -0.0012
M_i (u $^{-1}$)	0.0021	0.0060	0.0057	-0.0081	-0.039	-0.0033 , 2.5e-4
ϵ_i (eV $^{-1}$)	0.0033	-0.018	-0.018	-0.026	-0.075	5.6e-5, 0.023
J (kA $^{-1}$)	0.22	0.063	0.12	1.1	3.7	2.2e-4, 1.1
B_A (T $^{-1}$)	-0.36	0.39	0.40	1.3	3.9	-0.61 , 0.30
\dot{m} (s/g)	0.40	0.023	0.23	9.8	24	-2.0, 0.57
$\bar{\Phi}$	0.0026	0.0051	-0.0021	0.43	1.2	1.3e-4 , 0.0073
r_a/r_c	-0.024	0.025	0.089	-0.21	-0.61	-0.11, 0.36
l_c/l_a	0.0017	-0.049	-0.014	0.15	0.42	-0.12 , 8.9e-8
r_{ae}/r_{a0}	0.0075	0.025	-0.018	-0.55	-1.6	5.9e-4 , 0.041
l_c/r_c	-0.018	-0.011	0.0031	-0.026	-0.057	-0.030 , 8.5e-9
l_a/r_a	-0.16	0.035	-0.022	-0.079	-0.23	-0.068 , 0.080

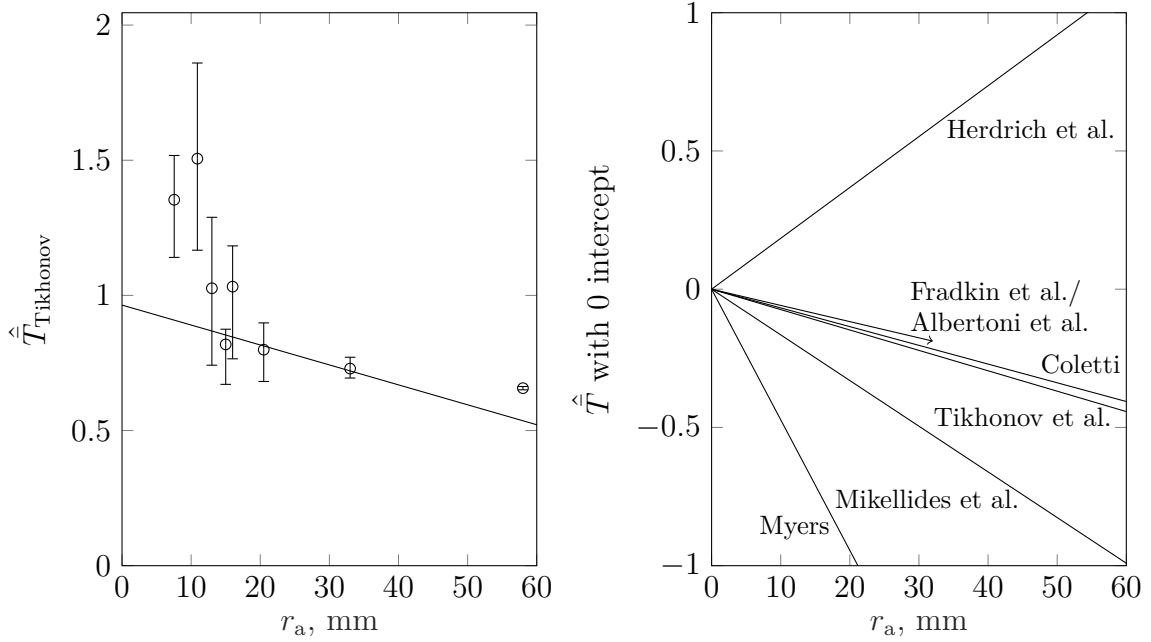


Figure 2.6: Left, the mean value of $\hat{T}_{\text{Tikhonov}}$ as a function of r_a is shown with error bars representing the interquartile region. Right, the linear fits for each model are shown with a common intercept. All data were taken at or below 1 mTorr.

shows the fit function for $\hat{T}(r_a)$ for each model. While the Herdrich et al. model was derived specifically to capture the thrust dependence on anode radius missed by the Tikhonov et al. model [14], it overpredicts the thrust because the empirical model of Herdrich et al. was made using a different dataset than that used here. Because the slope changes substantially depending on which dataset is used, there is likely either a more complicated dependence on anode radius than can be described by a power law fit, or an additional unknown parameter upon which thrust depends. While $\hat{T}_{\text{Tikhonov}}$ and \hat{T}_{Fradkin} have similar slopes as a function of anode radius, we see in Fig. 2.7 that the \hat{T} values diverge as a function of our nondimensionalized electrode radius, r_a/r_c , indicating that the electrode aspect ratio is also a relevant parameter to thrust scaling.

There is also a substantial deviation between prediction and experiment as a function of the solenoid radius (Fig. 2.8). Only the models of Sasoh and Arakawa and Coletti attempt to capture the influence of this parameter, however we observe

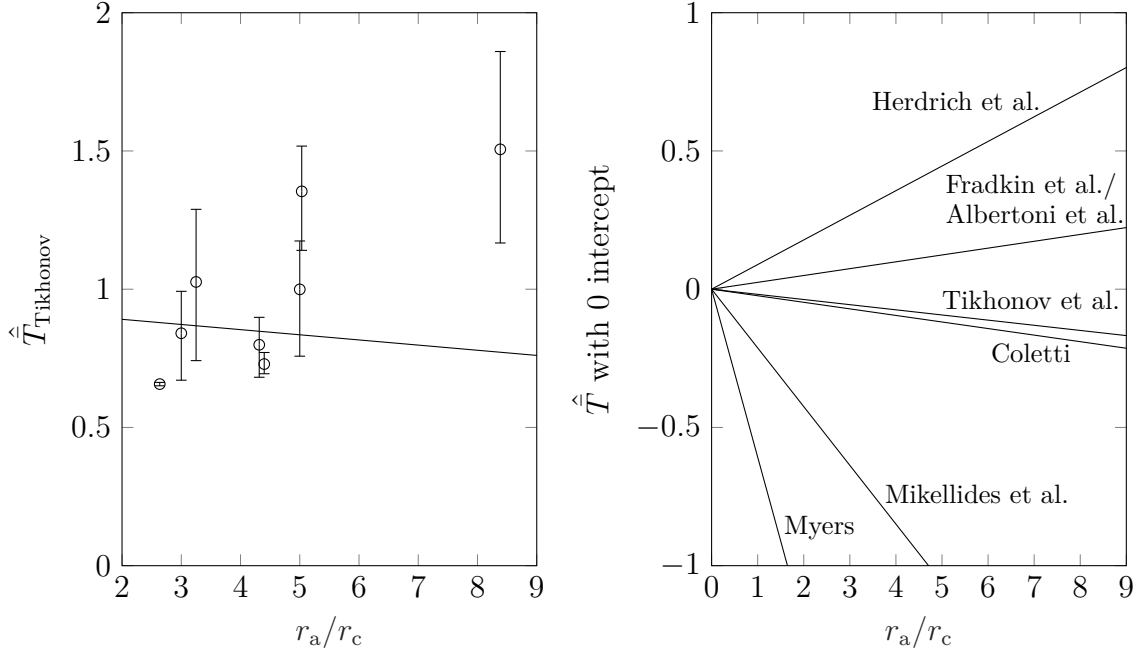


Figure 2.7: Left, the mean value of $\hat{T}_{\text{Tikhonov}}$ as a function of r_a/r_c is shown with error bars representing the interquartile region. Right, the linear fits for each model are shown with a common intercept. All data were taken at or below 1 mTorr.

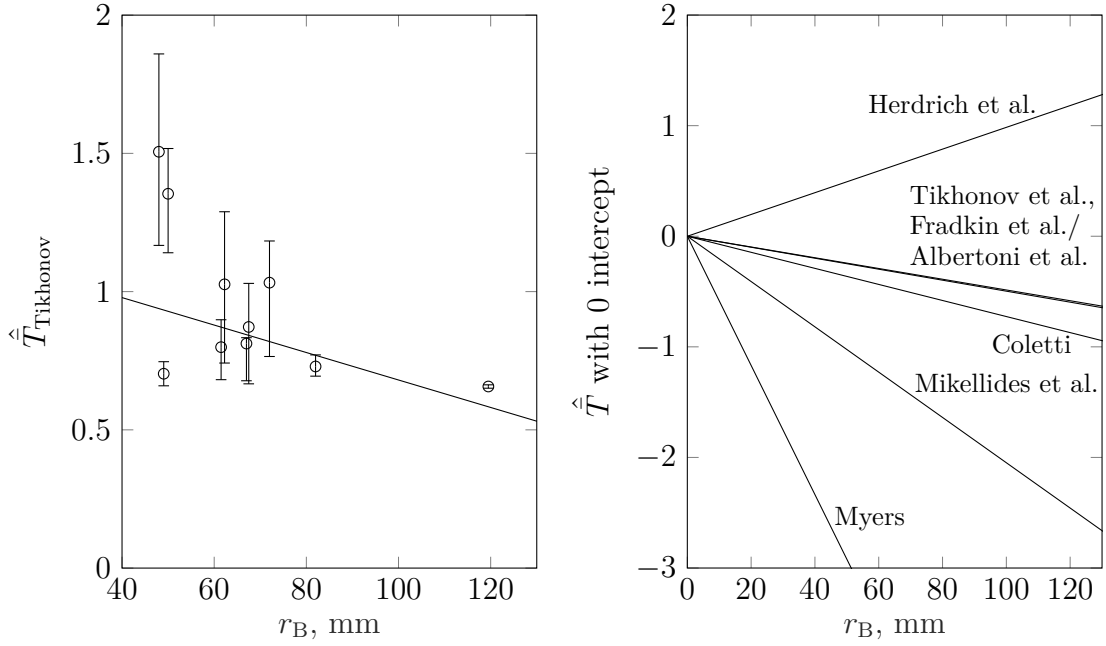


Figure 2.8: Left, the mean value of $\hat{T}_{\text{Tikhonov}}$ as a function of r_B is shown with error bars representing the interquartile region. Right, the linear fits for each model are shown with a common intercept. All data were taken at or below 1 mTorr.

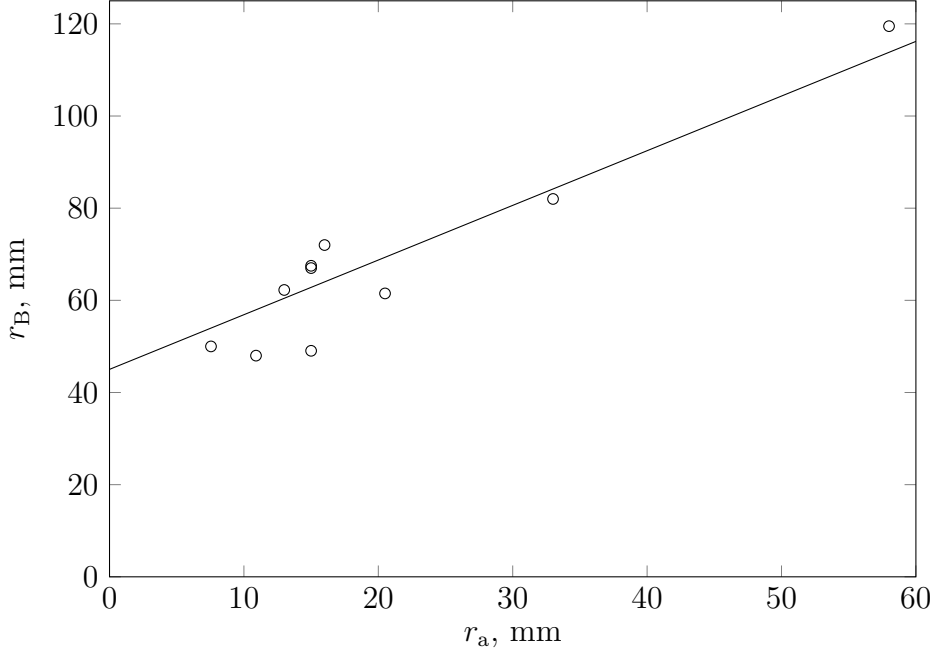


Figure 2.9: Correlation between solenoid and anode radii for data taken at or below 1 mTorr.

nearly identical behavior in Figs. 2.6 and 2.8. This consistent behavior despite a change in prediction indicates that there is a correlation between anode and solenoid radii, which we show to be the case in Fig. 2.9. Tests performed with different solenoid radii for a fixed anode radius [61] and with different anode radii for a fixed solenoid radius [52] show that thrust increases with each of these parameters.

Because the correlation between anode and solenoid radii makes it difficult to determine which of these variables contributes to thrust, we look at $\bar{\Phi}$, which incorporates both parameters into a single one. We see in Fig. 2.10 that most models deviate substantially from measurement as a function of this variable, where large values typically result in overpredictions.

Most models correctly describe thrust dependence on current, magnetic field strength, and mass flow rate, and even those with missed dependencies typically have slopes corresponding to small changes in \hat{T} over the domain of a given parameter. However, we find that the Myers model overpredicts thrust dependence on each

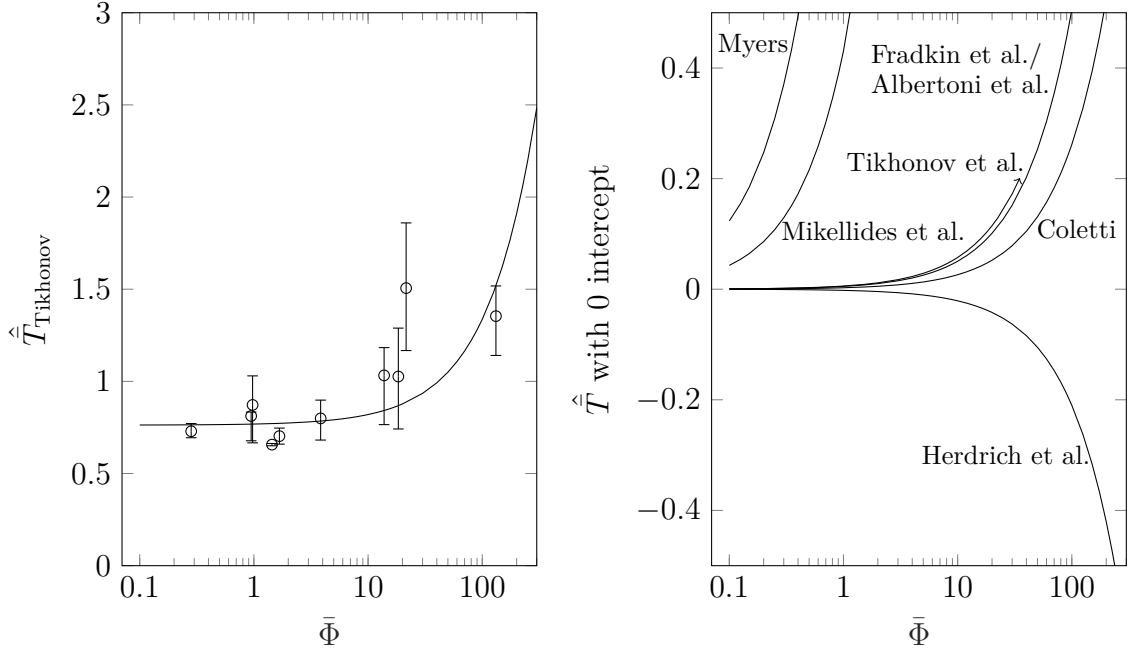


Figure 2.10: Left, the mean value of $\hat{T}_{\text{Tikhonov}}$ as a function of $\bar{\Phi}$ is shown with error bars representing the interquartile region. Right, the linear fits for each model are shown with a common intercept. All data were taken at or below 1 mTorr.

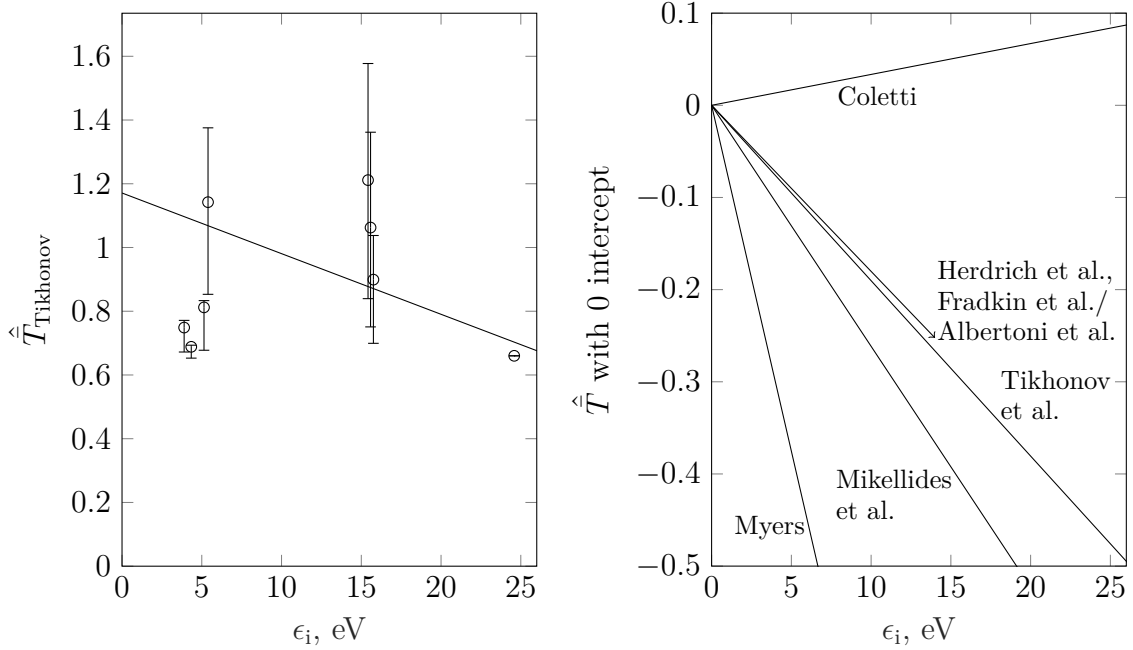


Figure 2.11: Left, the mean value of $\hat{T}_{\text{Tikhonov}}$ as a function of ϵ_i is shown with error bars representing the interquartile region. Right, the linear fits for each model are shown with a common intercept. All data were taken at or below 1 mTorr.

of these parameters. By comparing T_{Myers} to T_{Tikhonov} , we see that this overprediction must be a result of correlations with the electrode aspect ratio and/or the cathode length. The Mikellides and Turchi model also overpredicts thrust dependence on J , B_A , and \dot{m} , but $T_{\text{Mikellides}}$ is not easily comparable with other models. Nonetheless, while the Mikellides and Turchi model yields one of the smallest relative standard deviations and on average comes close to predicting the magnitude of a measurement, it fails to predict performance as a function of the controllable parameters of interest.

In implementing the model of Mikellides and Turchi, we assumed that the ionization factor, $\bar{Y} = 1$. We expect this factor to decrease with increasing ionization energy, which would increase the slope of $\hat{T}_{\text{Mikellides}}$ in Fig. 2.11. However, the agreement between prediction and measurement for the models of Coletti, Fradkin et al., and Tikhonov et al. which predict no dependence, suggests that while ionization energy affects the electrode voltage [58], it does not strongly influence the generated thrust. We see in Fig. 2.11 that $\hat{T}_{\text{Tikhonov}}$ is decreasing slightly, whereas we would expect a positive slope if alkali propellants benefited thrust generation.

2.8 Summary

We have shown that several of the existing models fail to describe the data as a function of specific controllable parameters, while groups of models seem to describe the data despite making different predictions from one another. We find that while the models predicting $T_{\text{AF}} \propto JB_{\text{Ar}}$ approximately describe the measured performance, each of the existing models incorrectly describes the thrust dependence on electrode and solenoid geometry. Specifically, we find that the applied-field thrust component depends on the nondimensional parameter $\bar{\Phi}$ and that this dependence is not captured by any model in the literature. In the following chapter, we will empirically determine

the dependence of thrust on a number of nondimensional parameters, including $\bar{\Phi}$, so that we can gain insight into the underlying physics.

Chapter 3

Empirical Model²

We now derive a new model empirically by assuming we know each of the parameters upon which the thrust depends [62]. Using this empirical model, we will attempt to shed light on the physical mechanism responsible for the disagreement between existing models and measurement.

3.1 **Π-product-corrected Model**

3.1.1 Method

We assume the general functional expression for the applied-field component of thrust,

$$T_{\text{AF}} = f(J, B_A, r_{a0}, r_{ae}, l_a, r_c, l_c, r_B). \quad (3.1)$$

There are nine parameters and four independent dimensions (mass, length, time, and charge), so per the Buckingham Π theorem, we can reduce this function to five nondimensional Π products, where Π_i is the i^{th} Π product. We choose the parameters

²This chapter is based on work being prepared to be submitted for publication and previously presented in [20]: W. J. Coogan and E. Y. Choueiri, “A Critical Review of Thrust Models for Applied-Field Magnetoplasmadynamic Thrusters,” In *AIAA Propulsion and Energy 2017*, AIAA-2017-4723, Atlanta, GA, July 10–12, 2017. doi:10.2514/6.2017-4723

$$\Pi_1 = \frac{T_{\text{AF}}}{JB_{\text{A}}r_{\text{a}}}, \quad (3.2)$$

$$\Pi_2 = \bar{\Phi}(r_{\text{a}0}, r_{\text{ae}}, l_{\text{a}}, r_{\text{B}}), \quad (3.3)$$

$$\Pi_3 = \frac{r_{\text{a}}}{r_{\text{c}}}, \quad (3.4)$$

$$\Pi_4 = \xi + \frac{l_{\text{c}}}{l_{\text{a}}}, \text{ where } \xi \text{ is a constant and} \quad (3.5)$$

$$\Pi_5 = \frac{r_{\text{ae}}}{r_{\text{a}0}}. \quad (3.6)$$

Using these Π products, we can derive a formula by assuming the general form

$$T_{\text{AF}} = k JB_{\text{A}}r_{\text{a}}\Pi_2^{\kappa_2}\Pi_3^{\kappa_3}\Pi_4^{\kappa_4}\Pi_5^{\kappa_5}, \quad (3.7)$$

where κ_i is the power for the i^{th} Π product found by fitting to the data, and k is a constant such that $\langle \bar{T}_{\text{AF}} \rangle = 1$. We solve for κ_2 by assuming that κ_3 , κ_4 , and $\kappa_5 = 0$, and minimizing the standard deviation of \hat{T}_{AF} . Then, knowing κ_2 , we can solve for κ_3 continuing the assumption that κ_4 and $\kappa_5 = 0$, and so on until κ_5 is determined. This method provides an approximate value for each κ_i , which can be improved with subsequent iterations until the κ_i values converge.

Since $l_{\text{c}}/l_{\text{a}}$ can be negative, and since we require that $T_{\text{AF}} > 0$, we choose a constant ξ such that $\min(\Pi_4) > 0$. $\xi = 10$ is used for all analyses.

3.1.2 Results

We show our empirical solution to T_{AF_j} in Table 3.1, where the index j indicates the number of corrections to the initial solution using only Π_1 . We see that the relative standard deviation improves markedly after one correction, but then converges rapidly to $\hat{s} = 0.267$. Table 3.2 gives the slopes of \hat{T}_{AF} as a function of each parameter for each iteration of the Π -product-corrected model. The initial slopes are the same as those for the Tikhonov et al. model since $\hat{T}_{AF_0} = \hat{T}_{\text{Tikhonov}}$. The number of parameters the model fails to capture decreases with each iteration until at last only one is remaining.

Table 3.1: Evolution of empirical model over successive iterations of Π products.

Iteration	Model	\hat{s}
T_{AF_0}	$0.14JB_A r_a$	0.356
T_{AF_1}	$0.14JB_A r_a \bar{\Phi}^{-0.13}$	0.286
T_{AF_2}	$1.12JB_A r_a \bar{\Phi}^{-0.13} (r_a/r_c)^{-0.20}$	0.276
T_{AF_3}	$1.17JB_A r_a \bar{\Phi}^{-0.13} (r_a/r_c)^{-0.20} (10 + l_c/l_a)^{-0.67}$	0.269
T_{AF_4}	$1.17JB_A r_a \bar{\Phi}^{-0.13} (r_a/r_c)^{-0.30} (10 + l_c/l_a)^{-0.67}$	0.267

We found Π_5 to be unnecessary to further improve the agreement with measurement, and so left $\kappa_5 = 0$. The only κ value we solved for more than once is κ_3 , but we found that the relative standard deviation was only marginally improved. All slopes are 0 within the certainty of the data except for as a function of M_i , which was not included in our original list of independent variables. This parameter makes the final model underpredict thrust by < 0.6% per u. Adding M_i to our list of variables requires an additional variable for normalization. Subsequently, a new solution requires two additional Π products. We deem the added complexity insufficiently warranted by such a weak dependence.

The results of the Π -product-corrected model are shown in Fig. 3.1. We see excellent agreement between prediction and measurement across four orders of magnitude.

Table 3.2: Calculated slope of linear fit to \hat{T} for each iteration of the Π -product-corrected model using data gathered at ≤ 1 mTorr. Entries with a 95% confidence bounds of a non-zero slope are shown in bold.

	\hat{T}_{AF_0}	\hat{T}_{AF_1}	\hat{T}_{AF_2}	\hat{T}_{AF_3}	\hat{T}_{AF_4}
r_c (cm $^{-1}$)	-0.19	0.10	0.58	0.10	0.10
l_c (cm $^{-1}$)	-0.016	0.035	0.15	0.018	0.015
r_a (cm $^{-1}$)	-0.074	0.060	0.22	0.046	0.034
l_a (cm $^{-1}$)	-0.0044	0.0017	0.015	0.0073	0.0068
r_B (cm $^{-1}$)	-0.050	0.036	0.18	0.024	0.020
M_i (u $^{-1}$)	0.0063	0.0056	0.027	0.0061	0.0054
ϵ_i (eV $^{-1}$)	-0.019	-0.019	-0.091	-0.020	-0.018
J (kA $^{-1}$)	0.053	0.092	0.38	0.092	0.076
B_A (T $^{-1}$)	0.41	0.42	2.0	0.44	0.39
\dot{m} (s/g)	-0.026	0.14	0.43	0.12	0.083
$\bar{\Phi}$	0.0057	-0.0028	-0.011	-0.0019	-0.0015
r_a/r_c	-0.019	0.055	0.076	0.023	0.0029
l_c/l_a	-0.041	0.079	0.41	0.035	0.034
r_{ae}/r_{a0}	0.030	-0.030	-0.11	-0.017	-0.013
l_c/r_c	-0.010	0.020	0.092	0.0096	0.0082
l_a/r_a	0.040	-0.051	-0.17	-0.021	-0.012

3.2 Physical interpretation of empirical model

The relative magnitudes of each of the described Π products indicates their relative importance. Aside from the already established $JB_A r_a$ scaling, $\bar{\Phi}$ is dominant, with the nondimensional electrode radius and length serving only as minor correction terms. We previously stated that $\bar{\Phi} > 1$ means that the anode diverges more rapidly than the applied magnetic field, but we expect this divergence to increase voltage (due to increased resistance across the magnetic field) rather than decrease thrust. However, a magnetic field that expands more slowly than the anode is effectively freezing the charged particles to a surface of constant flux, reducing the volume over which the Lorentz force acts.

Using Eq. 2.18, and assuming the initial radius at $z = 0$ to be r_{a0} , we find this radius of constant flux at the anode exit plane to be

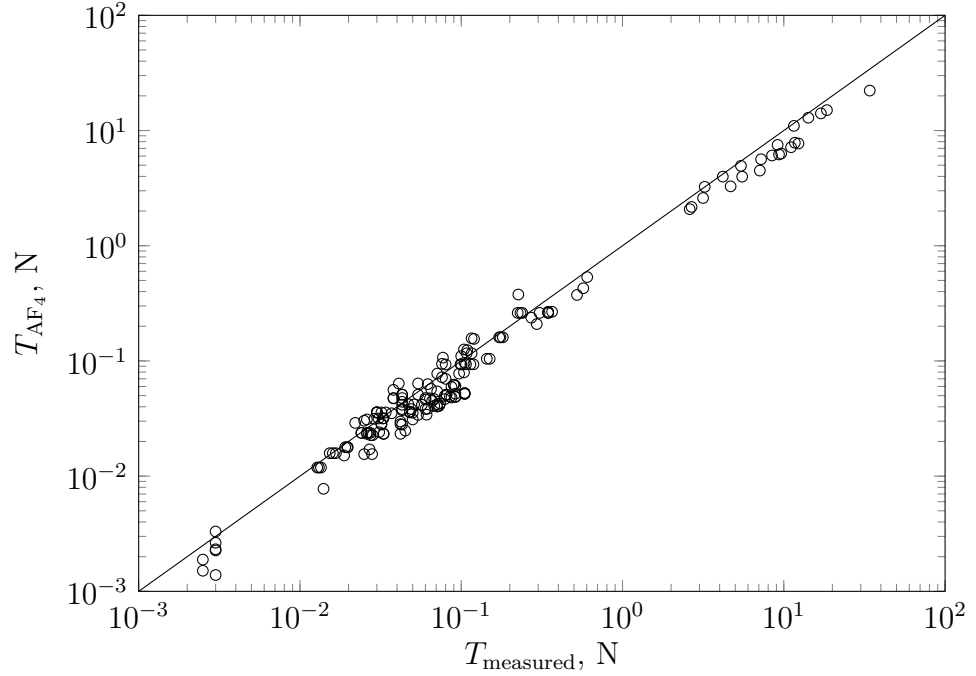


Figure 3.1: Comparison of T_{AF_4} prediction to measurement for data taken at or below 1 mTorr.

$$r_{\text{ae}-\Phi} = r_{\text{a}0} \sqrt{\frac{(r_{\text{B}}^2 + l_{\text{a}}^2)^{3/2}}{r_{\text{B}}^3}}. \quad (3.8)$$

We assume that there is some effective anode radius at the exit plane, $r_{\text{ae-eff}}$, such that $r_{\text{ae}-\Phi} \leq r_{\text{ae-eff}} \leq r_{\text{ae}}$, for all $r_{\text{ae}-\Phi} \leq r_{\text{ae}}$. The plasma within the anode volume is often collisional, and so we do not expect the charged particles to necessarily be completely frozen to an initial flux surface, but rather anticipate that they will expand to some point between the radius of constant flux and the anode radius at the exit plane, depending on the degree to which they are confined. The effective anode radius relevant to the Lorentz force is then

$$r_{\text{a-eff}} = \frac{r_{\text{a}0} + r_{\text{ae-eff}}}{2}, \quad (3.9)$$

where we approximate the flux surface as a cone (shown schematically in Fig. 3.2).

The degree to which $r_{\text{ae-eff}}$ extends beyond $r_{\text{ae-}\Phi}$ can be expressed by the nondimensional value

$$\hat{r}_{\text{a-}\Phi} = \frac{r_{\text{ae-eff}} - r_{\text{ae-}\Phi}}{r_{\text{ae}} - r_{\text{ae-}\Phi}}, \quad (3.10)$$

where $0 \leq \hat{r}_{\text{a-}\Phi} \leq 1$.

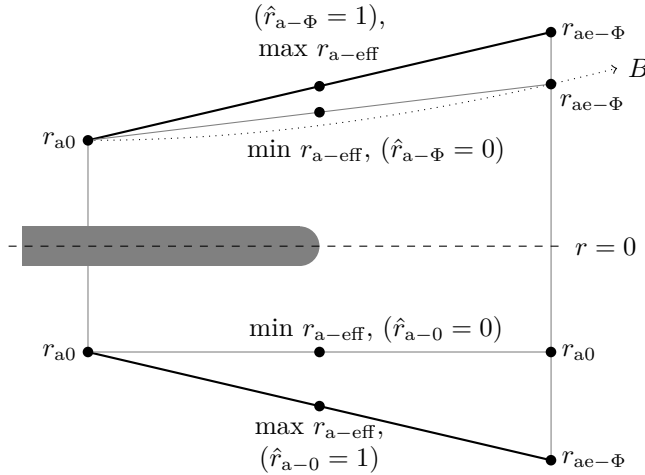


Figure 3.2: Schematic of the effective anode radius using either the surface of constant flux (top half) or the physical anode dimensions (bottom half).

We do not expect a universal $\hat{r}_{\text{a-}\Phi}$ value to exist, since this term depends on the degree of confinement, which is a function of the gasdynamic and magnetic pressures, each of which varies as a function of the operating conditions. However, we do expect better agreement between prediction and experiment for intermediate values than for the extremes, since we assume that the plasma is collisional and that the magnetic field is restricting radially outward flow. By iterating over all possible $\hat{r}_{\text{a-}\Phi}$ values and solving for the relative standard deviation, \hat{s} , of $kJB_{\text{Ar}}r_{\text{ae-eff}}/T$, we see in Fig. 3.3 that there is indeed a substantial decrease in the relative standard deviation for intermediate values of $\hat{r}_{\text{a-}\Phi}$, with a minimum of $\hat{s} = 0.289$ at $\hat{r}_{\text{a-}\Phi} = 0.43$.

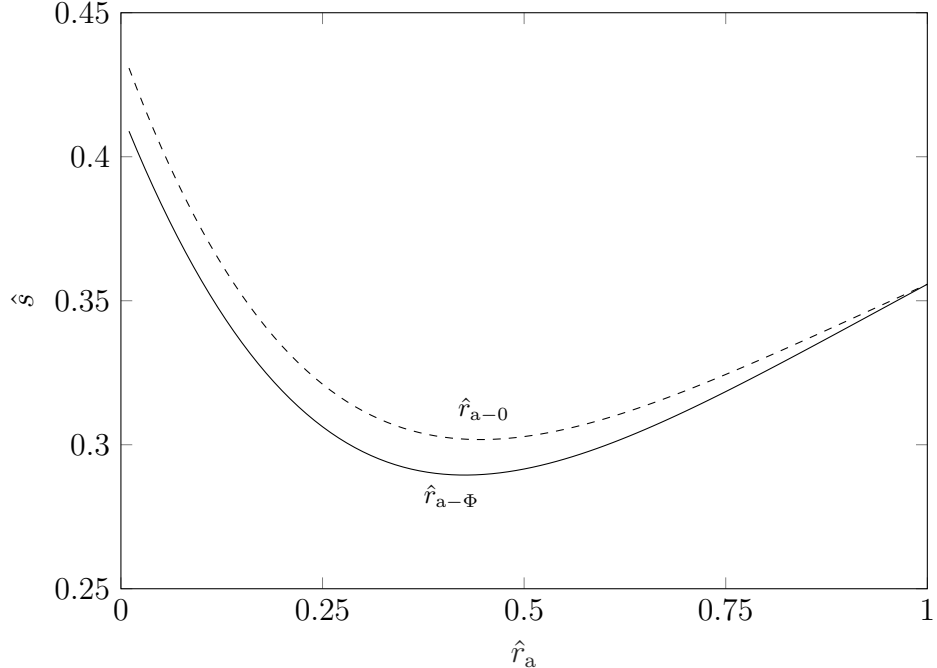


Figure 3.3: The relative standard deviation is shown as a function of \hat{r} for $kJB_{\text{Ar}}r_{\text{a-eff}}/T$. All data were taken at or below 1 mTorr.

So far, we have arbitrarily asserted that $r_{\text{a}} = \langle r_{\text{a}0}, r_{\text{ae}} \rangle$. In order to verify that the reduction in \hat{s} for certain $\hat{r}_{\text{a}-\Phi}$ values is not actually due to this arbitrary choice, we perform the same iteration over all possible physical anode radii. For consistency, we define

$$\hat{r}_{\text{a}-0} = \frac{r_{\text{ae-eff}} - r_{\text{a}0}}{r_{\text{ae}} - r_{\text{a}0}}, \quad (3.11)$$

where $0 \leq \hat{r}_{\text{a}-0} \leq 1$, as depicted in Fig. 3.2. Again, we see improved agreement between model and prediction, but to a lesser extent than was found using $\hat{r}_{\text{a}-\Phi}$. The best agreement is found at $\hat{r}_{\text{a}-0} = 0.45$, where $\hat{s} = 0.302$. The corresponding effective radius is less than 1/4 the distance between the radius at the throat and that at the exit plane rather than half as was initially assumed. However, 77% of the data used in this analysis are represented by magnetically restricted anodes, meaning we anticipate $r_{\text{ae-eff}} < r_{\text{ae}}$ based on our previous assertion that the volume over which the Lorentz

force acts is restricted. If instead we select only the data for which $r_{ae-\Phi} \geq r_{ae}$, the relative standard deviation decreases monotonically for increasing \hat{r}_{a-0} , and continues decreasing even if the domain is expanded until $r_{a-\text{eff}} = r_{ae}$.

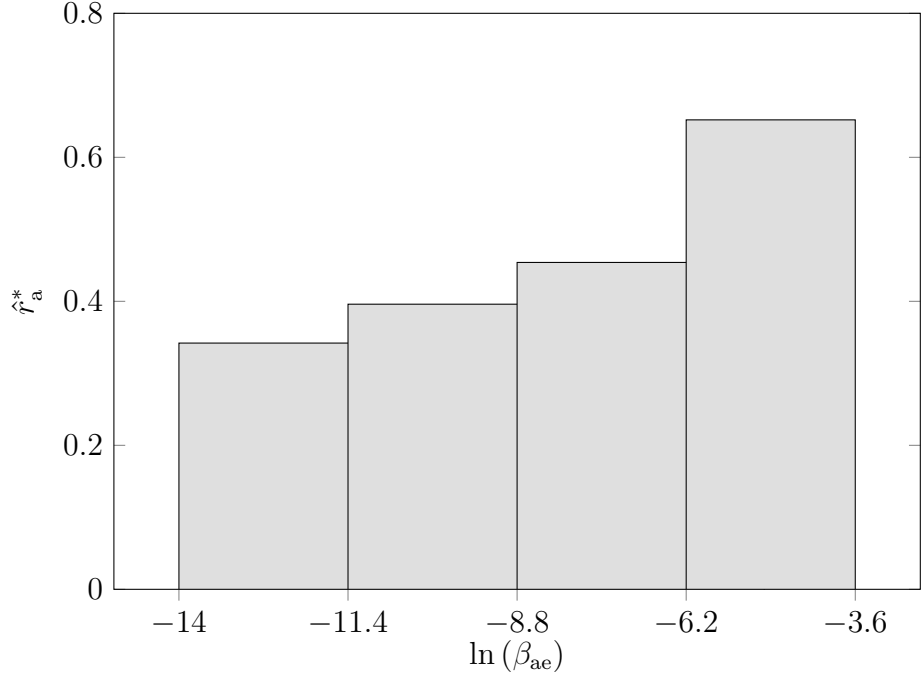


Figure 3.4: Bar plot showing the increase of the effective anode radius as the ratio of the gasdynamic pressure to magnetic pressure increases. All data were taken at or below 1 mTorr.

We see further evidence that the effective volume over which the Lorentz force acts is reduced by slowly diverging magnetic fields if we look at the ratio of gasdynamic to magnetic pressure at the anode exit plane,

$$\beta_{ae} = \frac{n_i k_B T_i}{B_{ae}^2 / 2\mu_0}, \quad (3.12)$$

where k_B is the Boltzmann constant, n_i is the ion number density, and B_{ae} is the applied field strength at the anode exit plane. We assume that $T_i = 2$ eV and solve for the magnetic field using Eq. 2.18. We find the ion density by assuming the ion velocity at the exit plane to be T_{AF_0}/\dot{m} , so that

$$n_i = \frac{\dot{m}^2}{M_i \pi r_{ae}^2 T_{AF_0}}. \quad (3.13)$$

We expect that as β_{ae} increases, the value of $\hat{r}_{a-\Phi}$ at which \hat{s} is minimized, or \hat{r}_a^* , will correspondingly increase due to the gasdynamic pressure forcing the ions across field lines. We group the data in bins by β_{ae} value in Fig. 3.4 and see this is in fact the case. This dependence indicates that the effective volume over which the Lorentz force acts is governed by a balance of the gasdynamic and magnetic pressures in thrusters for which the anode expands more rapidly than the magnetic field.

3.3 Summary

Our empirical fit to the data using dimensional analysis shows that we can better predict the data by accounting for the degree to which the anode inner surface follows the magnetic field contour. This improved agreement, suggests that a substantial cause for disagreement between $JB_A r_a$ thrust models and measurement is a result of variability in the effective anode radius. This variability appears to be due to the radial forces within the anode, which can restrict the volume of the plasma so that it is less than the volume of the anode. As a result, the volume over which the Lorentz force acts is also reduced.

Chapter 4

Derivation of Thrust Scaling

Parameters³

In the previous chapter, we found that the effective anode radius relevant to a thrust calculation is a function of the radial forces on the plasma within the anode. In this chapter, we will first modify the rigid-rotor thrust model developed by Fradkin et al. [8] for cylindrical thrusters so that it is better suited to conical anode geometries. Then, we will examine the scaling of the effective anode radius using a radial momentum balance. We will discuss different mechanisms by which the radial forces within the anode may contribute to the thrust.

4.1 Modified rigid-rotor model

Of the theoretical models (as opposed to empirical models), the models of Tikhonov et al. and Fradkin et al. most accurately predict measurement. However, these two models are based on different thrust mechanisms. Tikhonov et al. assume that thrust is generated by a Lorentz force resulting from Hall currents and a diverging magnetic field, whereas Fradkin et al. assume that thrust is generated when the swirling plasma

³This chapter is based on work being prepared to be submitted for publication.

expands in a magnetic nozzle and is redirected axially. Because the thrust due to the expansion of the swirling plasma in the magnetic nozzle is approximately an order of magnitude greater than the Hall thrust [26, 27, 28], and further because the Fradkin et al. theory is more applicable to anodes enclosed by the solenoid (when there is no radial component of the magnetic field within the anode), we use the rigid-rotor thrust model as a starting point for our derivation of scaling parameters relevant to thrust generation.

The model of Fradkin et al. has two significant shortcomings that must be addressed before it can be applied to a wide variety of thrusters. First, the anode radius is not well defined for conical thrusters, and we demonstrated in the previous chapter that the effective radius can change as a function of the radial force balance. This implies that, even for a single thruster, the effective anode radius may not be constant. Second, the rate of rotation of the plasma is found with the assumption of a constant radial plasma density, which, even in the quasi-one-dimensional flow approximation, is not a valid assumption for a diverging anode, since the plasma density will decrease axially and, therefore, radially.

4.1.1 Assumptions

In order to apply the rigid-rotor thrust model to the more general case of the conical thruster, we assume that:

1. All acceleration within the anode volume is azimuthal, and that the axial velocity is approximately constant and equal to the ion sound speed. Conversion of this azimuthal velocity to axial velocity occurs downstream of the anode in the magnetic nozzle.

2. The density is, to first order, a function of axial position, and is approximately constant radially out to the anode wall for a given distance z from the anode throat.
3. The plasma rotates rigidly at a given axial position. We also assume that the cathode stops at the anode throat since this is typically the case for thrusters in the literature for the past 25 years. In comparison, Fradkin et al. model the plasma as containing a void for the cathode for the entire length of the anode.
4. There is a maximum radius, r_{sep} , such that $r_{\text{a}0} \leq r_{\text{sep}} \leq r_{\text{ae}}$, where the plasma flow separates from the anode due to the pinching component of the Lorentz force overcoming the radial force outward. When the outward radial force is greater than the inward radial force along the entire length of the anode, separation occurs at the anode exit plane.
5. The magnetic field is strictly axial and constant in magnitude within the anode volume.

Our first assumption, that the axial velocity is approximately constant within the anode volume, is only valid at low currents or high mass flow rates where $\frac{T_{\text{GD}}}{T_{\text{SF}}} \gg 1$, and when the angle with which the anode diverges from the thrust axis, α , is much less than 45° . In all other cases, the axial ion velocity will increase substantially due to the self-field thrust or the velocity will have a significant radial component. Our second assumption, that the flow is quasi-one dimensional, is inconsistent with the observation that the radial density distribution is approximately gaussian [63, 64], but because the mean density will decrease with increasing anode radius, this approximation should be correct to first order.

Our assumption of the plasma rotating rigidly only for a given axial position, rather than for the entire thruster volume as has been previously assumed, substantially reduces the predicted angular frequency for conical anodes. While plasma has

been observed to rotate rigidly [63], this observation has only been made for a fixed axial position, and it is nonphysical for the plasma to instantaneously acquire an azimuthal velocity upon injection. Because the plasma initially has no angular velocity and because there is no data with which to speculate about the rate of rotation as a function of axial position, we assume that the angular frequency, ω , increases linearly with z until the plasma flow separates from the anode.

While it has been demonstrated that thrust increases with increasing anode radius, this scaling cannot hold for all cases. For example, if a conical anode extends to a large exit plane radius, the density at the outermost edge of the anode face will be insufficient to carry a substantial current, and further extension of the anode would not increase thrust. Because we have already shown that the effective anode radius is a function of the internal radial forces, we anticipate that even in less-extreme cases there exists some radius at which the plasma density has been substantially reduced. Our penultimate assumption, that the flow has separated from the anode wall, approximates this condition of reduced plasma density. We assume that this reduction in density increases the resistance of the plasma so that the current density to the anode downstream of the separation point is negligible.

Our final assumption, that the magnetic field is axial and constant in magnitude within the anode, allows us to reach an analytical expression for our radial force balance without invoking elliptic integrals. The axial component of the magnetic field is typically much greater than the radial component within the anode volume. However, for thrusters with diverging magnetic fields, the magnetic field typically reduces from its maximum value by at least a factor of 2 along the anode length. We therefore expect that we will be able to predict thrust scaling for a given magnetic field configuration, but that the magnitude of the measured value may vary for thrusters with different applied-field topologies.

4.1.2 Thrust

Fradkin et al. relate the power, P_θ , due to the applied azimuthal force, F_θ , to the power of the rotating plasma column. At the point of flow separation from the anode, this relation is given by

$$P_\theta = \frac{d}{dt} \left(\frac{1}{2} I \omega^2 \right) \Big|_{z=z_{\text{sep}}} = \frac{F_\theta^2}{2\dot{m}}, \quad (4.1)$$

where I is the moment of inertia of the rotating plasma column and z_{sep} is the distance from the anode throat at which the plasma flow separates from the anode. If I , ω , and \dot{m} are known, we can solve for F_θ . Then, assuming that the conversion of azimuthal kinetic energy to directed kinetic energy occurs with efficiency η_θ , we can express the applied-field thrust component resulting from the swirling plasma as

$$T_{\text{SW}} = \sqrt{\eta_\theta} F_\theta. \quad (4.2)$$

η_θ is the product of two different efficiencies: the efficiency with which plasma is redirected to be parallel to the field lines and the divergence efficiency. The first of these efficiencies should be approximately constant since many thrusters share similar plasma parameters ($T_e \approx 2$ eV [44, 45, 17, 33, 19], $n_e \approx 10^{19}$ m³ [19, 33, 22], fully ionized [22]). The divergence efficiency was shown by Little and Choueiri [65] to be primarily dependent on electron temperature and the ratio of the solenoid radius to the anode radius, the latter of which has been shown to be similar for most AF-MPDTs [20]. For typical AF-MPDTs, the divergence efficiency modeled by Little and Choueiri is in the range of 0.7 to 0.8. However, their analysis does not include the effects of a bulk rotation of the plasma.

While we expect T_{SW} to be the dominant term in an expression for the applied-field thrust, we must also consider the thrust contribution due to the electromagnetic pinching forces, $T_{\text{AF-pinch}}$, resulting from the application of an external magnetic

field. Inward radial forces can increase thrust by increasing gasdynamic pressure on the tip of the cathode. Choueiri [18] observed the influence of self-induced pinching forces on thrust for SF-MPD thrusters, with operation at low current resulting in a substantial thrust component generated by the pinching components of the Lorentz force densities. Additionally, Tahara et al. [28] observed that increasing the centrifugal force in an AF-MPD thruster served to reduce the gasdynamic pressure at the cathode tip, and attributed this decrease in pressure to a decrease in measured thrust.

The applied-field thrust can therefore be expressed as

$$T_{\text{AF}} = T_{\text{SW}} + T_{\text{AF-pinch}}. \quad (4.3)$$

We define $T_{\text{AF-pinch}}$ as the difference in force on the tip of the cathode operating with an applied-field compared to without one. Therefore, in the case of a quasi-one-dimensional flow, we assume that $T_{\text{AF-pinch}} = 0$, since the pressure at the tip of the cathode is the same as that predicted when there is no radial Lorentz force. $T_{\text{AF-pinch}}$ can be negative in cases where the density is higher near the anode wall than at the tip of the cathode.

4.1.3 Moment of inertia

We now solve for P_θ using the assumptions given in Sec. 4.1.1. Assuming steady-state operation, the time derivative of the middle expression in Eq. 4.1 is

$$\frac{d}{dt} \left(\frac{1}{2} I \omega^2 \right) = \frac{1}{2} \left(\frac{\partial}{\partial t} (I \omega^2) + \nabla \cdot (I \omega^2) \right) \quad (4.4)$$

$$= \frac{1}{2} \mathbf{u} \cdot \nabla (I \omega^2) \quad (4.5)$$

$$= \frac{1}{2} a_0 \frac{\partial}{\partial z} (I \omega^2) \quad (4.6)$$

$$= \frac{1}{2} a_0 \left(\omega^2 \frac{\partial I}{\partial z} + I \frac{\partial}{\partial z} (\omega^2) \right). \quad (4.7)$$

The moment of inertia is defined by

$$I = m \langle r^2 \rangle, \quad (4.8)$$

where m is the total mass of the rotating body, and $\langle r^2 \rangle$ is the expected value for r^2 .

The mass is constant in z , and is given by

$$m = \frac{\dot{m} z_{\text{sep}}}{a_0}. \quad (4.9)$$

The expected value for r^2 is found by the integral fraction

$$\langle r^2 \rangle = \frac{\iiint_V \rho r^2 dV}{\iiint_V \rho dV}, \quad (4.10)$$

where ρ is the mass density. The mass density varies as a function of the anode radius at a given axial location, so that

$$\rho = \frac{\dot{m}}{a_0 \pi r_a(z)^2}. \quad (4.11)$$

A schematic of the relevant geometry is given in Fig. 4.1. The anode radius varies as a function of z by the relation

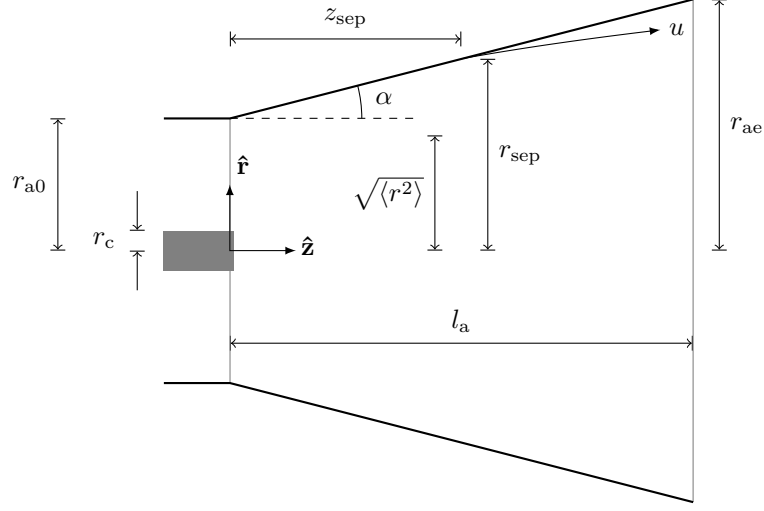


Figure 4.1: Schematic of the geometry relevant to the separation of the plasma flow from the anode wall.

$$r_a(z) = z \tan(\alpha) + r_{a0}. \quad (4.12)$$

Incorporating Eqs. 4.11 and 4.12 into Eq. 4.10 yields

$$\langle r^2 \rangle = \frac{3r_{a0}^2 + z^2 \tan^2(\alpha) + 3r_{a0}z \tan(\alpha)}{6}. \quad (4.13)$$

At the point of separation, this expression simplifies to

$$\langle r^2 \rangle = \frac{r_{sep}^2 + r_{sep}r_{a0} + r_{a0}^2}{6}. \quad (4.14)$$

Since

$$\frac{\partial \langle r^2 \rangle}{\partial z} = \frac{(2r_{sep} + r_{a0}) \tan(\alpha)}{6}, \quad (4.15)$$

we can now further simplify Eq. 4.7 to find that

$$\frac{d}{dt} \left(\frac{1}{2} I \omega^2 \right) = \frac{\dot{m} \omega^2}{12} (4r_{sep}^2 + r_{sep}r_{a0} + r_{a0}^2), \quad (4.16)$$

where we have incorporated our assumption that the angular frequency increases linearly from the anode throat to the position where separation occurs. The thrust due to the swirling motion of the plasma can now be expressed as

$$T_{\text{SW}} = \sqrt{\eta_\theta} \dot{m} \omega \sqrt{\frac{4r_{\text{sep}}^2 + r_{\text{sep}} r_{\text{a0}} + r_{\text{a0}}^2}{12}}. \quad (4.17)$$

4.1.4 Angular frequency

The angular frequency relates to the torque, τ_z , on the plasma column by the expression

$$\tau_z = \frac{d}{dt} (I\omega) \quad (4.18)$$

$$= \mathbf{u} \cdot \nabla (I\omega) \quad (4.19)$$

$$= a_0 \left(\omega \frac{\partial I}{\partial z} + I \frac{\partial \omega}{\partial z} \right) \quad (4.20)$$

$$= \dot{m} \omega \left(z \frac{\partial \langle r^2 \rangle}{\partial z} + \langle r^2 \rangle \right) \quad (4.21)$$

$$= \frac{\dot{m} \omega r_{\text{sep}}^2}{2}. \quad (4.22)$$

In order to determine ω , we will now solve for the torque on the plasma resulting from the current and applied magnetic field. The general expression for the torque inside the anode of volume V , is

$$\tau = \iiint_V \mathbf{r} \times \frac{\partial \mathbf{F}}{\partial V} dV, \quad (4.23)$$

where

$$\frac{\partial \mathbf{F}}{\partial V} = \mathbf{j} \times \mathbf{B}. \quad (4.24)$$

since only the Lorentz force resulting from the current density, \mathbf{j} , and magnetic field acts to swirl the plasma. We do not know the current density distribution, nor do we know the limits of the relevant volume, but we can limit the assumptions necessary about the current distribution with the concept of the magnetic stress tensor, \mathbf{B} . This tensor is defined [40] by the relation

$$\nabla \cdot \mathbf{B} = \mathbf{j} \times \mathbf{B}, \quad (4.25)$$

in order to determine the force density as a function of a surface integral by use of the divergence theorem:

$$\iiint_V \nabla \cdot \mathbf{B} dV = \iint_S \mathbf{B} \cdot \hat{\mathbf{n}} dS, \quad (4.26)$$

where S is the surface inclosing the volume, V . The torque is found using the azimuthal component of this force:

$$\tau_z = \iint_S r (\mathbf{B} \cdot \hat{\mathbf{n}})_\theta dS. \quad (4.27)$$

The magnetic stress tensor takes the form

$$\mathbf{B} = \frac{1}{\mu_0} \begin{bmatrix} B_r^2 - \frac{1}{2}B^2 & B_r B_\theta & B_r B_z \\ B_\theta B_r & B_\theta^2 - \frac{1}{2}B^2 & B_\theta B_z \\ B_\theta B_z & B_z B_\theta & B_z^2 - \frac{1}{2}B^2 \end{bmatrix}. \quad (4.28)$$

The only surfaces on which an azimuthal shear force exists are those enclosing a current since $(\mathbf{B} \cdot \hat{\mathbf{n}})_\theta$ is only nonzero when there is a self-induced magnetic field. On the backplate of the thruster and tip of the cathode, the unit normal vector is $(0, 0, 1)$. The torque on the backplate is

$$\tau_{z,\text{bp}} = \frac{1}{\mu_0} \iint_{\text{bp}} r^2 B_\theta B_z dr d\theta. \quad (4.29)$$

For a typical applied-field thruster, $B_z = B_A$ at the backplate. B_θ can be evaluated using Ampère's law, where the enclosed current between the electrodes is the total current:

$$B_{\theta,\text{bp}} = \frac{\mu_0 J}{2\pi r}. \quad (4.30)$$

Evaluating the integral in Eq. 4.29 yields

$$\tau_{z,\text{bp}} = \frac{1}{2} J B_A (r_{a0}^2 - r_c^2), \quad (4.31)$$

This torque is the same as that typically considered for a cylindrical anode [8]. However, for both cylindrical and conical anodes, we must also consider the shear over the tip of the cathode. This shear depends on how far the cathode extends into the anode volume. For a cathode that ends at the anode throat, we assume the current density at the tip to be constant, so that

$$B_{\theta,c} = \frac{\mu_0 J r}{2\pi r_c^2}, \quad (4.32)$$

and the total torque at the tip of the cathode is

$$\tau_{z,c} = \frac{1}{4} J B_A r_c^2. \quad (4.33)$$

The unit normal vector for the wall of the anode is

$$\hat{\mathbf{n}} = \left(\cos(\alpha), 0, \sin(\alpha) \right). \quad (4.34)$$

The enclosed current is the total current at the upstream end of this surface and 0 at the downstream end. We assume that the radial current density is uniform in z , so that the azimuthal magnetic field is

$$B_{\theta,\text{aw}} = \frac{\mu_0 J (z_{\text{sep}} - z)}{2\pi r_a z_{\text{sep}}}, \quad (4.35)$$

The torque at the anode wall is

$$\tau_{z,\text{aw}} = \frac{1}{\mu_0} \iint_{\text{aw}} r_a^2 B_{\theta,\text{aw}} \left(B_r \cos(\alpha) + B_z \sin(\alpha) \right) dz d\theta. \quad (4.36)$$

Although the azimuthal currents in the plasma contribute to both B_r and B_z , to first order these magnetic field components are those generated by the solenoid, and can be calculated using the Biot-Savart law for a solenoid [35]. However, for simplicity we assume that $B_z \gg B_r$, and that the applied field strength is approximately constant through the anode volume. We note that while these assumptions makes the problem significantly easier to solve, many thrusters have applied fields that decrease in strength over the length of the anode, with exit plane applied-field magnitudes being less than half the magnitude at the anode throat. We therefore expect our model to overpredict thrust in these cases, especially for anodes with large α values.

Incorporating our assumptions about the magnetic field into Eq. 4.36 yields

$$\tau_{z,\text{aw}} = \frac{JB_A \cos(\alpha)}{6} \left(r_{\text{sep}}^2 + r_{\text{sep}} r_{a0} - 2r_{a0}^2 \right). \quad (4.37)$$

We can now rearrange Eq. 4.22 to determine the angular frequency:

$$\omega = \frac{2(\tau_{z,\text{bp}} + \tau_{z,\text{c}} + \tau_{z,\text{aw}})}{\dot{m}r_{\text{sep}}^2} \quad (4.38)$$

$$= \frac{JB_A \left[2r_{\text{sep}}^2 \cos(\alpha) + 2r_{\text{sep}} r_{a0} \cos(\alpha) + (6 - 4 \cos(\alpha)) r_{a0}^2 - 3r_c^2 \right]}{6\dot{m}r_{\text{sep}}^2}. \quad (4.39)$$

For convenience, we introduce the nondimensional geometric term

$$\bar{r}_\omega = \frac{2r_{\text{sep}}^2 \cos(\alpha) + 2r_{\text{sep}} r_{\text{a0}} \cos(\alpha) + (6 - 4 \cos(\alpha)) r_{\text{a0}}^2 - 3r_c^2}{6r_{\text{sep}}^2}, \quad (4.40)$$

and simplify Eq. 4.39 so that

$$\omega = \frac{JB_A}{\dot{m}} \bar{r}_\omega (r_{\text{sep}}, r_c, r_{\text{a0}}, \alpha). \quad (4.41)$$

Equation 4.41 is consistent with observations of ω being proportionate to JB_A/\dot{m} [63]. Combining Eq. 4.41 with Eq. 4.17 yields

$$T_{\text{SW}} = \sqrt{\eta_\theta} JB_A \bar{r}_\omega (r_{\text{sep}}, r_c, r_{\text{a0}}, \alpha) \sqrt{\frac{4r_{\text{sep}}^2 + r_{\text{sep}} r_{\text{a0}} + r_{\text{a0}}^2}{12}}. \quad (4.42)$$

With an expression for r_{sep} , we will be equipped to determine the swirl component of the thrust in terms of controllable parameters.

4.2 Radius of flow separation from the anode

We now seek an analytical expression for r_{sep} . For a fluid with velocity \mathbf{u} expanding through a physical nozzle, which diverges at angle α from the thrust axis (Fig. 4.1), the fluid separates from the nozzle when

$$\tan(\alpha) > \frac{u_r}{u_z}. \quad (4.43)$$

In order to determine the axial position, z_{sep} , and corresponding radius, r_{sep} , at which this separation occurs, we consider the radial momentum balance for a steady-state, azimuthally symmetric inviscid flow:

$$\rho \left(u_r \frac{\partial u_r}{\partial r} + u_z \frac{\partial u_r}{\partial z} - \frac{u_\theta^2}{r} \right) = -\frac{\partial p_{\text{GD}}}{\partial r} + j_\theta B_z - j_z B_\theta, \quad (4.44)$$

where p_{GD} is the gasdynamic pressure. At the anode wall, $\frac{u_r}{u_z} = \frac{\partial r}{\partial z} = \tan(\alpha)$. We can therefore simplify Eq. 4.44 so that

$$\rho \left(2u_z \tan^2(\alpha) \frac{\partial u_z}{\partial r} - \omega^2 r_a \right) = -\frac{\partial p_{\text{GD}}}{\partial r} + j_\theta B_z - j_z B_\theta, \quad (4.45)$$

where we have also replaced u_θ/r with ω . We will now derive an expression for each term in Eq. 4.45 so that we may determine the value of $r = r_{\text{sep}}$ at which the equality holds.

4.2.1 Convective terms

We continue our assumption that u_z is the sound speed, which is given by

$$a_0 = \sqrt{\frac{\gamma k_B T_i}{M_i}}. \quad (4.46)$$

For all calculations, we assume that $T_i = 2$ eV, which is on the order of the measurement reported for a wide range of operating conditions [44, 45, 17, 33, 19].

Although we assume the variation of the axial velocity with radial position to be small, the fluid must flow parallel to the anode at the anode wall and is strictly axial along the thrust axis. Since we have assumed that the conversion of azimuthal flow to axial flow takes place downstream of the separation point, the axial velocity must have a dependence on r for energy to be conserved. We therefore assume that for a given z , $\sqrt{u_z^2 + u_r^2}$ is constant, and that the direction of flow at (r, z) can be traced from the vertex of the anode cone (illustrated in Fig. 4.2). The two velocity components are then given by

$$u_r = \frac{a_0 r}{\sqrt{r^2 + \left(z + \frac{r_{a0}}{\tan(\alpha)}\right)^2}}. \quad (4.47)$$

and

$$u_z = \frac{a_0}{\sqrt{1 + \left(\frac{r \tan(\alpha)}{z \tan(\alpha) + r_{a0}}\right)^2}} \quad (4.48)$$

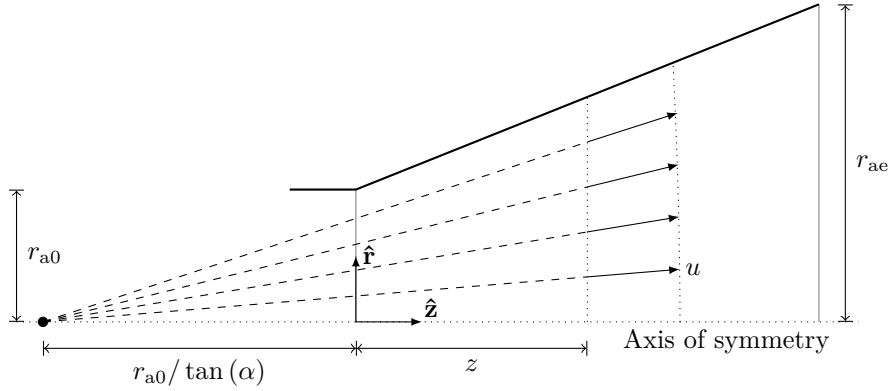


Figure 4.2: Illustration of assumed velocity distribution at \$z\$ (\$|u| = a_0\$).

The derivative of the latter velocity is given by

$$\frac{\partial u_z}{\partial r} = \frac{a_0 \left(\frac{\tan(\alpha)}{z \tan(\alpha) + r_{a0}} \right)^2 r}{\left(1 + \left(\frac{r \tan(\alpha)}{z \tan(\alpha) + r_{a0}} \right)^2 \right)^{3/2}}, \quad (4.49)$$

and simplifies at the anode wall to

$$\left. \frac{\partial u_z}{\partial r} \right|_{r=r_a} = \frac{-a_0 \sin^2(\alpha) \cos(\alpha)}{r_a}. \quad (4.50)$$

At the anode wall, the left-hand side of Eq. 4.45 can be rewritten as

$$\rho \left(2u_z \tan^2(\alpha) \frac{\partial u_z}{\partial r} - \omega^2 r_a \right) = \frac{-2\dot{m}a_0 \sin^3(\alpha) \tan(\alpha)}{\pi r_a^3} - \frac{J^2 B_A^2 \bar{r}_\omega^2 (r_{sep}, r_c, r_{a0}, \alpha)}{\pi \dot{m}a_0 r_a}, \quad (4.51)$$

where the final term represents the centrifugal force density, \$f_{cent}\$.

4.2.2 Gasdynamic pressure gradient

There are two components to the gasdynamic pressure gradient we must consider. First, there is a radially inward force density resulting from our imposed flow conditions (Fig. 4.2). However, for the equality in Eq. 4.45 to hold, we must also account for the pressure gradient resulting from the existence of the anode wall. In cases where the modeled outward force density is greater than the inward force density, the physical barrier at the anode wall results in an opposing force density in the form of a pressure gradient. We will refer to the two components as $\partial p_{\text{flow}}/\partial r$ and $\partial p_{\Sigma f}/\partial r$ respectively.

The gasdynamic pressure is given by the ideal gas equation for ions:

$$p_{\text{GD}} = \frac{\rho k_B T_i}{M_i}. \quad (4.52)$$

The radial component of the gradient is

$$\frac{\partial p_{\text{GD}}}{\partial r} = \frac{k_B T_i}{M_i} \frac{\partial \rho}{\partial r}. \quad (4.53)$$

Although we assume the density to be approximately constant in r for a given z , we can use our derivative of the axial velocity with respect to r to find that

$$\frac{\partial p_{\text{flow}}}{\partial r} = \frac{\partial p_{\text{GD}}}{\partial \rho} \frac{\partial \rho}{\partial u_z} \frac{\partial u_z}{\partial r} \quad (4.54)$$

$$= \frac{-\dot{m} k_B T_i}{M_i \pi r_a^2 u_z^2} \frac{\partial u_z}{\partial r} \quad (4.55)$$

$$= \frac{-p_{\text{GD}}}{u_z} \frac{\partial u_z}{\partial r}. \quad (4.56)$$

At the anode wall, this pressure gradient can now be rewritten as

$$\frac{p_{\text{flow}}}{\partial r} = \frac{\dot{m}a_0 \sin^2(\alpha)}{\gamma\pi r_a^3}. \quad (4.57)$$

When the density is not approximately constant in r , our model is insufficient, however we assume that

$$\frac{\partial p_{\Sigma f}}{\partial r} \propto \frac{p_{\text{GD}}}{r}. \quad (4.58)$$

At the anode wall, this expression yields

$$\frac{\partial p_{\Sigma f}}{\partial r} \propto \frac{\dot{m}a_0}{\gamma\pi r_a^3}. \quad (4.59)$$

4.2.3 Lorentz force density

We derive the axial and azimuthal currents from Ohm's law, which states that

$$\mathbf{j} = \sigma \left[\mathbf{E} + \mathbf{u} \times \mathbf{B} + \frac{\nabla p_{\text{GD}} - \mathbf{j} \times \mathbf{B}}{n_e e} \right], \quad (4.60)$$

where E is the electric field strength and σ is the plasma conductivity. The conductivity is given by

$$\sigma = \frac{n_e e^2}{m_e \nu_{ei}}, \quad (4.61)$$

where m_e is the electron mass. The azimuthal current is then

$$j_\theta = \sigma \left[-u_r B_z + \frac{j_r B_z}{n_e e} \right], \quad (4.62)$$

since the electric field is negligible in the azimuthal direction, the pressure is uniform in the azimuthal direction, and since we have assumed the applied field to be strictly axial. Applying the previous assumption that the current density is uniform in z , and assuming that the current leaving the anode wall is primarily radial, we find that

$$j_r = \frac{-J}{2\pi r_a z_{\text{sep}}}. \quad (4.63)$$

Although $j_z B_\theta = 0$ beyond the point of separation since there is no longer an enclosed current (and therefore $B_\theta = 0$), we will determine j_z so that we can compare the radial forces upstream of the separation point. The axial current density is

$$j_z = \sigma \left[u_r B_\theta + \frac{(\partial p_{\text{GD}} / \partial z) - j_r B_\theta}{n_e e} \right]. \quad (4.64)$$

Since the axial velocity depends only weakly on z , the axial pressure gradient at the wall is given by

$$\frac{\partial p_{\text{GD}}}{\partial z} = \frac{\partial}{\partial z} \left(\frac{\dot{m} k_B T_i}{M_i u_z \pi (z \tan(\alpha) + r_{a0})^2} \right) \quad (4.65)$$

$$= \frac{-2p_{\text{GD}} \sin(\alpha)}{r_a \cos^2(\alpha)}. \quad (4.66)$$

Accounting for the self-induced magnetic field being in the $-\hat{\theta}$ direction, the Lorentz force density at the anode wall can now be expressed as

$$\begin{aligned} j_\theta B_z - j_z B_\theta &= \frac{-eB_A^2 \sin(\alpha)}{\pi r_a m_e \nu_{ei}} \left[\frac{J}{2(r_{\text{sep}} - r_{a0}) \cos(\alpha)} + \frac{e\dot{m}}{M_i r_a} \right] \\ &\quad - \frac{e\mu_0 J (r_{\text{sep}} - r_a) \sin(\alpha)}{\pi^2 r_a^3 m_e \nu_{ei} (r_{\text{sep}} - r_{a0})} \left[\frac{\mu_0 J (r_{\text{sep}} - r_a)}{4\pi (r_{\text{sep}} - r_{a0})} \left(\frac{J}{2(r_{\text{sep}} - r_{a0}) \cos(\alpha)} + \frac{e\dot{m}}{M_i r_a} \right) \right. \\ &\quad \left. + \frac{\dot{m} a_0}{\gamma^2 r_a \cos^2(\alpha)} \right], \end{aligned} \quad (4.67)$$

where the two terms represent the Hall and self-induced force densities (f_H and f_{SF} respectively).

4.2.4 Comparison of radial forces

In order to simplify our momentum balance, we will compare the magnitude of each radial force density under typical operating conditions. For now, we will ignore the contributions of $\partial p_{\Sigma f} / \partial r$ since the magnitude of this contribution is unknown.

Outward forces

The only outward force densities are from the convective terms in our momentum balance. In Fig. 4.3, we compare the radial force densities at the anode wall as a function of axial position using typical operating conditions for one of our laboratory thrusters, the lithium Lorentz force accelerator (LiLFA), which is described in Appendix C. We see that the centrifugal force is dominant compared to the other convective terms (shown by $f_{\text{out}} - f_{\text{cent}}$), and so we can typically make the assumption that the outward force density can be assumed to be

$$f_{\text{out}} = \frac{J^2 B_A^2 \bar{r}_\omega^2 (r_{\text{sep}}, r_c, r_{a0}, \alpha)}{\pi \dot{m} a_0 r_a}. \quad (4.68)$$

It has been suggested that viscous forces might limit the rate of rotation [12]. In order to determine if viscous forces might have a significant influence on the modeled centrifugal force density, we calculate the Reynolds number at the anode exit plane,

$$\text{Re} = \frac{\rho \omega 2\pi r_{ae}^2}{\mu}, \quad (4.69)$$

where μ is the viscosity [32],

$$\mu = \frac{3n_i k_B T_i \nu_i}{10 (eB_A/M_i)^2}, \quad (4.70)$$

and where ν_i is the ion collision frequency, given by

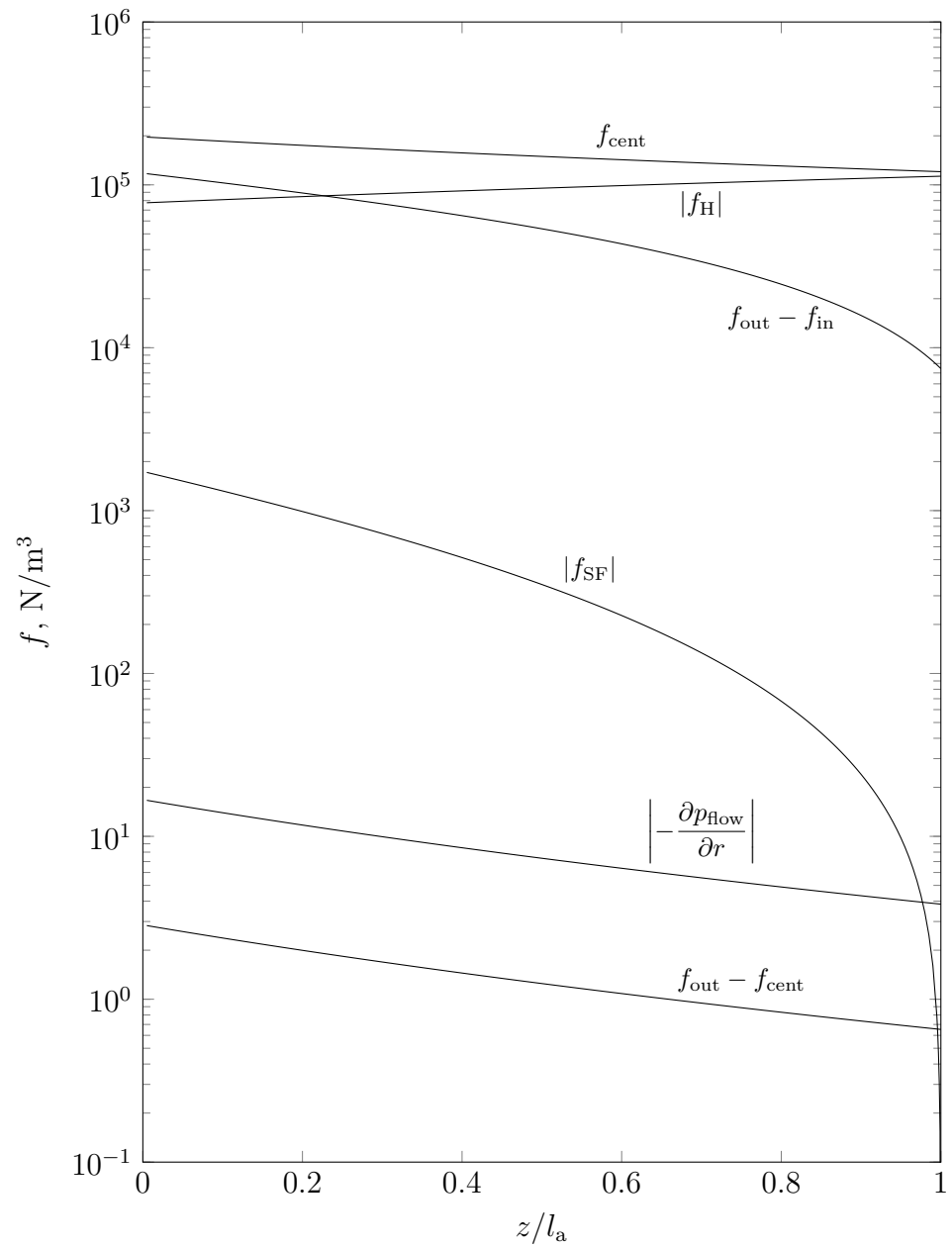


Figure 4.3: Radial force densities at the anode wall as a function of axial position for the LiLFA operating at 800 A, 0.056 T, and 8 mg/s lithium mass flow rate.

$$\nu_i = \frac{e^4 n_i \ln \left(1.24 \times 10^7 \sqrt{T_e^3 / n_e} \right)}{12\pi^{3/2} \epsilon_0^2 \sqrt{M_i} (k_B T_i)^{3/2}}. \quad (4.71)$$

We find that $\text{Re} > 10^8$ for typical operating conditions for the LiLFA, indicating that the inertial forces are substantially larger than the viscous forces. In addition, the shear due to viscosity is typically insignificant compared to the shear previously described due to the Lorentz force. This observation justifies our use of an inviscid flow model for the case of the LiLFA, however, for thrusters operating with high mass flow rates and low applied-field strengths, the shear due to viscosity can be significant.

Inward forces

As is shown in Fig. 4.3, $\partial p_{\text{flow}} / \partial r$ is typically insignificant compared to the pinching components of the Lorentz force densities. Since $\frac{\mu_0 J}{2\pi r_a}$ is typically much less than B_A , the pinching components due to the self-induced magnetic field are small compared to those resulting from Hall currents interacting with the applied-field. However, the self-induced pinching component can still be substantial for thrusters with large α values due to the correspondingly large axial pressure gradient.

In most cases, our dominant inward force density is f_H . This force density is composed of two components: the force related to the axial current, j_r , and the force related to the axial ion velocity, u_r . In Fig. 4.4, we show that the force density resulting from the axial current is typically dominant within the anode volume, and so the inward force density is given by

$$f_{\text{in}} = \frac{JB_A^2 e \tan(\alpha)}{2\pi m_e \nu_{ei} r_a (r_{\text{sep}} - r_{a0})}. \quad (4.72)$$

Nondimensional parameter

Even using our approximate values for the inward and outward forces, there is no analytical expression for r_{sep} . The value can be found numerically, however for nearly

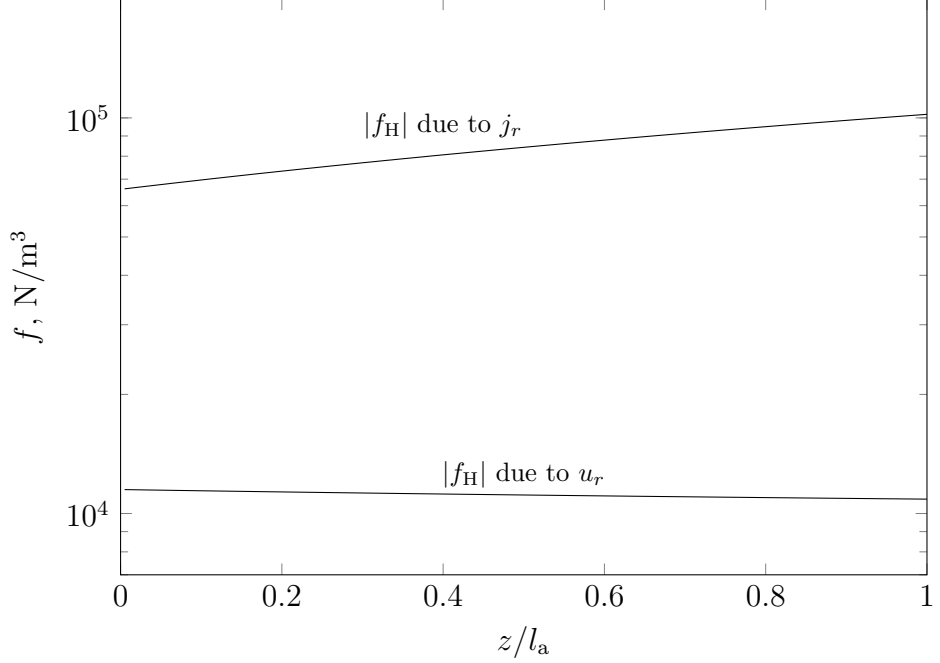


Figure 4.4: Radial Hall force component densities at the anode wall as a function of axial position for the LiLFA operating at 800 A, 0.056 T, and 8 mg/s lithium mass flow rate.

all data in the literature, it can be shown that either $r_{\text{sep}} = r_{\text{a0}}$, or $r_{\text{sep}} = r_{\text{ae}}$.

We can determine which, if either, of these cases applies using the nondimensional confinement parameter

$$\bar{f} = \frac{f_{\text{in}}}{f_{\text{out}}} = \frac{e\dot{m}a_0 \tan(\alpha)}{2J\bar{r}_\omega^2(r_{\text{sep}}, r_c, r_{\text{a0}}, \alpha) m_e \nu_{\text{ei}} (r_{\text{sep}} - r_{\text{a0}})}. \quad (4.73)$$

If $\bar{f} \leq 1$ at the anode exit plane, $r_{\text{sep}} = r_{\text{ae}}$ (the plasma exerts an outward force on the anode wall at the exit plane). Conversely, if $\bar{f} \geq 1$ at the anode throat, the inward radial forces at the anode throat are large enough to immediately cause separation to occur, and $r_{\text{sep}} = r_{\text{a0}}$. We will refer to these two distinct modes of operation as the anode-confinement mode, and the magnetic-confinement mode, respectively. In summary,

$$r_{\text{sep}} = \begin{cases} r_{\text{ae}} & \text{if } \bar{f}\Big|_{r_{\text{sep}}=r_{\text{ae}}} < 1 \\ r_{\text{a0}} & \text{if } \bar{f}\Big|_{r_{\text{sep}}=r_{\text{a0}}} > 1 \\ \text{solution of } \bar{f} = 1 \text{ for } r_{\text{sep}} & \text{otherwise.} \end{cases} \quad (4.74)$$

4.3 Applied-field thrust due to pinching forces

We have assumed until now that the flow is quasi-one-dimensional. We will now examine the consequences on our thrust model if this assumption is incorrect.

4.3.1 Effect of radial forces on pinching thrust component

We can use our confinement parameter \bar{f} to qualitatively describe the state of the flow. If $\bar{f} \approx 1$, the flow is approximately one dimensional. However, if $\bar{f} < 1$, there is an outward radial force that will increase the mass density at the anode wall and decrease the density at the thrust axis. Conversely, if $\bar{f} > 1$, the opposite will be true. Therefore, the radial mass distribution can be assumed to be a function of \bar{f} .

The parameter \bar{f} describes the radial force balance in cases where $\bar{f} \gtrsim 0.5$, but for smaller values, where the outward radial force is much larger than the modeled inward radial force, the dominant inward force density term is the pressure gradient at the anode wall, $\partial p_{\Sigma f}/\partial r$. The ratio of $\partial p_{\Sigma f}/\partial r$ to the centrifugal force density gives us a second confinement parameter,

$$\bar{f}_p = \frac{\partial p_{\Sigma f}/\partial r}{f_{\text{cent}}} = \frac{\dot{m}^2 a_0^2}{J^2 B_A^2 r_a^2 \bar{r}_\omega^2(r_{\text{sep}}, r_c, r_{\text{a0}}, \alpha) \gamma}. \quad (4.75)$$

Because these two confinement parameters, \bar{f} and \bar{f}_p , describe the radial force balance across a wide range of operating conditions, we assume that, for a given thruster geometry, $T_{\text{AF-pinch}}$ is a function of \bar{f} and \bar{f}_p and that $T_{\text{AF-pinch}}$ increases

monotonically with each. $T_{\text{AF-pinch}}$ is negative when $\bar{f} < 1$, 0 when $\bar{f} = 1$, and positive when $\bar{f} > 1$.

4.3.2 Effect of radial forces on swirl thrust component

We have already shown that radial forces play a role in determining the radius of separation, however the effect of these forces on the mass distribution can also affect the swirl component of the thrust. Increasing \bar{f} will serve to decrease $\langle r^2 \rangle$, which is an important parameter in our calculations of both the moment of inertia and the angular velocity. Because the swirl component of the thrust depends on each of these parameters, we will now derive an approximate scaling of this thrust component with $\langle r^2 \rangle$.

From Eqs. 4.1 and 4.2,

$$T_{\text{SW}}^2 \propto \frac{d}{dt} (I\omega^2) \Big|_{z=z_{\text{sep}}} . \quad (4.76)$$

Assuming that the angular velocity and mass distribution are at steady-state, and that only the mass of the rotating body changes as a function of time,

$$T_{\text{SW}}^2 \propto \dot{m} \langle r^2 \rangle \omega^2 . \quad (4.77)$$

Applying the same assumption to Eq. 4.18, we find that

$$\omega = \frac{\tau_z}{\dot{m} \langle r^2 \rangle} . \quad (4.78)$$

The result is that

$$T_{\text{SW}} \propto \frac{\tau_z}{\sqrt{\langle r^2 \rangle}} . \quad (4.79)$$

Equation 4.79 is a function of two length scales: the distance from the thrust axis at which the torque is applied, and the expected value for r^2 . If we assume that the former is independent of the mass distribution for $r_{\text{sep}} = r_{\text{ae}}$ (meaning $\bar{f} \leq 1$), then the swirl component of the thrust scales with $\langle r^2 \rangle^{-1/2}$. A higher dimensional model than that presented here is necessary to determine $\langle r^2 \rangle$, however we can predict from Eq. 4.79 that when $\bar{f} \leq 1$ at the anode exit plane, increasing \bar{f} or \bar{f}_p will serve to increase the thrust even when no change is predicted by Eq. 4.17. When $\bar{f} > 1$, the separation of the plasma from the anode wall will reduce the radius at which the torque is applied along with the expected value for r^2 , and we can only predict that the dependence of the swirl component of thrust on \bar{f} will be less pronounced compared to the case when $\bar{f} \leq 1$.

In Chapter 5, we will examine how thrust scales with both \bar{f} and \bar{f}_p for a number of different thrusters. In order to evaluate \bar{f} for cylindrical thrusters, for which there is a singularity, we use the relation

$$\frac{\tan(\alpha)}{r_{\text{sep}} - r_{\text{a0}}} = \frac{1}{l_a}. \quad (4.80)$$

4.4 Summary

We have derived a quasi-one-dimensional applied-field thrust model (Eq. 4.42). However, this model is only appropriate in the uncommon case that our confinement parameter $\bar{f} = 1$. In Ch. 5, we define a thrust coefficient, C_T , which is the ratio of measured thrust to modeled thrust. Based on our previous analysis of the role of radial forces in thrust generation, we can predict trends in how this thrust coefficient will scale with the confinement parameter.

When $\bar{f} < 1$, the outward radial forces exceed the inward radial forces, and the plasma is in the anode-confinement mode. In this mode, for a given thruster, we

expect the thrust coefficient to depend solely on the confinement parameter. Increasing the confinement parameter will decrease the plasma density near the anode wall and increase the density near the thrust axis, which will increase pressure on the tip of the cathode, and the rate of rotation of the plasma column. Both the increase in pressure, and the increase in azimuthal kinetic energy, will serve to increase the thrust parameter.

When $\bar{f} > 1$, the inward radial forces are dominant, and the plasma is in a magnetic-confinement mode. In this mode, the plasma is pinched inward from the anode wall, reducing the volume on which the Lorentz force acts to generate thrust. We therefore expect a reduced slope in C_T as a function of \bar{f} compared to operation in the anode-confinement mode.

Chapter 5

Verification with Reported⁴ Experimental Data

We will now examine how measured thrust reflects the predictions made in Chapter 4 using data from the literature. All measurements are of the total thrust. Because we wish to examine the scaling of the applied-field thrust component, we define the dimensionless thrust coefficient

$$C_T = \frac{T - T_{\text{SF}} - T_{\text{GD}}}{k_{\text{Tikhonov}} J B_{\text{A}} r_{\text{a}0}}. \quad (5.1)$$

Assuming that we know T_{SF} and T_{GD} , C_T is the applied-field thrust component nondimensionalized by the minimum prediction of Tikhonov et al. (evaluated at the anode throat). We again employ the Tikhonov et al. model because of how often it has been used in the literature. Because the geometry is constant for a single thruster, the Tikhonov et al. model serves as a stand-in for any $J B_{\text{A}} r$ thrust model, including our own model of the swirl component of the applied-field thrust, since these models only differ by a constant for a given geometry. We therefore expect that any observed trends in C_T can be attributed to a change in the swirl or the pinching component of

⁴This chapter is based on work being prepared to be submitted for publication.

the thrust compared to the prediction of a quasi-one-dimensional model. Based on our findings in Chapter 3, we set $k_{\text{Tikhonov}} = 0.14$.

We assume that the self-field thrust component is given by the Maecker formula (Eq. 2.13). The gasdynamic thrust component is given by Eq. 2.14. This latter thrust component includes two unknown parameters: the temperature of the plasma at the injection site, and the gasdynamic thrust coefficient, k_{GD} . We continue our assumption from previous chapters that $\mathcal{T}_i = 2 \text{ eV}$. We assume that $k_{\text{GD}} = 1$, but since values employed in the literature are as high as 1.6 [43], we demonstrate that this larger value does not significantly affect our results in Appendix D. For all results, we evaluate \bar{f} at $z = 0$. Table 5.1 compares the design features of each thruster referenced in this chapter.

5.1 Confinement modes

The only thruster for which measurements are taken in both anode-confinement and magnetic-confinement modes is the Alta 200 kW argon thruster [15, 66, 67, 68]. We show how the thrust coefficient scales with \bar{f} for these measurements in Fig. 5.1. We see two distinct regimes. When $\bar{f} < 1.3$, C_T increases as a function of \bar{f} . However, for $\bar{f} \geq 1.3$, C_T is either constant or decreasing. This transition is consistent with the prediction made in Ch. 4, that the slope of C_T is smaller when $\bar{f} > 1$ than when $\bar{f} < 1$. Since $\bar{f} = 1$ represents the condition where plasma flow separation from the anode has occurred, we expect that for $\bar{f} > 1$, increasing values of \bar{f} serve to reduce the effective anode radius, decreasing the torque on the plasma column, and therefore limiting the swirl thrust component. The fact that the change in behavior occurs at $\bar{f} = 1.3$ rather than 1 may be due to our assumption that $\mathcal{T}_i = 2 \text{ eV}$, whereas Albertoni et al. estimate the temperature for this thruster to be as high as 5 eV based

Table 5.1: Design features of each thruster referenced in this chapter.

Thruster	Propellant	Propellant injection site	r_{a0} , mm	r_{ae} , mm	α	Magnetic field profile within anode
ALFA 30 kW	Ar	Orificed hollow cathode	22	36	12°	Parallel
Alta 200 kW	Ar	Multichannel hollow cathode	50	66	20°	Diverging
H2-4F 12 kW	H ₂	Anode backplate	3.8	18	61°	Parallel
LeRC 100 kW	Ar	Anode backplate	25.4	25.4	0°	Parallel
MAI 30 kW	Li	Multichannel hollow cathode	22	36	12°	Diverging
MAI 150 kW	Li	Multichannel hollow cathode	48	80	15°	Diverging

on measurements from a similar thruster, the hybrid plasma thruster [15]. A value of $T_i = 3.4$ eV results in the transition occurring when $\bar{f} = 1$.

We observe that there is a substantial spread in the data for $\bar{f} > 1.3$ that depends on magnetic field strength and mass flow rate. While \bar{f} predicts where the transition from one mode to the next will occur, \bar{f} does not predict C_T scaling well for $\bar{f} > 1$. Because \bar{f} is the radial force balance evaluated at the anode wall, and we predict little or no plasma at the anode wall when $\bar{f} > 1$, it is not surprising that the confinement parameter does not predict thrust scaling in the magnetic-confinement mode.

We will see in Sec. 5.2 that in all cases where $\bar{f} < 1$, C_T increases with \bar{f} . However, the 12 kW H2-4F hydrogen thruster was operated exclusively in the magnetic-confinement mode, where $\bar{f} > 1$. The data for this thruster (Fig. 5.2) [57] show that C_T is decreasing, indicating that the pinching forces are reducing the angular frequency of the rotating body. We see that for these data, $C_T < 1.2$, suggesting that r_{a0} is approximately the correct r_a value to use when implementing the Tikhonov et al. thrust model. Since $r_{ae}/r_{a0} = 4.74$ for the H2-4F, r_a is particularly ambiguous, and the fact that $C_T = r_a/r_{a0} \approx 1$ provides further evidence that the volume of the plasma has been constricted by pinching forces.

5.2 Scaling of C_T with the confinement parameter

In Chapter 4, we predicted that the thrust coefficient would increase with \bar{f} when $\bar{f} < 1$ as a result of increasing pressure on the tip of the cathode and increasing azimuthal kinetic energy within the anode. However, we said that \bar{f}_p is the more relevant parameter with $\bar{f} \lesssim 0.5$ because the pressure gradient contribution from the anode wall is dominant in this regime. In Figs. 5.3 (a) and (b), we show how C_T scales with each parameter for the MAI 30 kW lithium thruster [25, 69, 70]. We see qualitatively that \bar{f}_p is the more relevant scaling parameter. While C_T increases with

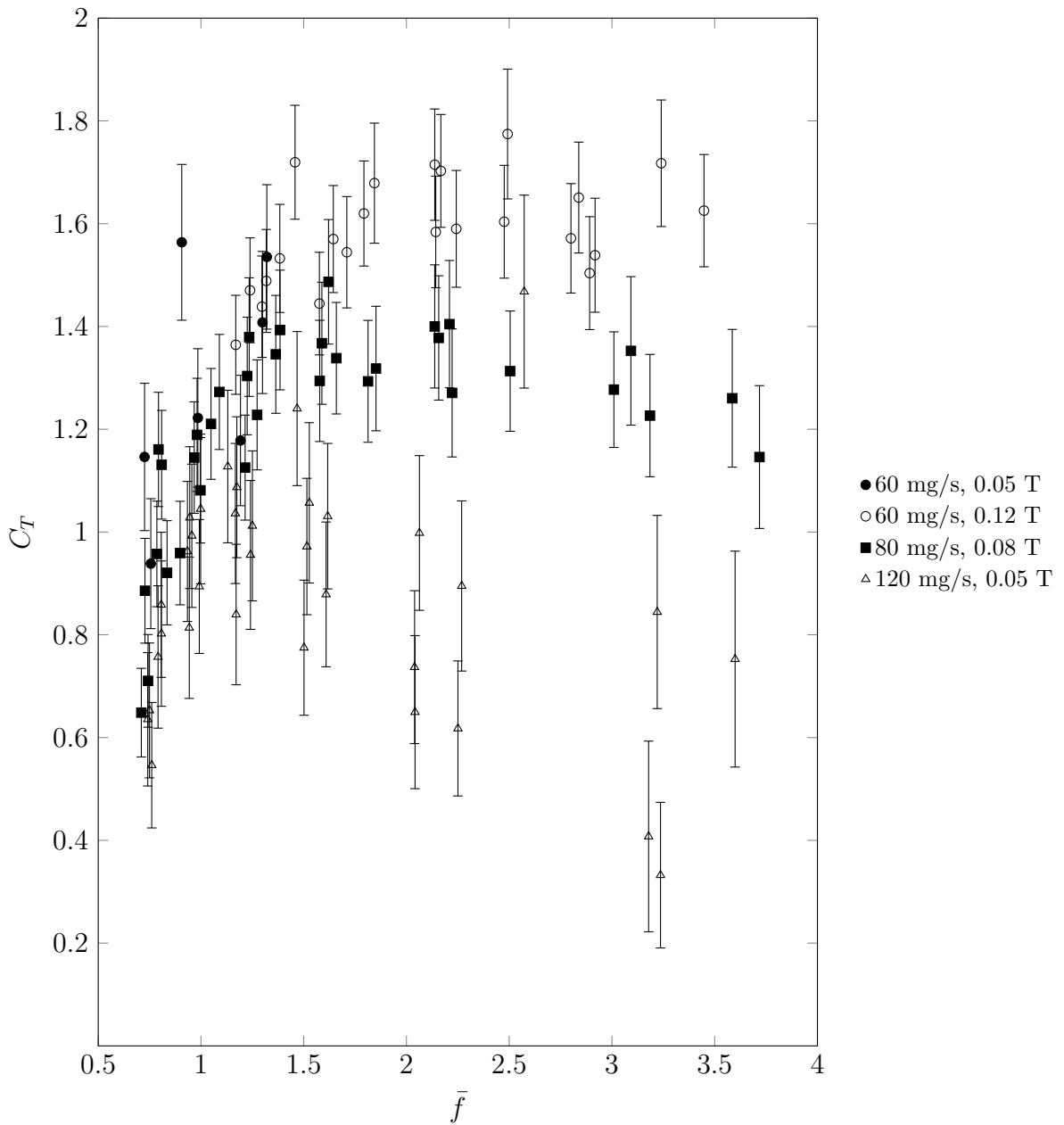


Figure 5.1: C_T as a function of \bar{f} for the 200 kW Alta argon thruster.

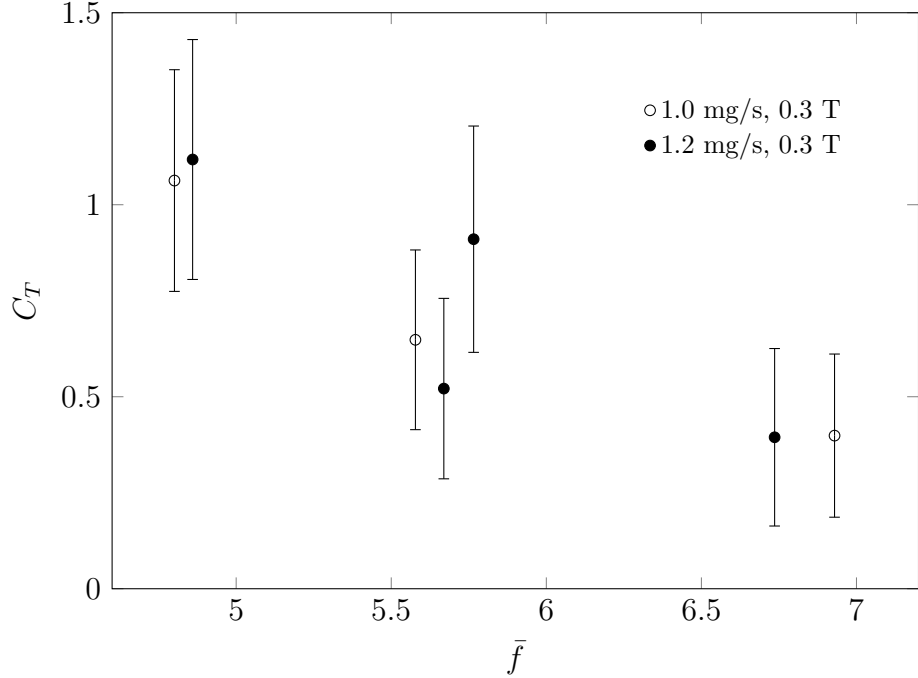


Figure 5.2: C_T as a function of \bar{f} for the 12 kW H2-4F hydrogen thruster.

\bar{f} , the scaling is different for each tested mass flow rate and magnetic field strength. In contrast, \bar{f}_p nearly completely captures the scaling of C_T .

Performing the same comparison for the MAI 150 kW lithium thruster (Figs. 5.4 (a) and 5.4 (b)) [16, 23, 24, 25], we again see that $\bar{f} < 1$, and that C_T typically increases with \bar{f} for a given mass flow rate and applied field strength. As with the case of the MAI 30 kW thruster, \bar{f}_p more completely captures the scaling of C_T irrespective of the mass flow rate and applied field strength. The exception to this trend is the data taken at 81 mg/s mass flow rate and 0.09 T applied field strength. However, the trend is strongly supported by the data taken at 80 mg/s and at the same applied field strength. We would not expect a 1.3% change in mass flow rate to have such a profound effect on C_T , and we observe that larger changes in mass flow rate at the same applied field strength have little effect. C_T behavior as a function of \bar{f}_p is nearly identical for the data taken at 80, 85, and 95 mg/s.

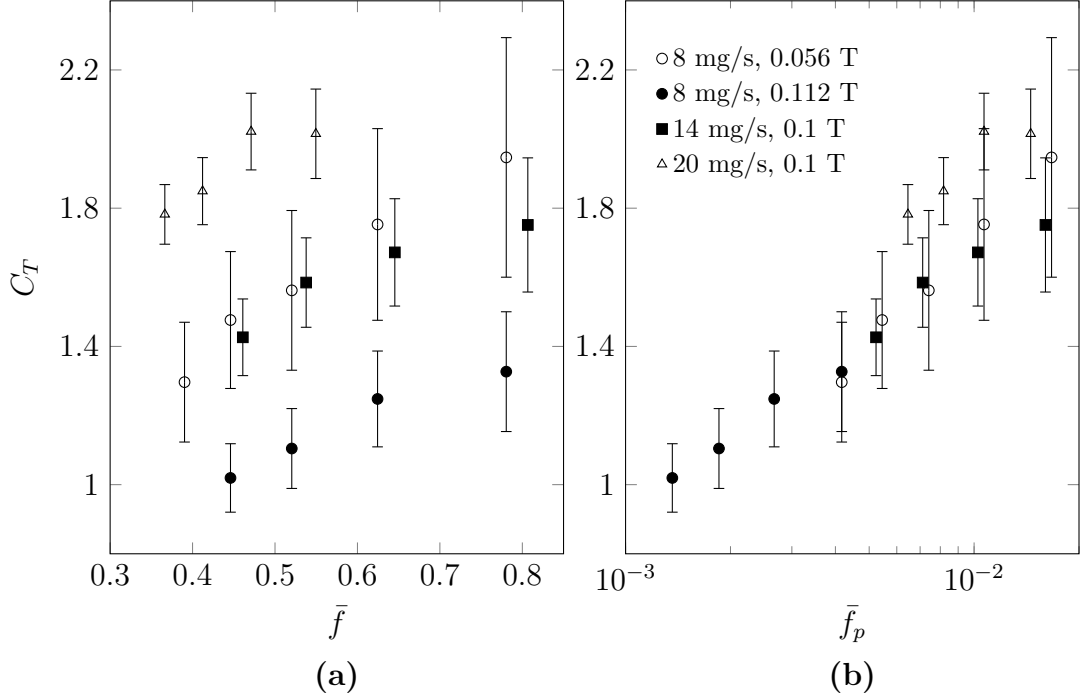


Figure 5.3: C_T as a function of \bar{f} (a) and \bar{f}_p (b) for the 30 kW MAI lithium thruster.

It therefore seems most likely that the anomalous data taken at 81 mg/s is not characteristic of the thruster performance.

For cylindrical thrusters, there is no ambiguity about the anode radius, however the internal forces can still affect the mass distribution within the anode and, therefore, the swirl and pinch thrust components. In Fig. 5.5, we show how C_T varies as a function of \bar{f}_p for the cylindrical 100 kW LeRC-A argon thruster [9]. Because current was only varied for a single mass flow rate and magnetic field strength, the scaling as a function of \bar{f} is similar, and we cannot say which is the more relevant scaling parameter, however the thrust coefficient increases monotonically with each parameter, which is consistent with previous observations when $\bar{f} < 1$.

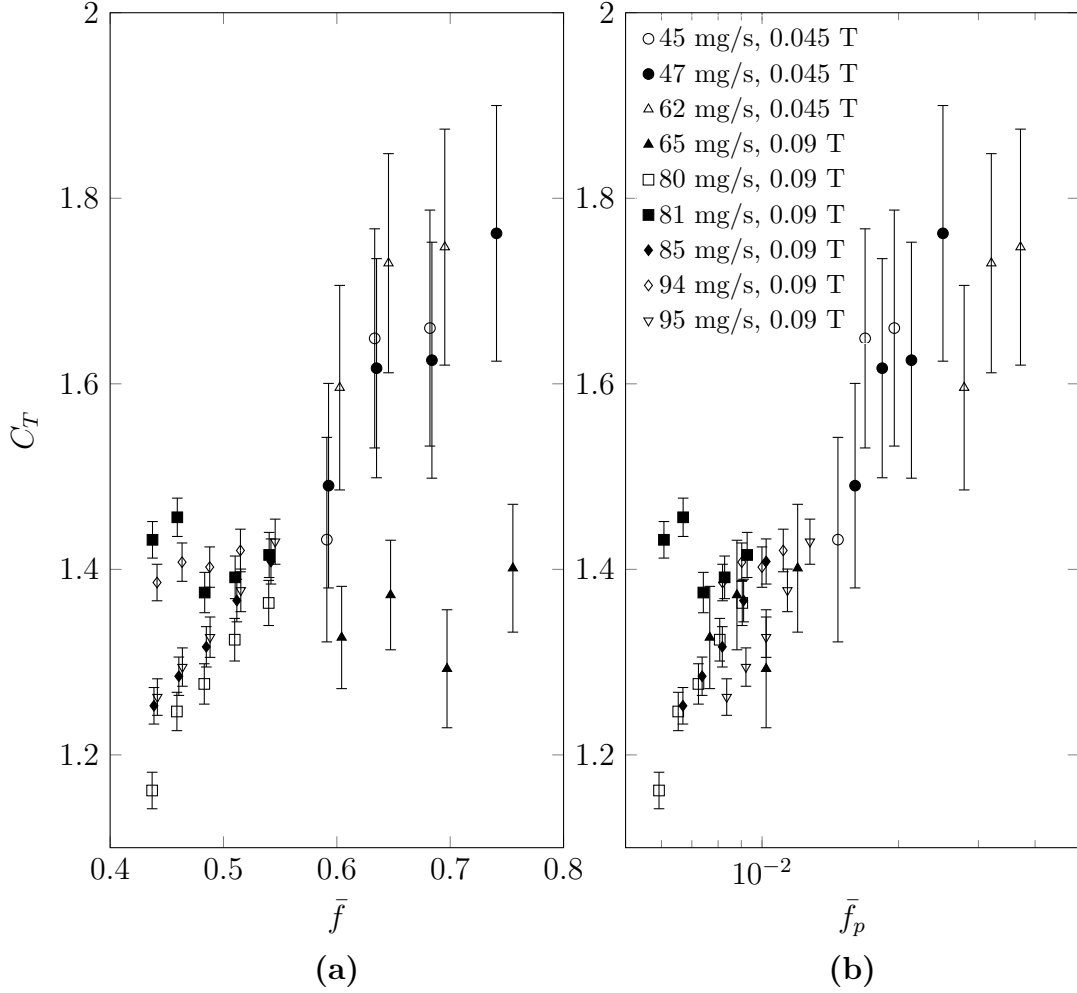


Figure 5.4: C_T as a function of \bar{f} (a) and \bar{f}_p (b) for the 150 kW MAI lithium thruster.

5.3 Applied-field thrust scaling

In the previous sections, we saw that C_T is at a maximum when $\bar{f} \approx 1$. When $\bar{f} > 1$, a thruster is operating in a magnetic-confinement mode analogous to onset, in which the anode is starved of charge carriers. Because such operation is not well-described by our scaling parameters, we will focus on the anode-confinement mode, in which $\bar{f} < 1$.

While a qualitative comparison of Figs. 5.3 (a) and 5.4 (a) to Figs. 5.3 (b) and 5.4 (b) shows \bar{f}_p to be more relevant to thrust generation than \bar{f} when operating in an anode-confinement mode, we can also compare the two parameters quantita-

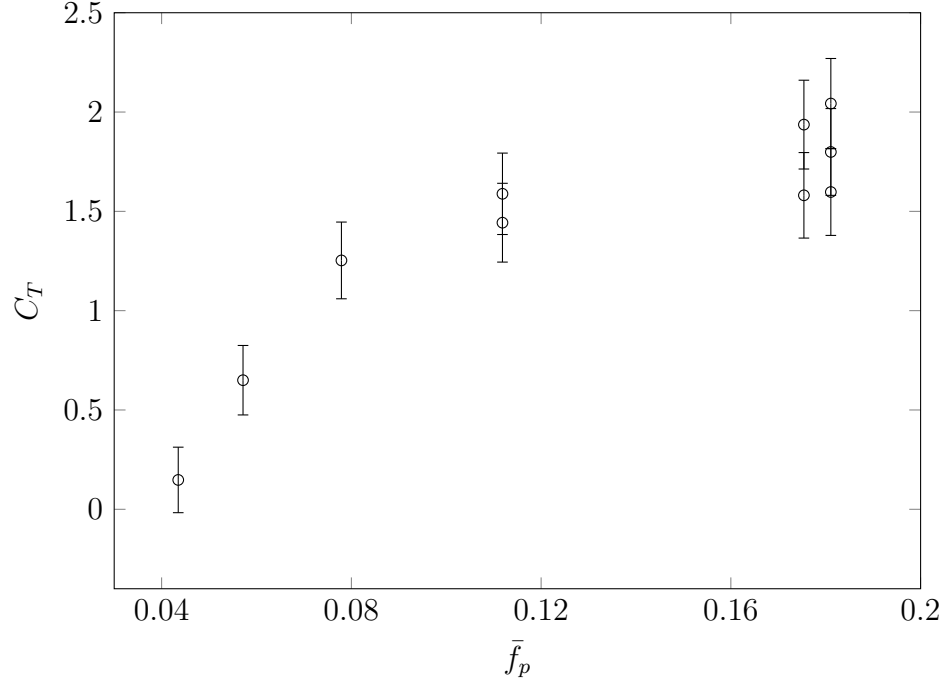


Figure 5.5: C_T as a function of \bar{f}_p for the 100 kW LeRC-A, operating at 0.034 T with argon at 100 mg/s.

tively by fitting to a power law as we did in Chapter 3. Based on our findings in Chapter 4, we assume that the thrust is described by the relation

$$T = T_{\text{GD}} + T_{\text{SF}} + k J B_A \bar{r}_\omega (r_{\text{ae}}, r_c, r_{\text{a0}}, \alpha) \sqrt{\frac{4r_{\text{ae}}^2 + r_{\text{ae}}r_{\text{a0}} + r_{\text{a0}}^2}{12}} \bar{f}^{\kappa_1} \bar{f}_p^{\kappa_2}. \quad (5.2)$$

We solve for the κ_1 and κ_2 values that minimize the relative standard deviation between prediction and measurement, and then find the k value such that the average prediction provides the value of the measurement. Following this procedure separately for the 30 and 150 kW MAI thrusters, we find the results summarized in Table 5.2. In addition, we apply the same method to the Tikhonov et al. model, using the average anode radius. The relative standard deviation, \hat{s} , is given for each thrust model, where $\hat{s}_{\text{Tikhonov}}$ is that of the Tikhonov et al. model.

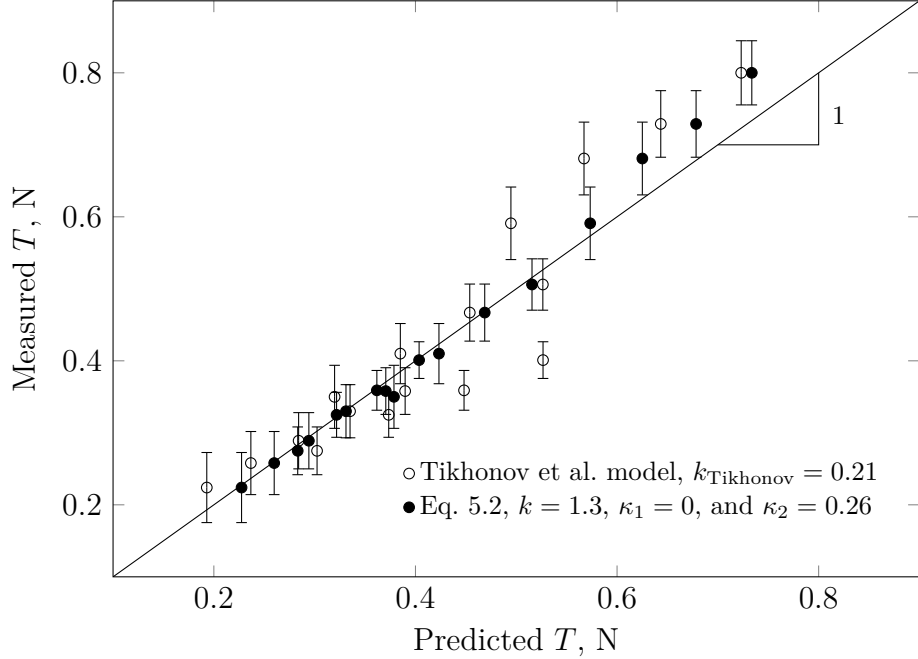


Figure 5.6: Thrust measurement versus prediction for the 30 kW MAI lithium thruster.

We find that, while the relative standard deviation is substantially reduced when \bar{f} and \bar{f}_p are incorporated into a thrust model, the κ_1 and κ_2 values differ substantially between the two thrusters, indicating that the values do not represent a universal scaling. However, in each case, κ_2 is substantially larger than κ_1 , supporting our previous assertion that \bar{f}_p is the more relevant parameter to thrust generation when $\bar{f} < 1$. We can therefore repeat our analysis assuming that $\kappa_1 = 0$. Doing so, we find that $\kappa_2 = 0.26$ for the 30 kW thruster and 0.18 for the 150 kW thruster, with relative standard deviations of 0.068 and 0.047 respectively. The assumption that $\kappa_1 = 0$ is justified by the fact that κ_2 and \hat{s} are nearly unchanged from the case when $\kappa_1 \neq 0$. We therefore conclude that \bar{f} is only an important parameter insofar as it determines the mode of confinement. When $\bar{f} < 1$, $r_{\text{sep}} = r_{\text{ae}}$ and the applied-field thrust scales with \bar{f}_p .

In Figs. 5.6 and 5.7, we show the measured total thrust as a function of the predicted thrust for the 30 and 150 kW thrusters respectively. We show the predicted

Table 5.2: Constants found by comparison to data.

Thruster	κ_1	κ_2	k	\hat{s}	k_{Tikhonov}	$\hat{s}_{\text{Tikhonov}}$
MAI 30 kW	-0.18	0.29	1.34	0.055	0.17	0.25
MAI 150 kW	0.07	0.17	0.68	0.047	0.15	0.12

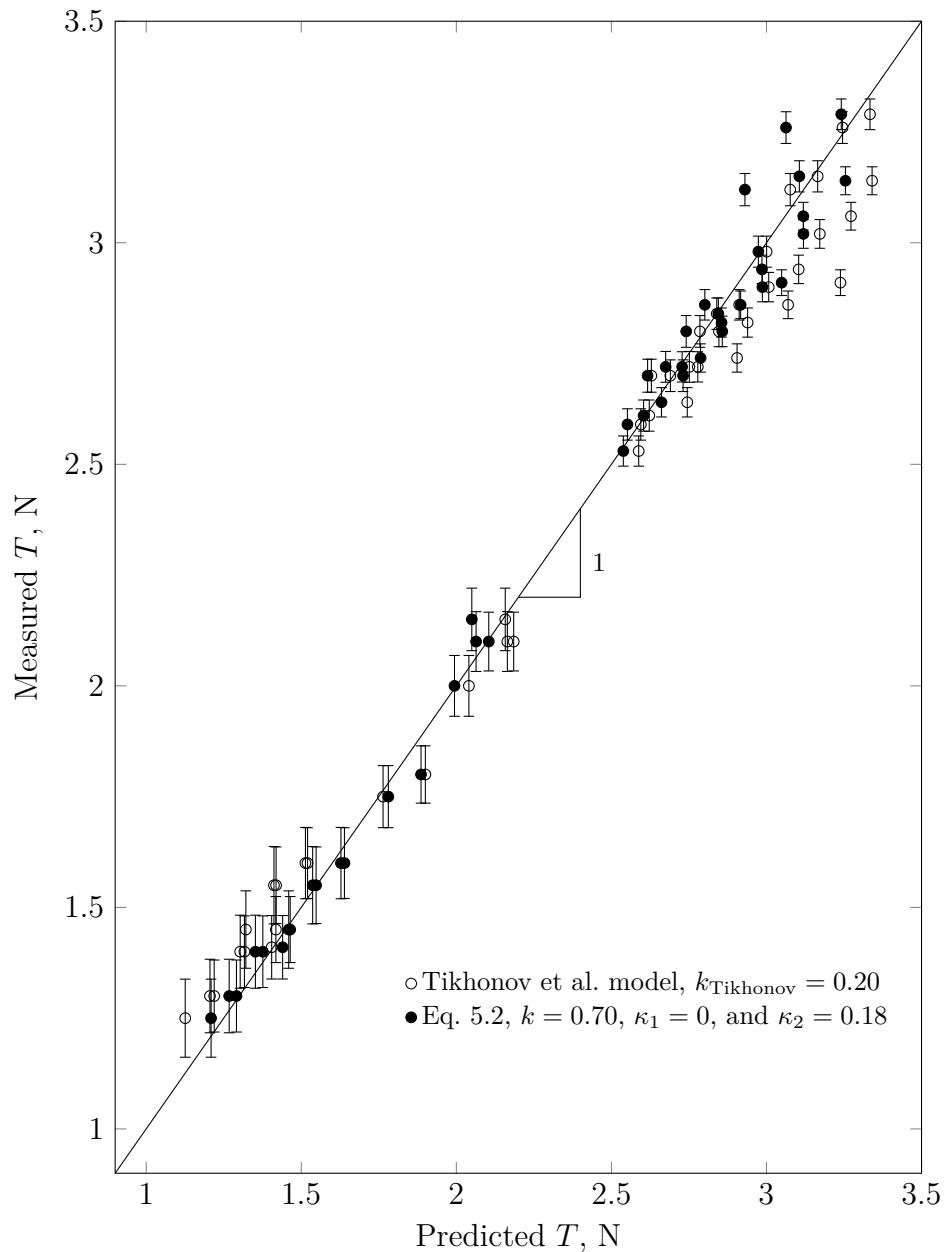


Figure 5.7: Thrust measurement versus prediction for the 150 kW MAI lithium thruster.

value by our model (Eq. 5.2) where $\kappa_1 = 0$ and by the Tikhonov et al. model. We see in Fig. 5.6 that the predictions of Eq. 5.2 are nearly always within an error bar of the agreement line. The predictions of Tikhonov et al. are close to measurement for low thrust values, but diverge from the measured value markedly in two locations. First, there is a departure below the line representing agreement where the predicted value is ≈ 5 N. These data are the highest current and magnetic field strength measurements taken for the lowest mass flow rate. The other main point of departure is for the largest four thrust measurements, which are substantially larger than the predicted value. These represent the highest mass flow rate data, which were taken at a constant magnetic field strength. Because $\bar{f}_p \propto \left(\frac{\dot{m}}{JB_A}\right)^2$, the model incorporating \bar{f}_p is able to account for both deviations from the Tikhonov et al. model.

In Fig. 5.7, we again see that Eq. 5.2 more closely predicts the measurement than does the Tikhonov et al. model. The latter model tends to underpredict the measurement for smaller thrust values and overpredict the measurement for larger thrust values. The two outlying data points for which Eq. 5.2 underpredicts the measurement are the same anomalous data points referred to in the previous section.

We have by no means found a universal thrust formula, as the magnitudes of the free parameters in Eq. 5.2 differ substantially between thrusters. The different values may be due to our assumption that the $T_i = 2$ eV or that $k_{GD} = 1$. Any future testing campaigns conducted with the intention of determining thrust scaling should therefore include measurements of T_i . In addition to measurements of total thrust, measurements of the applied-field thrust component remove the need for assumptions about the value of k_{GD} .

We observed in Chapter 2 that although the model of Mikellides and Turchi could not be applied to all thrusters, for those it could be applied to, the prediction that $T_{AF} \propto \sqrt{\dot{m}JB_A}$ was generally in agreement with measurement. Their model cannot be applied to the MAI thrusters, as each of these thrusters has a recessed cathode

and they predict that $T_{\text{AF}} \propto l_c^{-1}$. However, a value of $\kappa_2 = 0.25$, which is between the values found for these two thrusters, yields the same $T_{\text{AF}} \propto \sqrt{\dot{m}JB_A}$ scaling. We found that the physical explanation provided by the Mikellides and Turchi model—that viscous heating is one of the primary acceleration mechanisms and that viscous effects significantly limit the rate of rotation—does not correctly describe the underlying physics of most thrusters in the literature, but rather the one specific thruster that was numerically simulated by the model. In the presented work, we have found a similar scaling justified by different physical mechanisms, namely the scaling of azimuthal kinetic energy within the anode, and the pressure on the tip of the cathode, due to pinching forces.

Chapter 6

Applied-Field Thrust Component

Measurements⁵

In the previous chapter, we demonstrated that the thrust coefficient scales with the confinement parameter when $\bar{f} < 1$. Here, we will verify that the demonstrated scaling is not due to our assumptions about the gasdynamic and self-field thrust components by directly measuring the applied-field thrust component. A detailed description of the facilities in which these measurements were taken can be found in Appendix C.

⁵This chapter is based on work accepted for publication in [71]: W. J. Coogan, M. A. Hepler, and E. Y. Choueiri, “A Method for Measuring the Applied-Field Thrust Component of Plasma Thrusters,” In *Journal of Propulsion and Power*.

Similar work was also presented in [72]: W. J. Coogan, M. A. Hepler, and E. Y. Choueiri, “Measurement of the Applied-Field Component of the Thrust of a Lithium Lorentz Force Accelerator,” In *AIAA Propulsion and Energy 2016*, AIAA-2016-4537, Salt Lake City, UT, July 25–27, 2016. doi:10.2514/6.2016-4537

The applied-field thrust measurements taken with the ALFA were previously presented in [73]: W. J. Coogan and E. Y. Choueiri, “Applied-Field Topology Effects on the Thrust of an MPDT,” In *35th International Electric Propulsion Conference*, IEPC-2017-182, October 8–12, 2017.

6.1 Direct measurement of the applied-field thrust component

Because we seek to verify the applied-field thrust component scaling without making assumptions about other thrust components, we developed a thrust stand with which to directly measure the thrust generated by the application of a magnetic field. Solenoid thrust stands have been investigated previously for helicon plasma thrusters with magnetic nozzles operating at low currents ($J_B \leq 6$ A) [74]. However, the techniques used in these studies are poorly suited to the high currents ($J_B \leq 350$ A) typical of our argon and lithium Lorentz force accelerators (ALFA and LiLFA respectively). The higher currents require cooling and a means of calibrating for electromagnetic tare forces. In this section, we describe the solenoid thrust stand we developed for high-current applications, along with the measurement and calibration procedures.

6.1.1 Thrust stand

In order to directly measure the applied-field thrust component, we constructed an inverted pendulum thrust stand, similar to that used to measure the total thrust on a high-power AF-MPDT described by Haag in Ref. [75]. The difference is that the flexures support only the solenoid (illustrated in Figs. 6.1 and 6.2), which can move independently of the thruster, which is fixed to the lab reference frame. Because the applied-field component of the thrust exerts an equal and opposite force on the solenoid, a calibrated measurement of the deflection of this inverted pendulum is a direct measurement of the applied-field thrust component.

In order to accommodate the current and cooling requirements of our solenoid without impeding the motion of the thrust stand, copper pipes (0.375" OD, 0.245" ID) are used as the flexures, which carry all necessary current and cooling. The dimensions of the flexures are based on the design criteria outlined in Ref. [75], the dimensions of

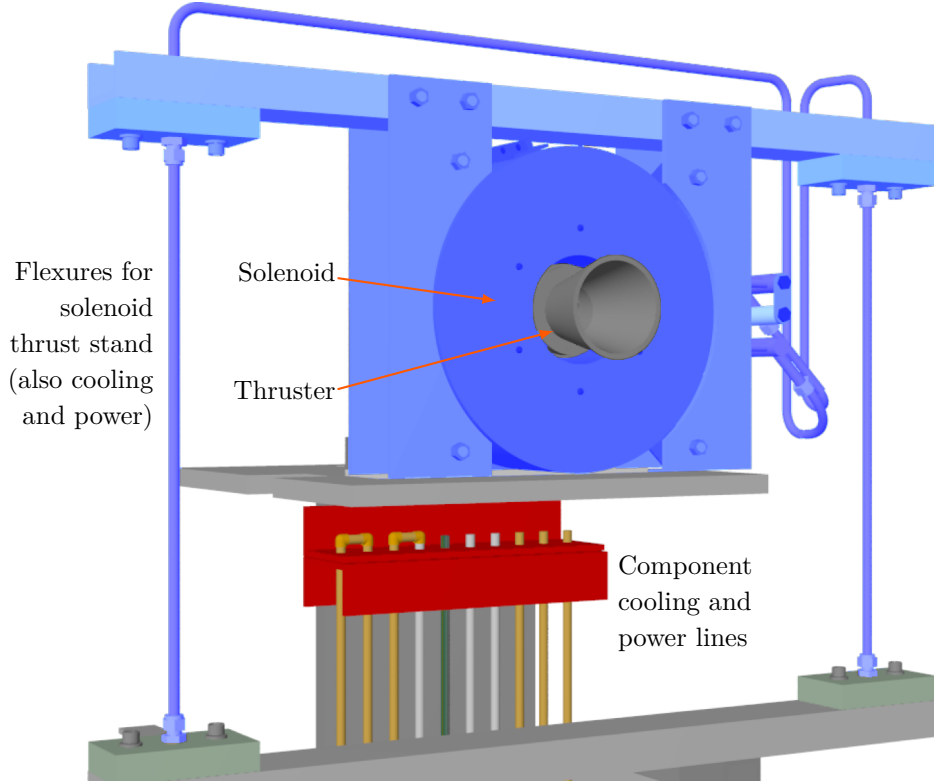


Figure 6.1: Solenoid thrust stand for measurement of the applied-field component of the thrust. Moving components are shown in blue.

our vacuum facility, and the sensitivity of our linear variable differential transformer (LVDT). Because the temperature and spring constant of the flexures are functions of current through the solenoid, an open-cycle cooling system was implemented and found to reach steady-state operating temperature in under two minutes for any current level in our operational range of up to 350 A. No change in flexure temperature was observed while firing the thruster.

The force exerted on the solenoid is augmented by electromagnetic tare forces from azimuthal currents to the thruster electrodes in proximity to the solenoid. The tare forces between the flexures and the components carrying current to the thruster electrodes were minimized by separating the two as much as possible within the constraints of the vacuum tank dimensions. We considered two methods to account for this tare force. The first method consists of making a measurement for a given

set of operating parameters and then repeating that measurement with the solenoid current running in the opposite direction. The force from the applied-field thrust will be the same in each instance, but the tare force will be in opposite directions. The average of the two measurements is then equal to the applied-field thrust component.

In the second method, the measurement is repeated with the thruster electrodes physically shorted. This measurement provides the tare force, which can then be subtracted from the measurement made while firing. This method requires that the short does not contribute to, or subtract from, the preexisting azimuthal currents, which means it must be strictly radial and within the thruster volume. We tested each method and present the results in Sec. 6.1.3.

The applied-field thrust component is dependent on the shape and strength of the magnetic field within the anode, and so care must be taken to ensure that the motion of the solenoid does not significantly alter either of these parameters. For all measurements in the presented work, the magnetic-field strength at the exit was within 0.22% of the thruster-off value, and the angle of the solenoid was within 0.03° of the thruster-off value. Since the applied-field thrust is approximately proportional to the applied-field strength, these small deviations can be neglected.

6.1.2 Thrust measurement procedure

To correlate deflection with force, we measure the deflection of the thrust stand using a Macro Sensors PR 750-100 LVDT, which has a sensitivity of 155 mV/V/mm. After the solenoid coolant reaches steady state, we fire the thruster and record the voltage from the LVDT. Then, the thruster current supply is turned off, but the solenoid is left on at a constant current. This ensures that the temperature of the flexures, and the magnetic forces on nearby metallic surfaces, remain constant. A second voltage is recorded. The difference in voltage between the two measurements represents the distance the thrust stand was deflected.

To calibrate the deflection measurement, a known force is applied to the pendulum. For forces under a few newtons, the change in voltage measured as a result of deflection of the thrust stand was found to be linear with force. Therefore, application of a single known force, in addition to the calibration-off measurement, is sufficient to calibrate a voltage measurement. However, the measurement was repeated at a number of force levels after each deflection measurement to ensure the linearity of the response.

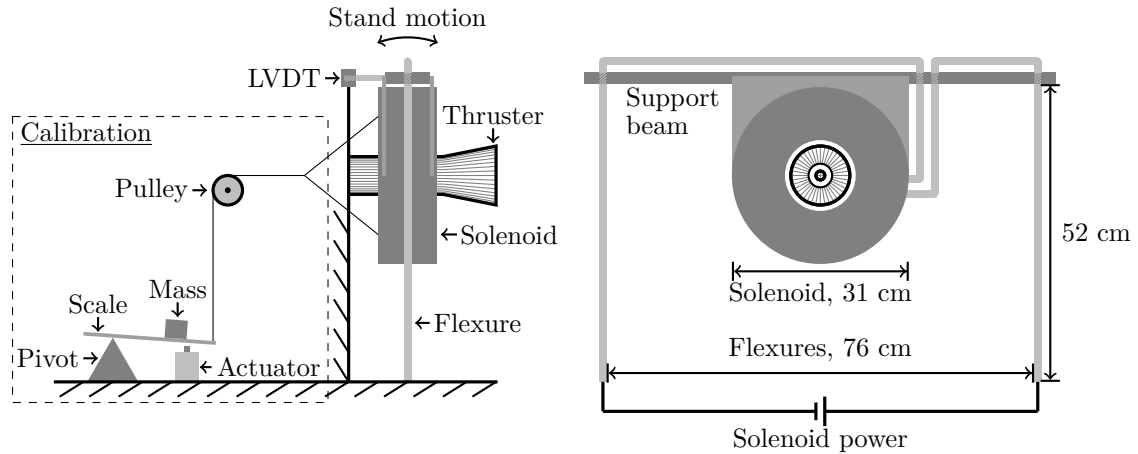


Figure 6.2: Calibration is performed in situ via a mass that can be translated along a scale. An actuator is used to apply the calibration mass.

We apply a known force by means of an actuator and a scale, as is schematically illustrated in Fig. 6.2. The scale translates a mass back and forth through remote control. A cable is strung from the end of the scale over a pulley and attached to the back end of the thrust stand along the thrust axis. As the mass moves further from the pivot point, the scale applies a greater calibration force to the thrust stand. The correlation between mass position and force is determined by suspending masses from the same pulley and comparing the outputs of the LVDT, as is illustrated in Fig. 6.3. The LVDT output was found to be linear with force up to 1.2 N, with $R^2 = 0.9996$.

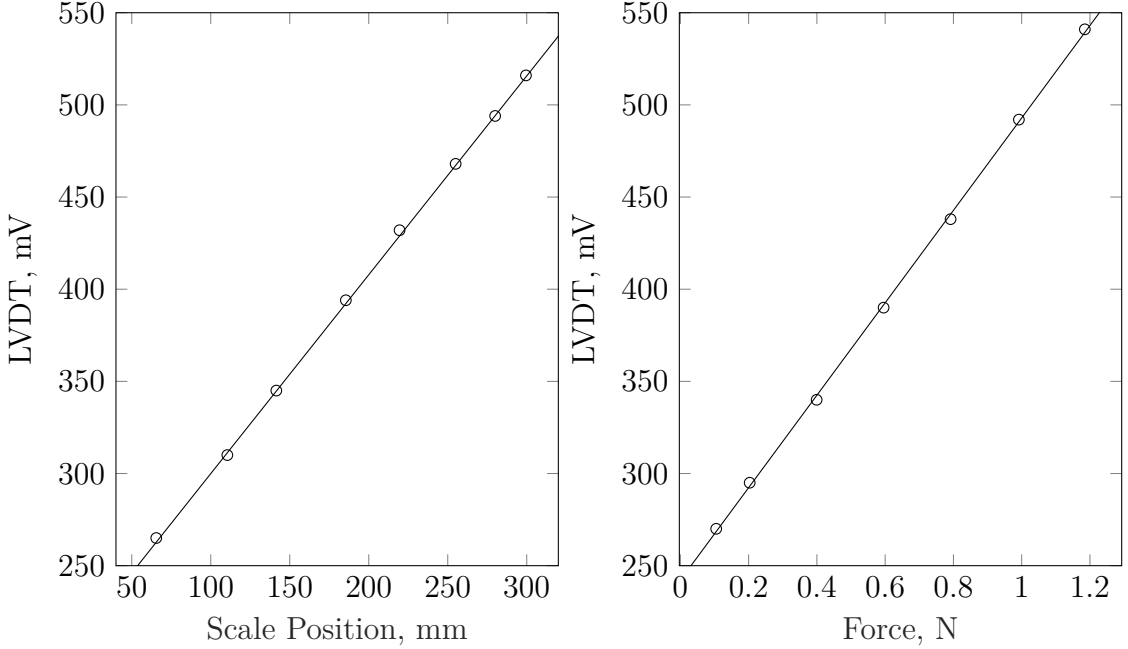


Figure 6.3: LVDT voltage as a function of scale position (left) and known force (right) when $B_A = 0$. The typical error is ± 2 mV.

6.1.3 Initial test

We fired the LiLFA at 400 A at steady state, with an applied field strength of 0.056 T, and a lithium mass flow rate of 8 mg/s. Background pressure was maintained under 5×10^{-5} Torr. We made two measurements for the same operating parameters, as is shown in Fig. 6.4. First, we measured the total deflection of the stand with the electromagnetic tare force parallel to the thrust. We then reversed the current direction through the solenoid and took a second measurement. Each deflection measurement consists of the average LVDT output taken over a 10 to 15 second interval.

We calibrated the thrust stand with its flexures at operating temperature and measured a sensitivity of 3.4 mN/mV. Averaging the deflection measurements from each solenoid configuration yields an applied-field thrust of 108 ± 14 mN. We shorted the thruster, and measured an electromagnetic tare force of 137 ± 17 mN, which, subtracted from the parallel force measurement, and added to the antiparallel force measurement, yields an applied-field thrust of 106 ± 19 mN and 111 ± 20 mN, re-

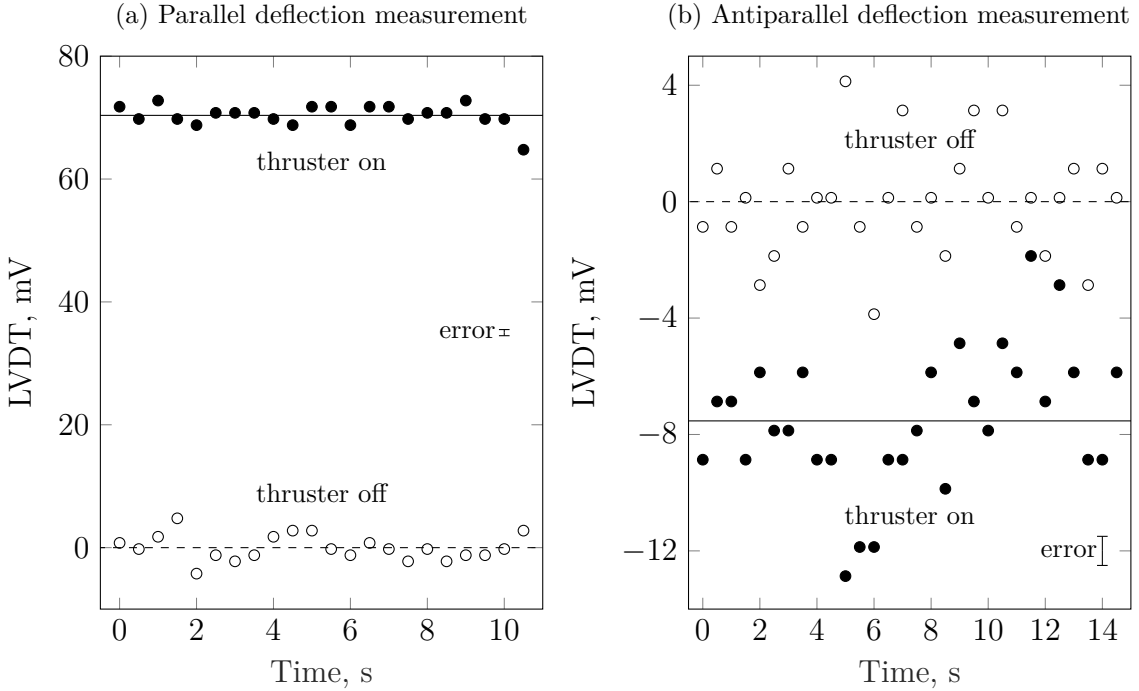


Figure 6.4: The deflection of the thrust stand as measured by an LVDT with the electromagnetic tare force parallel to the thrust (a) and antiparallel to the thrust (b). These measurements were taken at 400 A, with an applied field strength of 0.056 T, and a lithium mass flow rate of 8 mg/s.

spectively. The magnitude of the tare force, which is larger than the thrust, indicates that there is a significant azimuthal current path to the thruster near the solenoid. All results are summarized in Table 6.1.

Our three thrust measurements for the same operating conditions are in agreement. In addition, all three methods provide applied-field thrust component values that are less than the total thrust (224 mN) measured with equivalent operating conditions [69] and within the range of values predicted by the model of Tikhonov et al. [16] for applied-field thrust (99 to 197 mN). We recommend future experimental campaigns employ the first method used, where the solenoid is run in both directions and the measurements from each configuration are averaged. This method is preferred because measurements can be made during a single operating period without venting the vacuum tank. In addition, we avoid inadvertently adding to or subtracting

from the existing azimuthal currents to the thruster electrodes through an artificial electrical short that may not be strictly radial. This method also avoids damage due to high temperatures resulting from large currents through an electrical short in the thruster volume.

Table 6.1: Results of each thrust measurement method for the LiLFA operating at 400 A, with an applied field strength of 0.056 T.

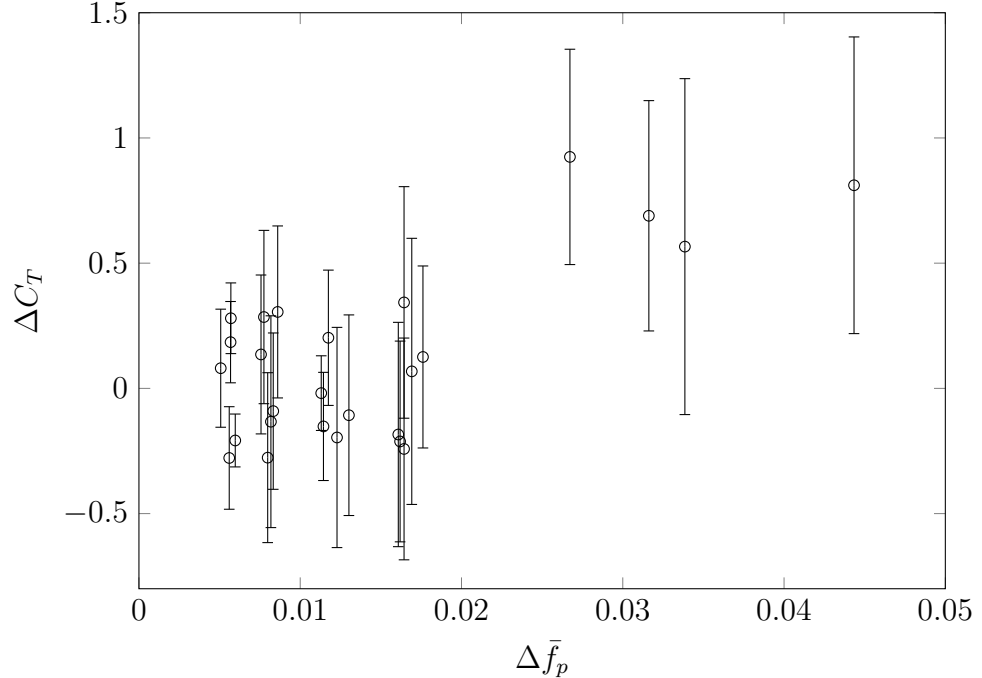
Method	Measurement	Error
Alternating B -field	108 mN	± 14 mN
Parallel tare	106 mN	± 19 mN
Antiparallel tare	111 mN	± 20 mN

The 13% error in our thrust measurement is due to the variability in position, which did not scale with the magnitude of the measurements made. Consequently, we anticipate smaller relative errors in a higher-thrust regime.

6.2 Measurements of ΔT_{AF} with constant EM tare force

In certain instances, it is possible to reduce the error by streamlining the measurement process. For instance, a single deflection measurement can be used to investigate the dependence of the applied-field thrust, T_{AF} , on mass flow rate, \dot{m} , which can be changed while firing without affecting the electromagnetic tare force. In this case, we do not know the value of T_{AF} , but we can still determine ΔT_{AF} as a function of \dot{m} .

In addition to eliminating one source of error from the measurement, this method allows the duplication of the position measurement using a General Electric model 3300 8MM proximitator. The proximitator has a limited range compared to the LVDT, but provides an order of magnitude greater resolution. In order to keep the proximitator within range of the thrust stand, its position can be adjusted while firing by use of



increased or decreased when the mass flow rate was decreased. All measurements were taken at background pressures less than 0.3 mTorr.

In Fig. 6.5, we see that the applied-field thrust component increases with increasing mass flow rate, which has not previously been demonstrated. Further, we see that the magnitude of this increase is dependent on current. At high current, the change in mass flow rate results in small changes in \bar{f}_p and the error bars typically include a null change in thrust. However, at lower currents, $\Delta\bar{f}_p$ is larger for a given mass flow rate change, and we are able to measure a substantial change in C_T .

Chapter 7

Conclusions

In this dissertation, we investigated the acceleration mechanisms of applied-field magnetoplasmadynamic thrusters. We sought to determine which operating and geometric parameters influence the thrust and what underlying physical mechanisms are responsible for thrust generation. In addition, we sought a means of directly measuring the applied-field thrust component so that models of the applied-field thrust could be directly compared to experiment without making assumptions about the self-field and gasdynamic thrust components.

7.1 Significant contributions

7.1.1 Data comparison methodology and assembly of data catalog

For any AF-MPDT study requiring the comparison of numerous geometries, electrode material effects, or facility effects, the AF-MPDT database is a vital resource. It is impractical for a single researcher to build numerous thrusters, or to test in diverse facilities. It is our hope that the work that went into assembling all thrust data

into a single database [7] will be made more worthwhile by the significant findings of numerous future researchers.

In addition to assembling the AF-MPDT database, we developed a novel method for analyzing large quantities of data using dimensional analysis. We applied this method to applied-field thrust models, but the same technique can be applied to any field of study for which there is both a theoretical model and data containing all necessary parameters for the model.

7.1.2 Method of directly measuring the applied-field thrust component

For most AF-MPDT thrust models, the only difference between models is in how the applied-field thrust component is modeled. However, prior to the research contained in this dissertation there were no direct measurements of the applied-field thrust component of an AF-MPDT. Measurements of the thrust generated by magnetic nozzles on other thrusters were made for solenoid currents ≤ 6 A. The development of a method with which to measure the applied-field thrust directly with solenoid currents up to 350 A represents a significant advancement in the state of the art. In this work, we used this thrust stand to show that the mass flow rate is one of the controllable parameters that affects the applied-field thrust component. In a measurement of the total thrust, a change in thrust resulting from varying the mass flow rate might be attributed to the gasdynamic thrust component.

7.1.3 Analytical and experimental findings

Our analytical studies, combined with the experimental data of numerous thrusters shed light on a number of physical insights and empirical observations. These are summarized as follows:

- The applied-field thrust component is *not* proportionate to current or applied-field strength as has been assumed in much of the literature. We found that in the case of two lithium-fed thrusters, the applied-field thrust is more closely proportionate to $\sqrt{JB_A}$.
- The applied-field thrust component depends on mass flow rate. Whereas most previous models predict no dependence on mass flow rate, our findings indicate that in the case of two lithium-fed thrusters the applied-field thrust is approximately proportionate to $\sqrt{\dot{m}}$.
- The radial forces within the anode play a significant role in determining the thrust. We showed that there are two distinct modes of operation: a magnetic-confinement mode, and an anode-confinement mode. We showed that in the latter mode, the thrust coefficient for a given thruster is solely a function of the confinement parameter for parameter values as high as one. In this regime, the thrust coefficient increases with an increasing confinement parameter. For confinement parameter values greater than one, the thruster is in the magnetic-confinement mode, and the trend is in the opposite direction due to the decreased volume of the plasma column. This decrease in volume is detrimental to the swirl component of the thrust because of the corresponding reduction in azimuthal kinetic energy.

7.2 Future work

In this work, we have furthered our understanding of how the applied magnetic field contributes to thrust for AF-MPDTs. However, in shedding light on the underlying physics, we have also brought forth a number of avenues for possible further research. Although we have assembled an extensive database of thrust data, the fact that most of the data were taken at high background pressures (≥ 1 mTorr), and that

much of the data were taken in a regime where either gasdynamic or self-field thrust components are significant, means there remains a great deal of experimental work to be done in order to put the nail in the coffin for AF-MPDT thrust models. In order to assess that a thrust model correctly describes the dependence of thrust on geometric parameters, an extensive campaign must be undertaken to test varying geometries. To this end, an AF-MPDT similar to the hybrid plasma thruster [49] (the anode of which consists of strips of copper that are not continuous azimuthally) can be constructed in such a way that the inner and outer anode radii can be independently varied. Such a device would allow a single researcher to study geometric effects without constructing numerous thrusters.

Because our goal was to derive a scaling parameter analytically, we made the assumption that flow through the anode is quasi-one-dimensional, but we show that it is specifically when this assumption fails—when the outward radial force is larger than the inward radial force or vice versa—that the radial forces can affect the thrust in a predictable way. A two- or three-dimensional computational model may therefore be able to predict the thrust without relying on scaling parameters that require input from data.

We have assumed that the efficiency with which the swirling motion within the anode is redirected into axial kinetic energy is universal, when in actuality it will depend on a number of geometric and operating parameters. A rigorous study of the physics taking place in the magnetic nozzle of an AF-MPDT has yet to be completed. However, recent studies of magnetic nozzles have shed light on how a similar process works for a heated plasma [65]. Extending these studies to a swirling plasma would constitute a major contribution to our understanding of how the applied-field contributes to thrust.

Finally, whenever we are able to further our understanding of thrust scaling, we can apply that knowledge to further our understanding of efficiency scaling. Our

findings in this dissertation can serve this end by two different means. First, the found thrust scaling can be used directly to calculate the energy going to thrust. Second, our scaling parameters representing the radial force balance can be used to develop a voltage model, as the plasma density at the anode wall plays a significant role in determining the anode sheath voltage fall [60].

Appendix A

Propellant Properties

The following table contains the values used for all calculations in this work requiring propellant properties.

Table A.1: Propellant properties used in analysis.

	H ₂	He	Li	N ₂	NH ₃	Na	Ar	K	Kr	Xe	Cs
M_i (u)	2.02	4.00	6.94	28.01	17.03	22.99	39.95	39.10	83.80	131.29	132.91
ϵ_i (eV)	15.42	24.59	5.39	15.58	10.20	5.14	15.76	4.34	14.00	12.13	3.89
γ	1.41	1.67	1.67	1.41	1.28	1.67	1.67	1.67	1.67	1.67	1.67

Appendix B

Catalogued Thrusters⁶

The following table lists each of the thrusters included in the AF-MPDT database [7] along with their typical operating parameters.

⁶This chapter is based on work being prepared to be submitted for publication and previously presented in [20]: W. J. Coogan and E. Y. Choueiri, “A Critical Review of Thrust Models for Applied-Field Magnetoplasmadynamic Thrusters,” In *AIAA Propulsion and Energy 2017*, AIAA-2017-4723, Atlanta, GA, July 10–12, 2017. doi:10.2514/6.2017-4723

Table B.1: Catalogued thrusters and their operating regimes.

Thruster	Principal Investigators	Power (kW)	B_A (T)	Propellants	p_b	Error	Electrode	Refs.
					(mTorr)	Reported?	Geometry	
Alta	Albertoni et al.	21–230	0–0.1	Ar	0.15	Y	conical, dir.	[15, 66, 67, 68]
H2-1	Cann et al.	38–89	0.1–0.3	H ₂	150	N	conical, del.	[57]
H2-2 (D – F)	Cann et al.	4–14	0.2–0.7	H ₂	20–40	N	cylindrical	[57]
H2-3B	Cann et al.	8–17	0.3	H ₂	50	N	cylindrical	[57]
H2-4 (A – E)	Cann et al.	7–13	0.3	H ₂	15–30	N	conical, del.	[57]
H2-4F	Cann et al.	4–13	0.3	H ₂ , He, N ₂ ,	0.05–70	N	conical, del.	[57]
HC-8	Fradkin and Roehling	14	0.2	Li	0.02	Y	cylindrical	[76, 77]
LAJ-AF (2 – 4)	Moore et al.	7–23	0.3–0.5	Li	0.7–	Y	cylindrical	[78]
					1000			

Thruster	Principal Investigators	Power (kW)	B_A (T)	Propellants	p_b	Error (mTorr)	Reported?	Geometry	Electrode	Refs.
LAJ-AF-6D	Cann et al.	3–34	0.2–0.5	Li, Na, K	0.5	Y/N		cylindrical	[79, 56, 57]	
LAJ-BF-1D	Cann et al.	4–16	0.08–0.2	K	0.1	Y		cylindrical	[56]	
LAJ-CF (3 – 5)	Moore et al.	6–38	0.5	Li	30–1000	Y		cylindrical	[78]	
LaRC	Grossmann et al.	8–36	0.1–0.6	Ar	5	N		cylindrical	[80, 81]	
LeRC-A0	Mantenieks, Myers, et al.	20–48	0–0.3	Ar	0.5	Y		conical, del.	[82, 29, 75]	
LeRC-B0	Mantenieks, Myers, et al.	30–45	0.02–0.2	Ar	0.5	Y		conical, dir.	[82, 29, 75]	
LeRC-C0	Myers et al.	29–72	0.02–0.04	Ar	0.5	Y		cylindrical	[29, 75]	
LeRC-A	Myers	15–87	0.03–0.2	H ₂ , Ar	0.5	Y		cylindrical	[9, 83, 52, 84]	

Thruster	Principal Investigators	Power (kW)	B_A (T)	Propellants	p_b (mTorr)	Error Reported?	Geometry	Electrode Refs.
LeRC (B, C, E – G)	Myers	24–120	0.03–0.2	Ar	0.5	Y	cylindrical	[9, 83, 52, 85]
LeRC-H	Myers	38–59	0.03–0.1	Ar	0.5	Y	conical, dir.	[83, 52]
MAI-30kW	Kim et al.	12–38	0.06–0.1	Li	5	Y	conical, dir.	[69]
MAI-130kW et al.	Tikhonov	53–120	0.05– 0.09	Li	4	Y	conical, dir.	[16, 24, 25, 23]
MAI-200kW et al.	Tikhonov	120–180	0.05–0.3	Li	5	Y	conical, dir.	[70, 86]
MY-I	Tahara et al.	230– 4,900	0–0.3	H ₂ , NH ₃	0.008	Y	cylindrical	[87]
MY-III	Tahara et al.	98– 4,900	0–0.5	H ₂ , NH ₃ , Ar	0.008	Y	conical, del.	[61, 28, 88, 27, 87]

Thruster	Principal Investigators	Power (kW)	B_A (T)	Propellants	p_b (mTorr)	Error Reported?	Electrode Geometry	Refs.
MY-III (C1-1, C1-3,	Tahara et al. 3,900	360– 0.05–0.5	H ₂ , NH ₃	0.008	Y	conical, del.	[61, 87]	
C1-3-CA.L, C1-3-CO.L, C2-12, C ² -23, C3-123)								
NaU-A et al.	Ichihara 0.7–3	0.1–0.3	Ar	0.4	Y	conical, dir.	[89, 47]	
ToU	Sasoh et al. 2–10	0.03–0.3	H ₂ , N ₂ , Ar	1	Y	conical, del.	[90, 91]	
SX3 et al.	Boxberger 30–114	0.4	Ar	2	Y	conical, dir.	[92, 93]	
WaU (s, m, l)	Nakano et al. 0.4–1	0.1–0.2	Ar	0.5	Y	conical, del.	[94]	
X-2C Bennett	John and 18–170	0.08–0.3	H ₂ , NH ₃	100	Y	conical, dir.	[30, 95]	

Thruster	Principal Investigators	Power (kW)	B_A (T)	Propellants	p_b (mTorr)	Error Reported?	Electrode Geometry	Refs.
X-2C-H ₂ O	John and Bennett	5–12	0.07–0.3	C ₈	0.1	Y	conical, dir.	[30]
X-2C-Rad	John and Bennett	4–7	0.01–0.3	Li	0.1	Y	conical, dir.	[30]
X-7 (s, m, l, xl)	Esker et al.	13–38	0.1–0.2	NH ₃	10	N	conical, del.	[96]
X-7 (C-1 – C-5, CR)	Bennett et al.	9–100	0.08–0.3	NH ₃	100	N	conical, del.	[31]
X9	Krülle	22–96	0–0.3	H ₂ , Ar	500	N	conical, del.	[1]
X13	Kurtz	5–89	0.1–0.4	Ar	10	N	cylindrical	[53]
X16	Krülle and Zeyfang	3–12	0.6	Ar, Kr, Xe	0.6	N	conical, del.	[55]

Appendix C

Experimental Apparatus

This chapter describes the facility and systems used to conduct all experimental work in this thesis. These include the vacuum and cooling systems, as well as two thrusters, the LiLFA and the ALFA, and their corresponding subsystems.

C.1 Steady-state MPDT facility

The steady-state MPDT facility (SS-MPDT-F) at Princeton University consists of a steel vacuum chamber, a cutaway view of which is illustrated in Fig. C.1. This chamber houses a 30 kW steady-state AF-MPDT (either the LiLFA or the ALFA) along with all subsystems required for thruster operation.

C.1.1 Vacuum

The ultimate pressure for the SS-MPDT-F is 1×10^{-5} Torr. Typical background pressures while operating with lithium and argon are $< 5 \times 10^{-5}$ Torr and $< 3 \times 10^{-4}$ Torr respectively. The lower pressure is achieved with lithium because it typically condenses upon contact with the cooled inner surface of the vacuum chamber and on the traps placed downstream of the thruster.

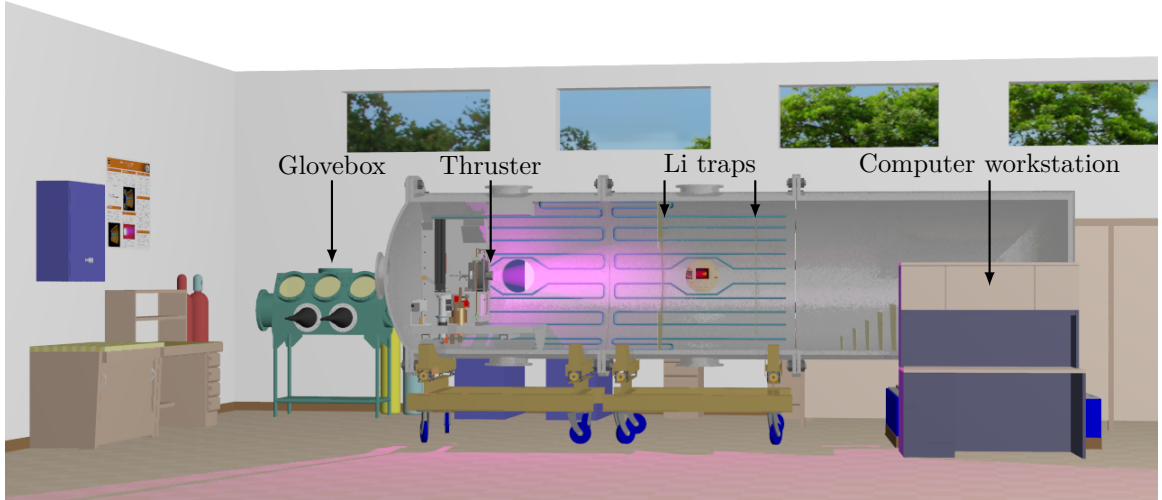


Figure C.1: A cutaway view of the steady-state MPDT facility is shown in its laboratory setting.

A schematic of the vacuum system is shown in Fig. C.2. Vacuum is achieved via a three-stage pumping system. The Stokes 212-H11 Microvac roughing pump brings the chamber from atmosphere down to < 5 Torr, and pumps at 71 l/s. The RUVAC WSU-2000 roots blower pumps at 633 l/s and further reduces the pressure to < 0.1 Torr. Ultimate vacuum is achieved using the 1.2 m CVC type PMC-48C diffusion pump, which displaces 95,000 l/s. The pressure is measured by a Terranova model 906 convection gauge above 1 mTorr and using an MKS 943 cold cathode gauge at lower pressures.

Lithium traps placed downstream of the thruster are cooled, as are the walls of the vacuum chamber. Because lithium is solid below 180 °C, lithium exhausted from the LiLFA condenses on these surfaces and does not add to the load on the pumping system.

C.1.2 Cooling

There are two separate processed chilled water lines. The first line is regulated by the campus cogeneration plant and is used to cool the roughing pump, the diffusion

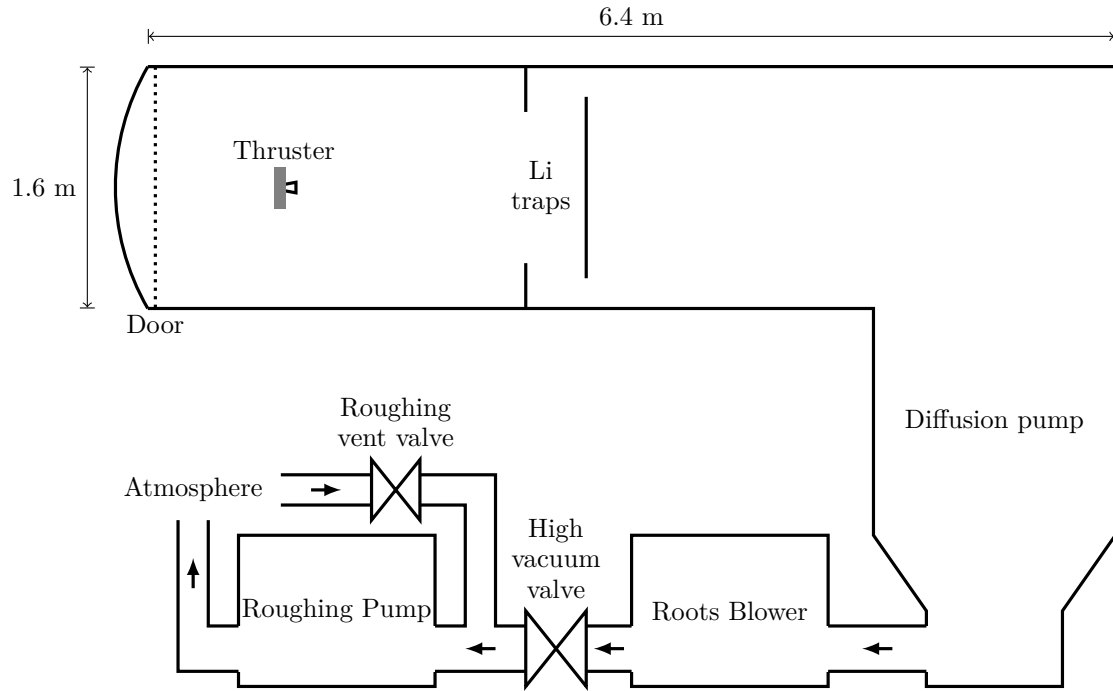


Figure C.2: Schematic of the steady-state MPDT facility vacuum system.

pump (which operates at 20 kW), and the jackets on the cables carrying the thruster current on the exterior of the vacuum chamber.

In addition to the 30 kW delivered to the thruster, an additional ≈ 3 kW goes to operating the solenoid and, when operating with lithium, ≈ 2 kW goes to melting and evaporating the lithium propellant. This power generates enough heat to melt many of the materials in proximity to the thruster. In order to avoid damaging equipment and to mitigate the effects of thermal expansion on our measurements, a second line, which is supplied by the engineering building, is used to cool components inside the vacuum chamber. This line is split into 7 different subsystems, as is illustrated schematically in Fig. C.3:

- 1. Chamber walls:** Pipes are welded to the interior front and middle sections of the vacuum chamber (shown as teal in Fig. C.1), which cool the chamber.

2. **Lithium feed system:** Cooling lines are used to freeze lithium at various points in the feed system. The freezing or thawing of lithium serves as a valve or seal. This cooling line includes the electrodes carrying current to the thruster in proximity to the feed system, as well as the table supporting the thruster.
3. **Solenoid:** The solenoid operates at up to 350 A, and requires active cooling. This cooling line includes the flexures in the applied-field component thrust stand.
4. **Flexures:** The flexures for the thrust stand measuring total thrust are cooled to limit thermal drift.
5. **Thruster shield and conductors:** A cooled baffle surrounds the anode in order to prevent lithium from being deposited upstream of the thruster. This cooling line includes the electrodes carrying current to the thruster at the top port cover.
6. **Diagnostics:** Any diagnostics requiring active cooling are connected to this line. In the present setup, this line is shorted.
7. **Lithium traps:** The right-most lithium trap shown in Fig. C.2 is cooled to assist lithium condensation.

The flow rate to each subsystem is regulated by gate valves.

While the second line previously ran through a heat exchanger in a closed-loop cooling system for the vacuum chamber subsystems, an open-loop system was recently implemented in order to obtain a near-constant input temperature, reducing thermal expansion of the thrust stand during thrust measurements.

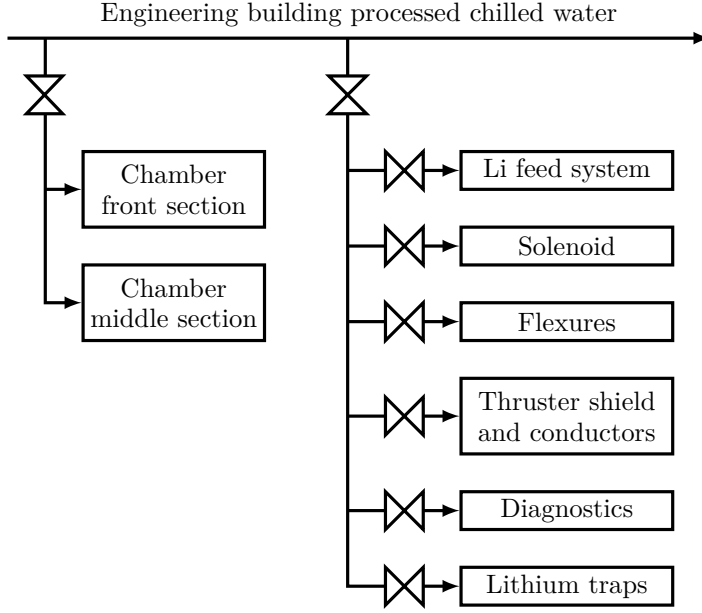


Figure C.3: Schematic of the steady-state MPDT facility cooling system.

C.2 The lithium Lorentz force accelerator

The lithium Lorentz force accelerator (LiLFA) is one of a series of lithium-fed applied-field magnetoplasmadynamic thrusters designed and built by the Moscow Aviation Institute (MAI) in the 1990s [97, 43, 17, 69, 24, 98, 25, 99, 70]. The LiLFA was designed to operate at up to 30 kW steady state, and was delivered to Princeton University in 1998.

The LiLFA is shown schematically in Fig. C.4. Its electrodes are each made of tungsten. The multichannel hollow cathode includes a channel for the propellant injection, as well as a separate chamber for a graphite heater, which evaporates the lithium. The evaporated lithium travels through the holes surrounding tungsten pins at the cathode exit, where ionization occurs. This style of cathode offers a number of advantages over a conventional solid rod cathode. First, the lithium phase change cools the cathode, reducing cathode erosion due to tungsten evaporation. Second, the presence of lithium lowers the work function of the cathode from 4.5 eV to 2.1 eV when trace amounts of barium are added, further reducing the operation temperature [70].

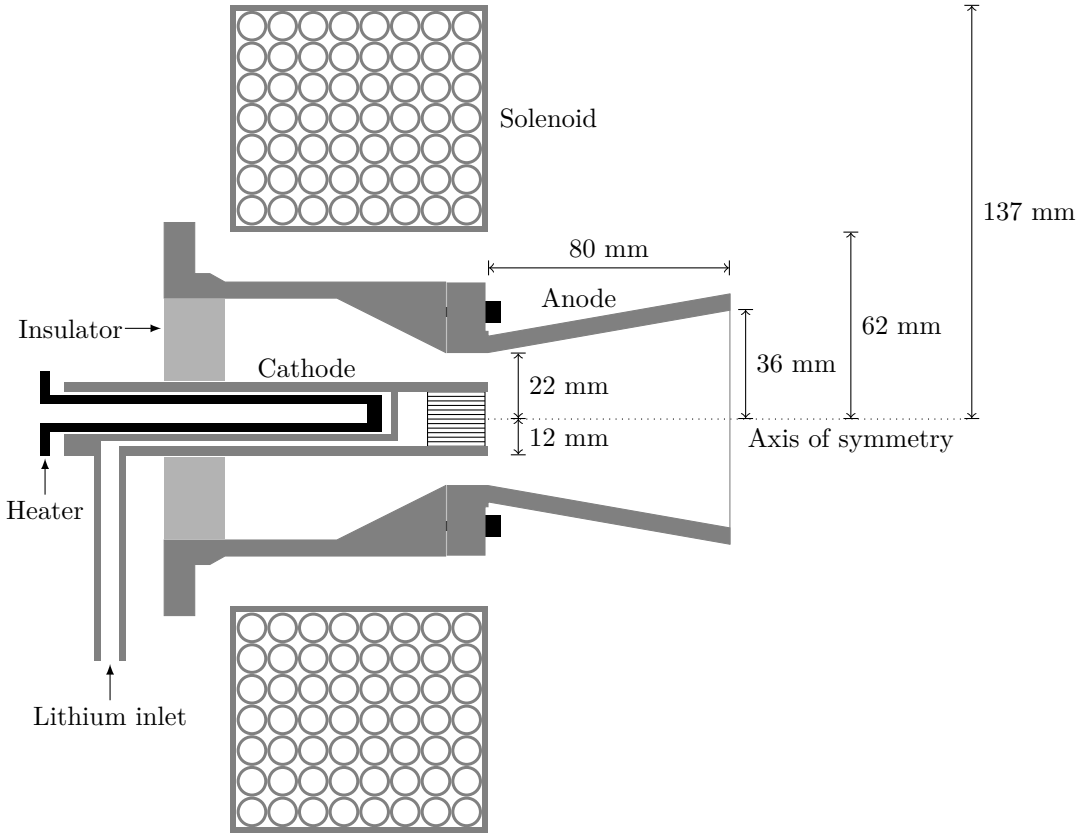


Figure C.4: Cross-section of the LiLFA.

MAI experiments with the LiLFA at 700 A using a barium additive showed the cathode to be 1,880 °C at steady state, compared to 2,000 °C using only lithium [70].

C.2.1 Lithium loading and cleaning procedures

Lithium is a highly reactive propellant, and as such, it presents a challenge in terms of maintaining propellant purity until time of firing. Further, it poses a significant safety hazard to the researcher. In order to prevent the contamination of lithium propellant due to reaction with the atmosphere, we handle the lithium in a glovebox (Fig. C.1) under argon pressure. We maintain the glovebox pressure at just over 1 atmosphere so that air cannot leak in. We cut a solid 116 g lithium ingot in half using a chisel, store one half in mineral oil, and load the remaining half into a reservoir.

We then close this reservoir (shown schematically in Fig. C.5) except for the argon inlet and lithium output tubes.

We place the reservoir into the antechamber of the glovebox, don fire resistant clothing, and then open the antechamber. We rapidly transfer the reservoir to the main vacuum chamber and connect an argon line to the inlet. Argon flows over the ingot while we pump the vacuum chamber down. We cease flowing argon when 100 mTorr is reached and continue pumping down until we reach our target background pressure.

After successfully firing the LiLFA, the inside of the vacuum chamber is coated in a thin layer of lithium. In order to simplify the cleanup procedure, the inside of the chamber is wrapped in aluminum foil prior to every firing. Because lithium reacts with air to form hydrogen (which is extremely flammable), we react the lithium with water before venting the chamber. We begin this procedure by turning off all vacuum pumps except for the roughing pump, closing the high vacuum valve, and venting 500 mL of water into the chamber. We wait 30 min for the water vapor to react, and then open the high vacuum valve. Using this procedure, we generate only small amounts of hydrogen at low pressure, and there is never a danger of hydrogen leaking into the laboratory. We repeat this procedure as many times as necessary to convert all the lithium to lithium hydroxide. Once complete, the tank can be safely vented to atmospheric pressure.

Lithium hydroxide poses additional risks. It is a carcinogen and forms a strongly basic solution when mixed with water. For this reason, prior to opening the main chamber door we attach a duct to one of the port windows with a fan to slightly reduce the chamber pressure. The fan exhausts outside the building. This limits the contamination of the surrounding laboratory area. We then enter the tank wearing Tyvek coveralls, a full face mask, and a self-contained breathing apparatus. The aluminum foil is removed from the interior of the chamber and disposed of. The feed

system and thruster are rinsed in a location where the resulting hydrogen is blown outside the building.

C.2.2 Lithium feed system

The lithium feed system uses a piston to displace a chamber of liquid lithium at a controlled rate, forcing the fluid into the thruster cathode. At present, the only dynamic seals (silicon and Viton[®]) that will survive repeated exposure to liquid lithium have a narrow margin of safety. It is similarly difficult to operate a mechanical valve with liquid lithium. The LiLFA feed system overcomes both of these obstacles by controlling the flow of lithium with a sequence of melting and freezing cycles.

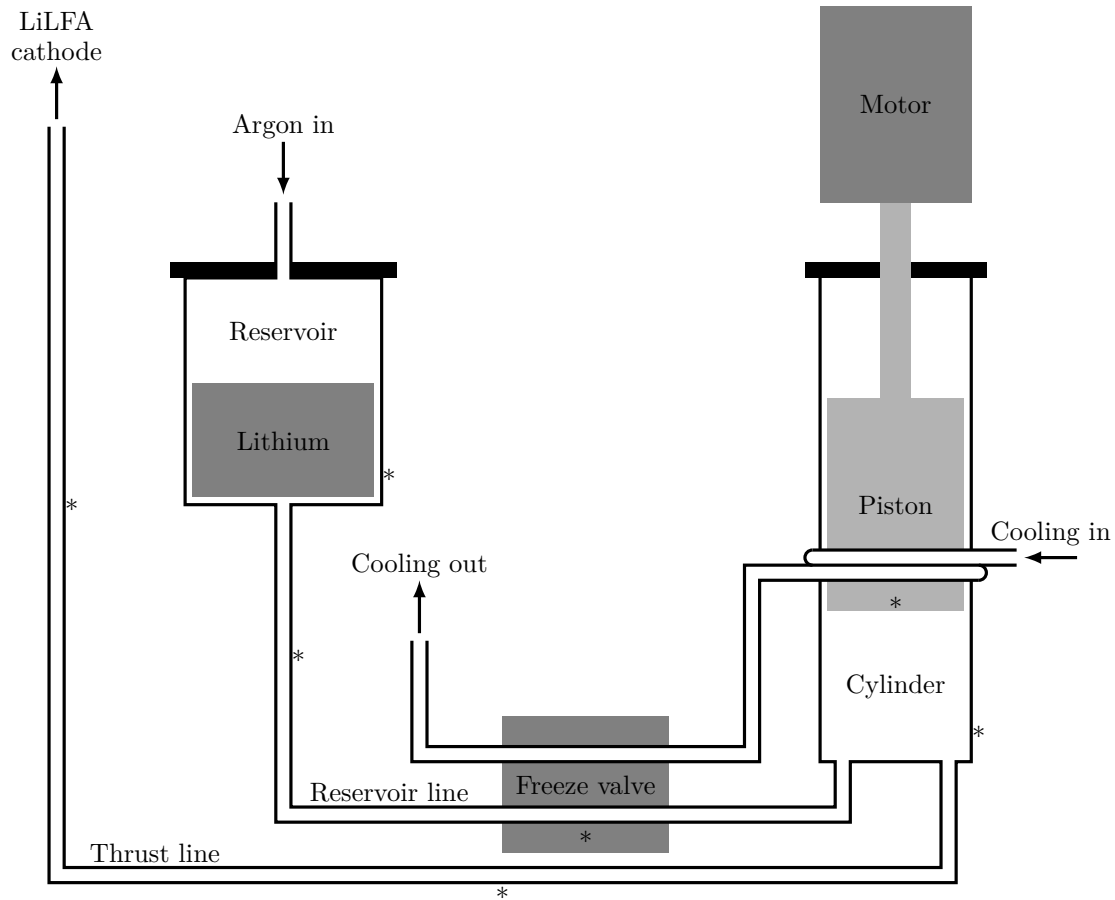


Figure C.5: Schematic of the lithium feed system. Thermocouple positions are indicated by the “*” symbol.

The lithium feed system is shown schematically in Fig. C.5. All surfaces in contact with lithium are stainless steel and can be heated via external band, cartridge, and coil heaters. Initially, a solid ingot of lithium is in the reservoir. We heat the reservoir, reservoir line, freeze valve, and cylinder and melt the lithium. Then, we apply a small amount of argon pressure through the argon inlet, which forces the lithium to flow into the cylinder. We turn off the reservoir, reservoir line, and freeze valve heaters, and turn on the thrust line heater. Then, the flow rate is increased in the cooling line. This increase causes the remaining lithium in the freeze valve to solidify. The piston is lowered slowly so that the rate of displacement corresponds to the desired mass flow rate. The freeze valve prevents the displaced lithium from flowing back to the reservoir and the cooling loop around the cylinder prevents lithium from leaking around the piston. Once lithium reaches the cathode, it is evaporated by the cathode heater (Fig. C.4).

The temperature of the lithium feed system is measured by 8 K-type thermocouples, 7 of which are marked in Fig. C.5. An additional thermocouple is positioned on the stem of the cathode. Using the temperature measurements, we are able to determine the phase and location of lithium at each location. A temperature plateau followed by a sudden increase indicates the lithium has melted. A sudden increase in temperature downstream of the reservoir when we are applying argon pressure indicates the lithium has reached that location. Similarly, a sudden increase in temperature of the thermocouple located inside the piston indicates the piston has reached the lithium surface inside the cylinder.

C.2.3 Power

Power is delivered to the LiLFA by a 30 kW Miller SRS-1000-C1 welding power supply. This supply has multiple output options. When configured for the LiLFA, it is limited to 80 V or 1000 A. The current is controlled using a remote turn dial and measured

using a Hall-effect sensor (see Sec. C.4.2). A 25:1 voltage divider is used to step down the voltage for measurement.

C.3 The argon Lorentz force accelerator

The argon Lorentz force accelerator (ALFA), pictured in Fig. C.6, was designed and constructed at Princeton University in 2017. Argon is a worse propellant than lithium in terms of thrust efficiency and thruster lifetime. It has a higher first ionization potential (15.8 eV compared to 5.4 eV for lithium), meaning more energy is spent on ionization instead of accelerating ions, and a lower second ionization potential (27.6 eV compared to 75.6 eV for lithium), meaning there are more frozen flow losses. While injecting lithium through a cathode reduces the cathode temperature and therefore the erosion rate, argon offers no such benefit. However, argon is nonhazardous, requires no cleanup, and its flow rate to a thruster is easy to control compared to the previously described method for pumping lithium. Because the scaling principles of thrust and voltage can be studied using any propellant, we elected to use the ALFA for the majority of our experimental work, since it allows for more frequent data acquisition.

The ALFA has similar dimensions to the LiLFA so that comparisons between the two can be easily made. However, it differs in that the electrodes are made from AXM-5Q POCO® graphite. Because we lack the temperature reducing benefits of lithium, we implemented an orificed hollow cathode, which contains a lanthanum hexaboride (LaB_6) emitter, which has a work function of 2.5 eV. The thruster is shown schematically in Fig. C.7. The anode is contoured to the shape of the applied magnetic field, since this has been shown to be beneficial for reducing the operating voltage and temperature [16, 10, 61].

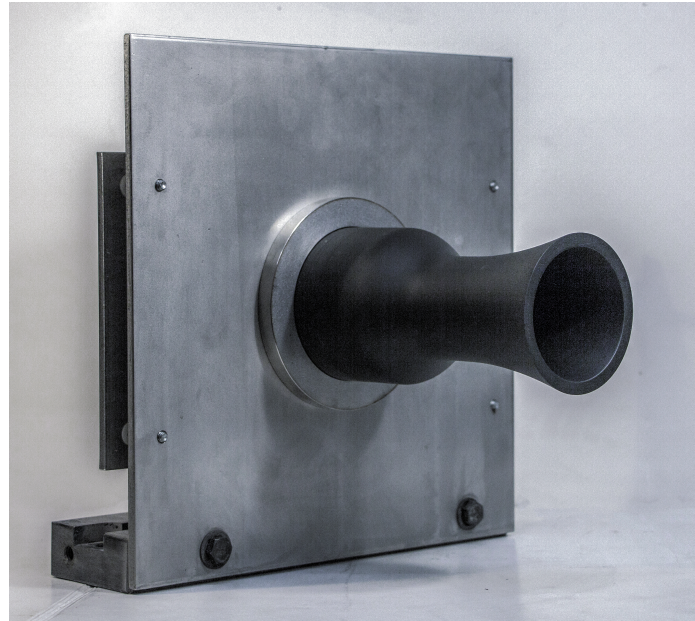


Figure C.6: Picture of the ALFA. A solenoid (not pictured) fits around the graphite nozzle and can be placed at different axial positions.

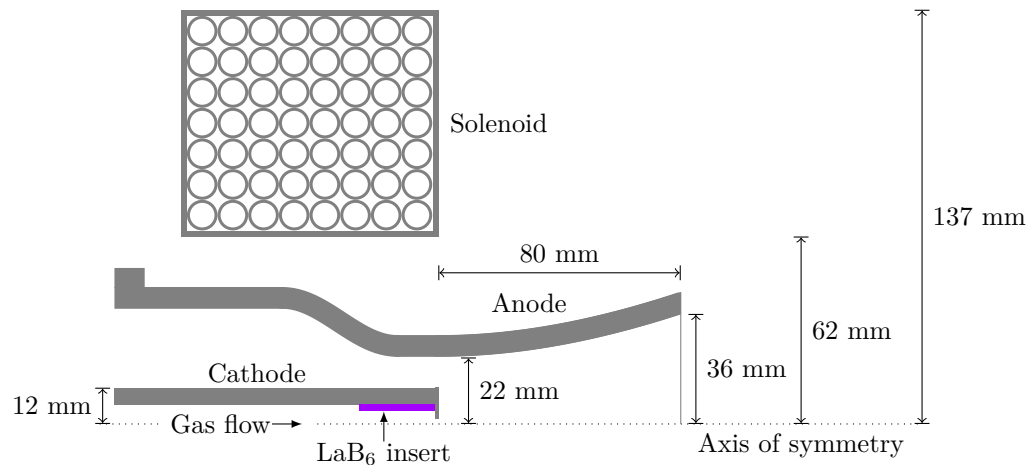


Figure C.7: Cross-section of the ALFA, which is symmetric about the thrust axis.

In this work, we will investigate the effects of the applied-field topology on thrust generation. To this end, we designed this thruster so that the solenoid could be placed at two different locations with respect to the anode exit plane. These are illustrated in Fig. C.8, and we will refer to the different configurations as contoured (a), where

the magnetic field follows the contour of the anode, and constricted (b), where the magnetic field diverges more slowly than the anode.

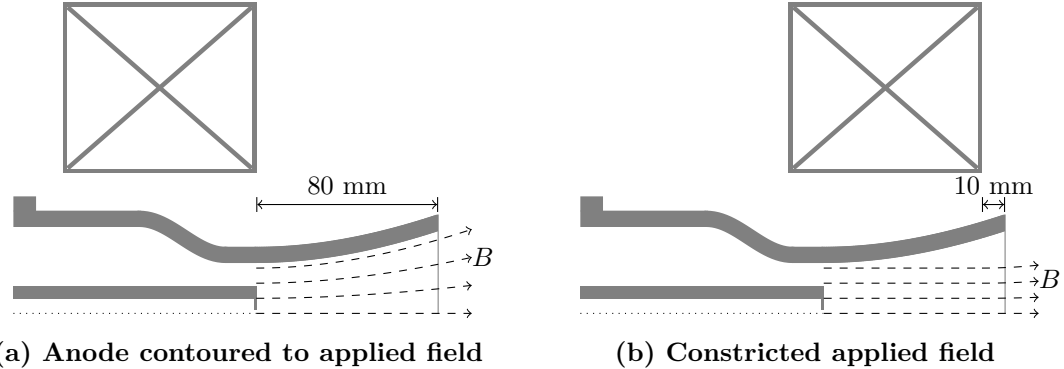


Figure C.8: Contoured (a) and constricted (b) configurations and the corresponding applied-field topologies.

C.3.1 Argon mass flow control system

In addition to the applied-field topology, we will investigate the effects of mass flow rate on thrust. We wish to consistently operate at one of two different mass flow rates, and so we designed the mass flow controller illustrated in Fig. C.9. The controller consists of two sonic orifices in parallel, each of which can be toggled on and off using a ball valve. When only the first is open, the mass flow rate is low, and when both are open, the mass flow rate is high. We kept the upstream pressure constant, at 10 psig, which resulted in mass flow rates of 2.5 and 5.3 mg/s for the two different configurations.

C.3.2 Power and ignition procedure

Power is delivered to the ALFA by the same 30 kW welding power supply used for the LiLFA. However, it is configured with a limit of 160 V or 500 A. Because there is no heater with which to make the LaB₆ begin emitting, the thruster is spark started. A Kepco ABC 1000M 1 kV power supply is used to charge a capacitor bank, which

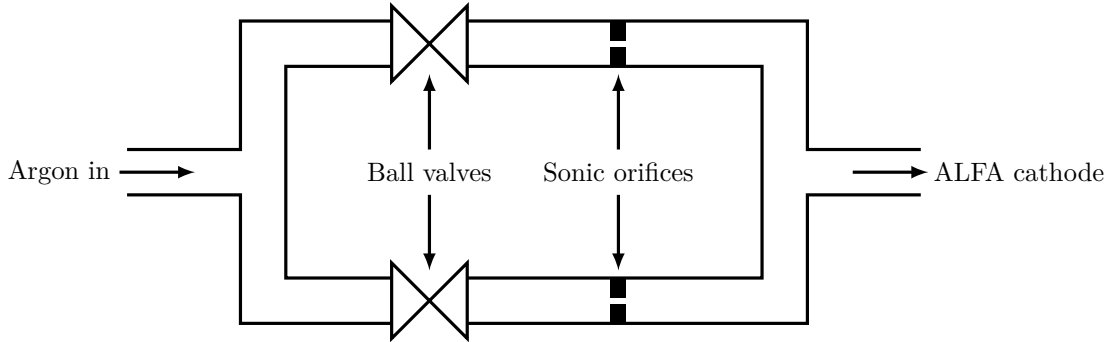


Figure C.9: Schematic of the ALFA mass flow controller.

is discharged across the thruster to begin current flow. Diodes are used to prevent reverse current flow through the welding supply. A detailed schematic is given in Fig. C.10. Once the thruster is sparked, the Miller is able to maintain a current for steady-state operation. The voltage in this setup is reduced for measurement by a 16:1 voltage divider with a limit on the maximum output voltage in order to protect the data acquisition system.

C.4 Diagnostics

C.4.1 Data acquisition system

A computer station records all output signals and controls the mass flow rate for the lithium feed system via a LabVIEW interface. The default sample rate was twice per second, except during thrust measurements, when the sample rate was increased to the maximum possible, up to 30 samples per second.

C.4.2 Current and magnetic field strength measurements

The current to the thruster, J , and to the solenoid, J_B , were each measured using an F. W. Bell® closed-loop Hall-effect sensor (model QB-1687) outside of the vacuum chamber. The magnetic strength, B_A , was measured using a Lake Shore Cryotronics®

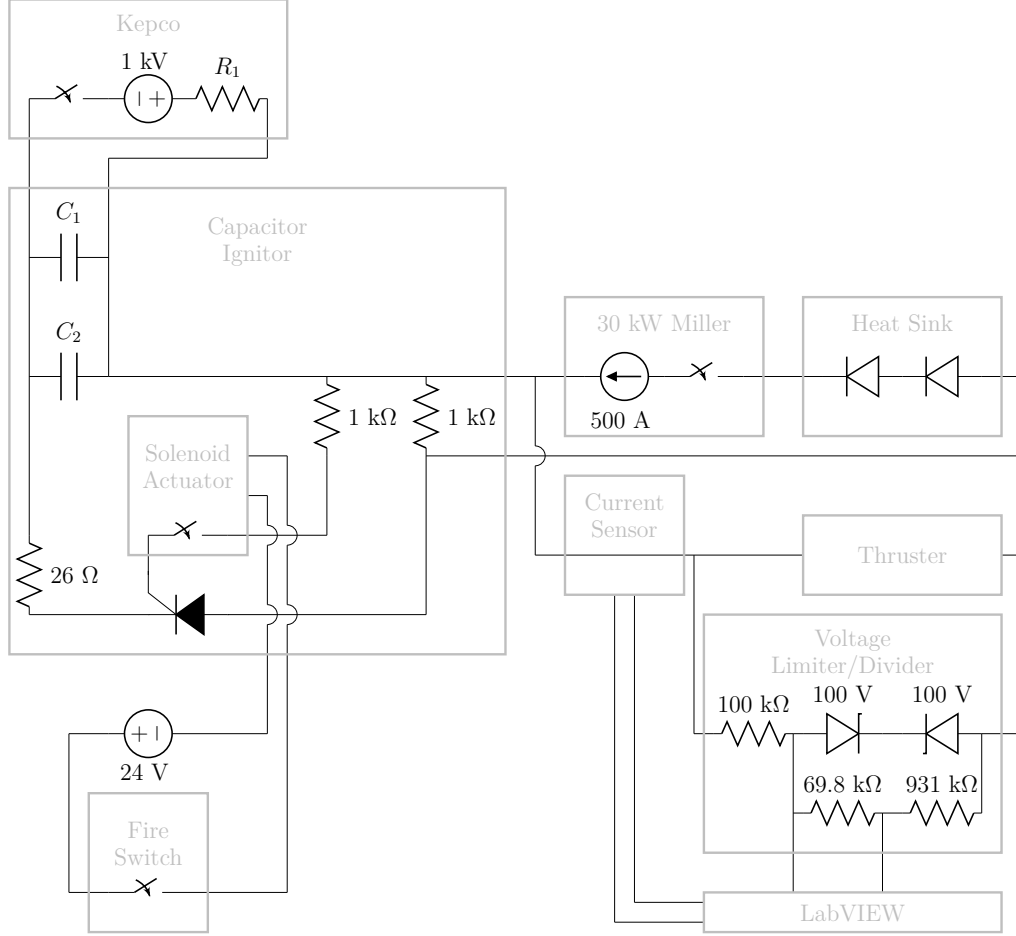


Figure C.10: Schematic of the power supply and sparking system for the ALFA.

model 425 gaussmeter as a function of J_B at the tip of the cathode, as well as at the anode exit plane, for the LiLFA. The results of this measurement are given in Fig. C.11. The magnetic field for all measurements is determined by the linear fit functions shown, with a slope of $3.14 \times 10^{-4}\ \text{T/A}$ at the tip of the cathode and $1.01 \times 10^{-4}\ \text{T/A}$ at the anode exit plane.

When operated in the contoured configuration, the magnetic field in the ALFA is assumed to be the same as that in the LiLFA since the geometries are nearly identical from the cathode tip outwards. When the ALFA is operated in the constricted configuration, we assume the magnetic field to be approximately constant, and equal to that found at the cathode tip in the contoured configuration.

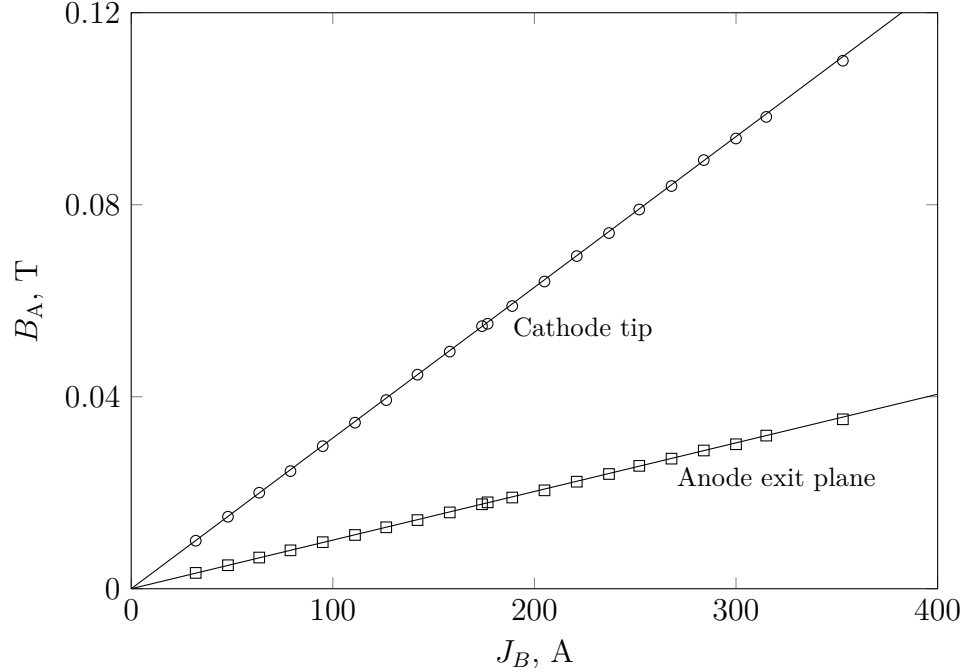


Figure C.11: Magnetic field strength at the cathode tip and anode exit plane as a function of current to the solenoid for the ALFA in the contoured configuration and for the LiLFA.

C.4.3 Argon mass flow and background pressure measurements

The mass flow rate is recorded using an OMEGA® FMA-A2404 flow meter, which is accurate to within 4% using argon. The background pressure is measured using an MKS 943 cold cathode vacuum gauge system, which is located in the top of the vacuum chamber approximately 2 m downstream of the thruster. Thrust measurements are only considered valid if the background pressure, p_b , is maintained at under 3×10^{-4} Torr, since pressures above this threshold have been shown to affect both thrust and thruster voltage [51].

Appendix D

Gasdynamic Thrust Component Contribution

Our observation of increasing C_T with increasing \bar{f} for a given mass flow rate and applied-field strength is equivalent to C_T decreasing with increasing J . This behavior would also be observed if we had underpredicted the gasdynamic thrust. In order to make sure the observed trends are not due to our assumption that $k_{GD} = 1$, we repeat our analysis with $k_{GD} = 1.6$ in Figs. D.1, D.2, and D.3. We observe the same trends, although they are less pronounced in these figures. Further, we observe that in the case of the Alta data (Fig D.3), there are negative C_T values for the data taken at 120 mg/s, indicating that $k_{GD} = 1.6$ overpredicts the gasdynamic thrust for this thruster.

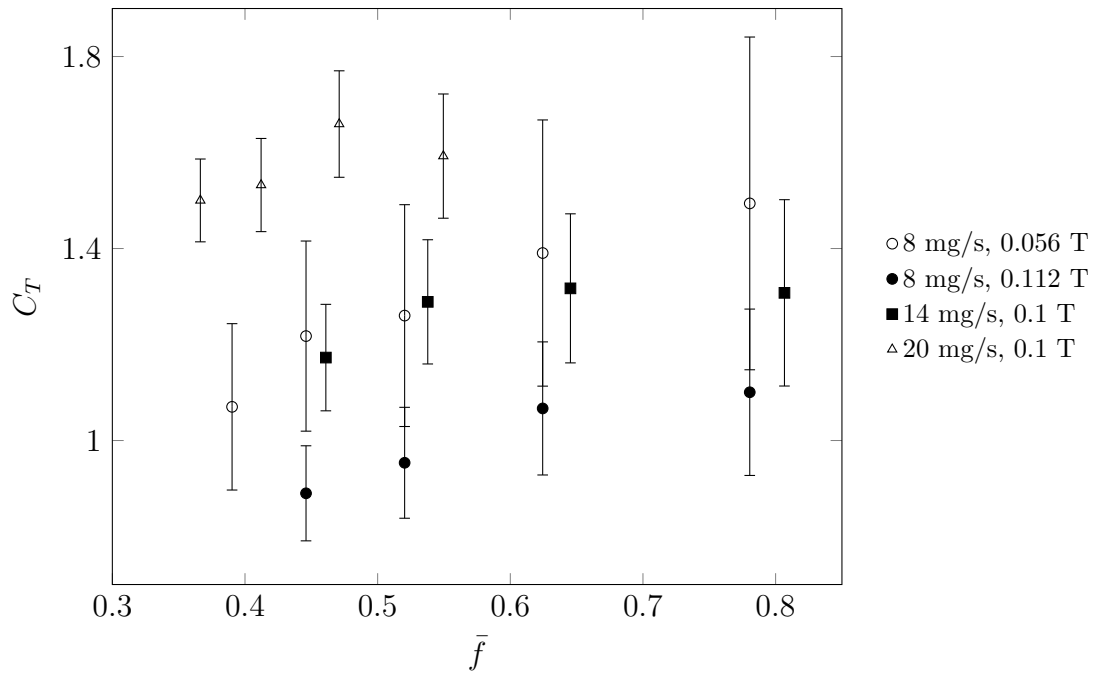


Figure D.1: C_T as a function of \bar{f} for the 30 kW MAI lithium thruster where C_T is calculated using the highest estimate in the literature for gasdynamic thrust ($k_{GD} = 1.6$).

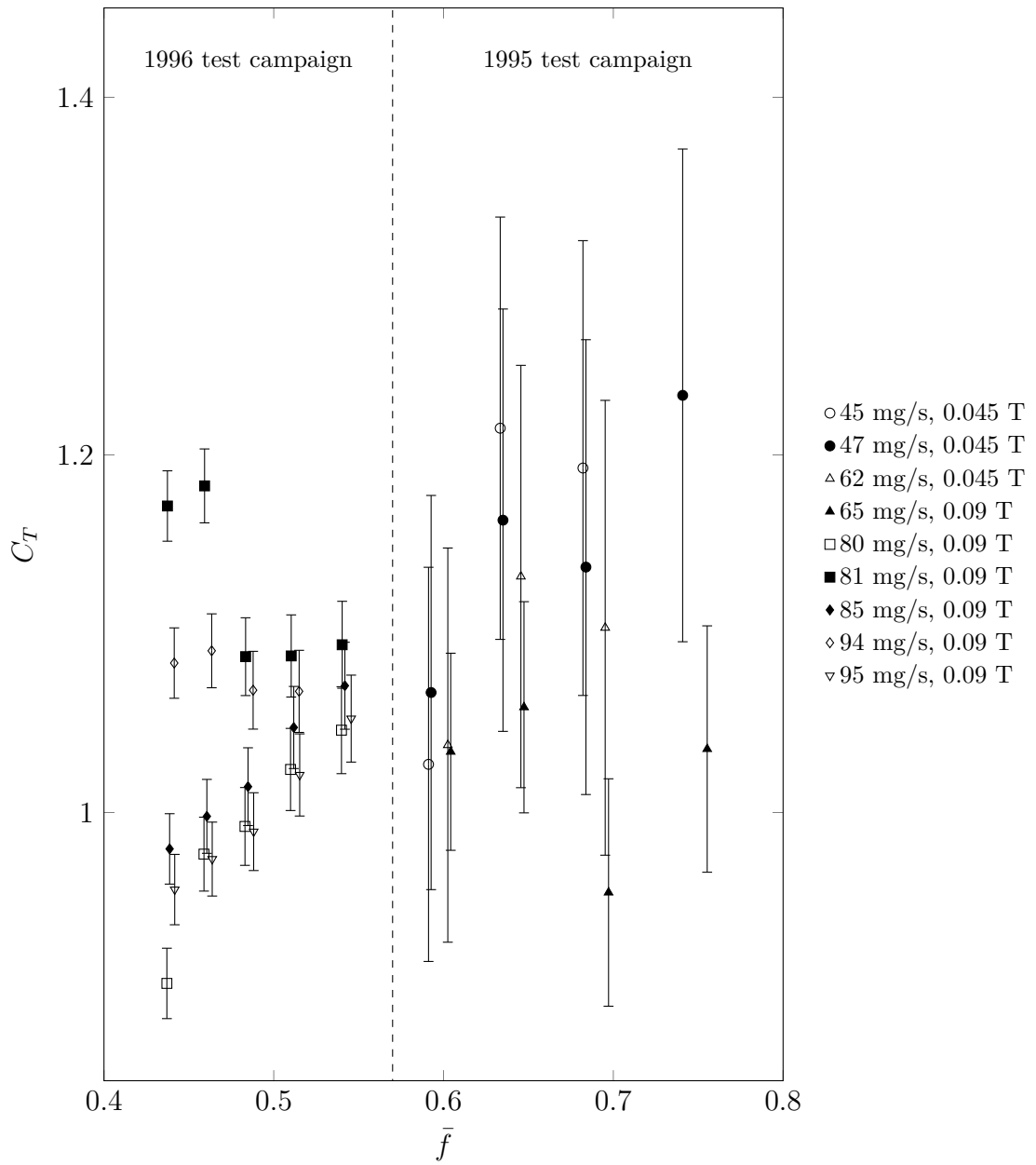


Figure D.2: C_T as a function of \bar{f} for the 150 kW MAI lithium thruster where C_T is calculated using the highest estimate in the literature for gasdynamic thrust ($k_{GD} = 1.6$).

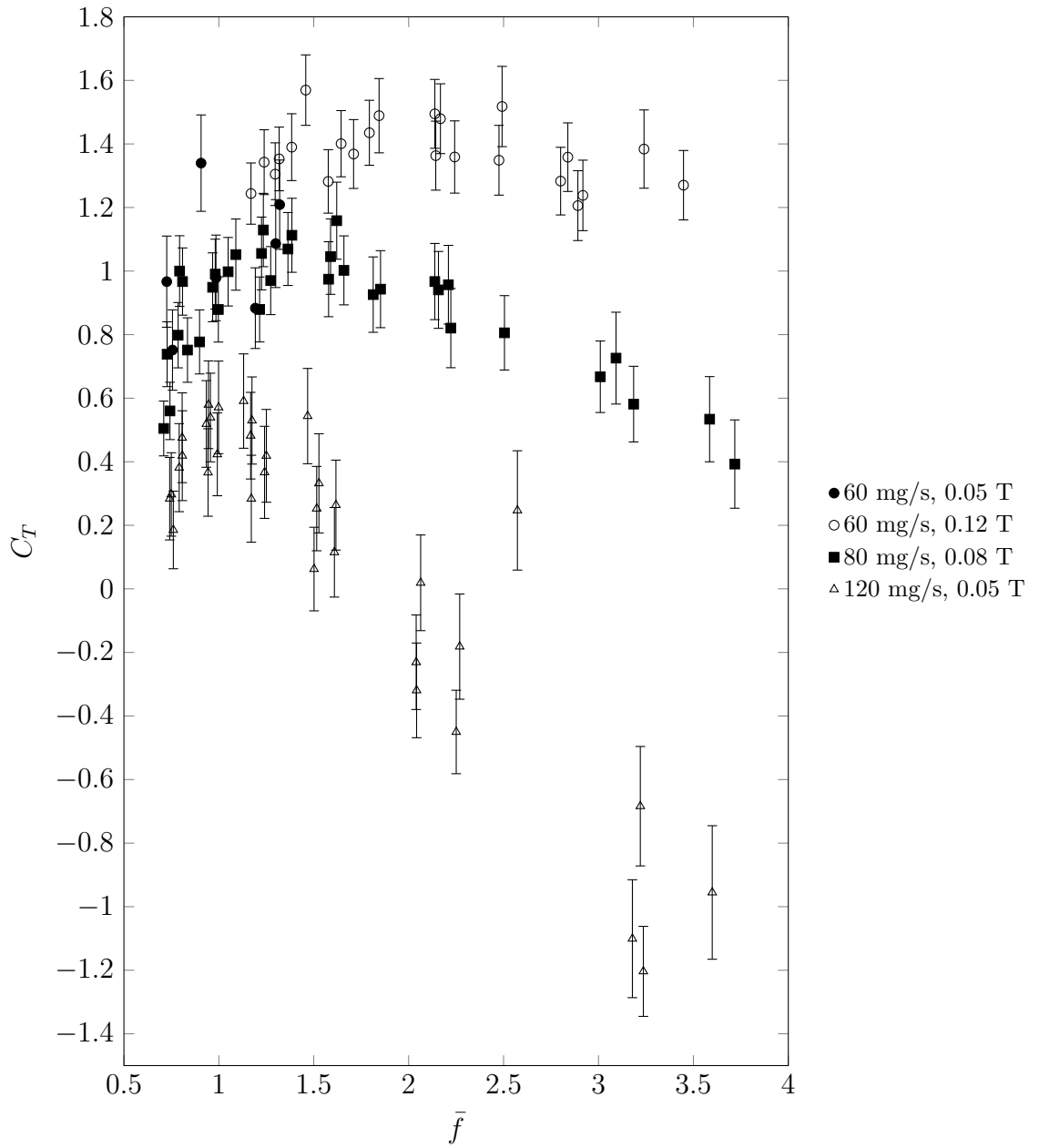


Figure D.3: C_T as a function of \bar{f} for the 200 kW Alta argon thruster where C_T is calculated using the highest estimate in the literature for gasdynamic thrust ($k_{GD} = 1.6$).

Bibliography

- [1] G. Kruelle. Characteristics and local analysis of MPD thruster operation. In *AIAA Electric Propulsion and Plasmadynamics Conference*, AIAA-67-672, Colorado Springs, CO, Sept. 11–13, 1967. doi:10.2514/6.1967-672.
- [2] M. Andrenucci. *Encyclopedia of Aerospace Engineering: Magnetoplasmodynamic Thrusters*, chapter 2.4.04. Wiley Online Library, 2010. doi:10.1002/9780470686652.eae118.
- [3] K. Sankaran, L. Cassady, A. D. Kodys, and E. Y. Choueiri. A survey of propulsion options for cargo and piloted missions to Mars. In *International Conference on New Trends in Astrodynamics*, College Park, MD, Jan. 20–22, 2003.
- [4] J. Polk. Lithium-fuelled electromagnetic thrusters for robotic and human exploration missions. In *Space Nuclear Conference*, San Diego, CA, June7, 2005.
- [5] D. Brown, B. Beal, and J. Haas. Air Force Research Laboratory high power electric propulsion technology development. Technical report, IEEEAC, 2009.
- [6] E. Musk. Spacex interplanetary transport system. 2016. URL: <http://www.spacex.com/mars>.
- [7] W. J. Coogan. AF-MPDT database. URL: <http://alfven.princeton.edu/tools/afmpdt-database>.
- [8] D. B. Fradkin, A. W. Blackstock, D. J. Roehling, T. F. Stratton, M. Williams, and K. W. Liewer. Experiments using a 25 kW hollow cathode lithium vapor MPD arcjet. In *AIAA 7th Electric Propulsion Conference*, AIAA-69-2417, Williamsburg, VA, Mar. 3–5, 1969. doi:10.2514/6.1969-241.
- [9] R. M. Myers. Scaling of 100 kW class applied-field MPD thrusters. In *28th Joint Propulsion Conference and Exhibit*, AIAA-92-3462, Nashville, TN, July 6–8, 1992.
- [10] V. B. Tikhonov, S. A. Semenikhin, V. A. Alexandrov, and G. A. Popov. Research of plasma acceleration processes in self-field and applied magnetic field thrusters. In *23rd International Electric Propulsion Conference*, IEPC-93-076, Seattle, WA, Sept. 13–16, 1993.

- [11] A. Sasoh and Y. Arakawa. Thrust formula for applied-field magnetoplasmodynamic thrusters derived from energy conservation equation. *Journal of Propulsion and Power*, 11(2):351–356, 1995. doi:10.2514/3.51432.
- [12] P. G. Mikellides and P. J. Turchi. Applied-field magnetoplasmodynamic thrusters, part 2: Analytic expressions for thrust and voltage. *Journal of Propulsion and Power*, 16(5):894–901, 2000. doi:10.2514/2.5657.
- [13] M. Coletti. A thrust formula for an MPD thruster with applied-magnetic field. *Acta Astronautica*, 81:667–674, 2012. doi:10.1016/j.actaastro.2012.08.014.
- [14] G. Herdrich, A. Boxberger, D. Petkow, R. A. Gabrielli, S. Fasoulas, M. Andrenucci, R. Albertoni, F. Paganucci, and P. Rosetti. Advanced scaling model for simplified thrust and power scaling of an applied-field magnetoplasmodynamic thruster. In *46th AIAA/ASME/SAE/ASEE Joint Propulsion Conference*, AIAA-2010-6531, Nashville, TN, July 25–28, 2010. doi:10.2514/6.2010-6531.
- [15] R. Albertoni, F. Paganucci, and M. Andrenucci. A phenomenological model for applied-field MPD thrusters. *Acta Astronautica*, 107:177–186, 2015. doi:10.1016/j.actaastro.2014.11.017.
- [16] V. Tikhonov, S. Semenikhin, J. R. Brophy, and J. E. Polk. The experimental performances of the 100 kW Li MPD thruster with external magnetic field. In *24th International Electric Propulsion Conference*, IEPC-95-105, Moscow, Russia, Sept. 19–23, 1995.
- [17] G. Popov, V. Kim, T. Tikhonov, S. Semenikhin, and M. Tibrina. The third quarterly report on the stages ## 5-6 of the contract on the research studies no. NASA-4851 between RIAME MAI and NASA. Technical Report NASW-4851, RIAME MAI, June 1995.
- [18] E. Y. Choueiri. Scaling of thrust in self-field magnetoplasmodynamic thrusters. *Journal of Propulsion and Power*, 14(5):744–753, 1998. doi:10.2514/2.5337.
- [19] D. Lev. *Investigation of Efficiency in Applied Field MagnetoPlasmaDynamic Thrusters*. PhD thesis, Princeton University, Jan. 2012.
- [20] W. J. Coogan and E. Y. Choueiri. A critical review of thrust models for applied-field magnetoplasmodynamic thrusters. In *AIAA Propulsion and Energy 2017*, AIAA-2017-4723, Atlanta, GA, July 10–12, 2017. doi:10.2514/6.2017-4723.
- [21] A. G. Popov and S. A. Semenikhin. Calculation of thrust for the end-Hall effect rocket. In *7th Soviet Conference for Plasma Rockets and Ion Injectors (in Russian)*, pp. 202-203, Kharkiv, Ukraine, Sept. 26–28, 1989.
- [22] H. V. Belan, V. P. Kim, A. E. Oranksky, and V. B. Tikhonov. *Stationary Plasma Engines (in Russian)*, chapter 5, pages 125–131. Kharkiv Aviation Institute, Kharkiv, Ukraine, 1989.

- [23] V. B. Tikhonov, S. A. Semenikhin, J. R. Brophy, and J. E. Polk. Performance of 130 kW MPD thruster with an external magnetic field and Li as a propellant. In *25th International Electric Propulsion Conference*, IEPC-97-117, Cleveland, OH, Aug. 24–28, 1997.
- [24] V. Kim, T. Tikhonov, and S. Semenikhin. The second quarterly report on the stages ##2A, B of the contract on the research studies no. NASW-4851 between RIAME MAI and NASA. Technical Report NASW-4851, RIAME MAI, July 1996.
- [25] V. Kim, T. Tikhonov, and S. Semenikhin. The fourth quarterly (final) report on the stage ## 3 “C”, “D” of the contract on the research studies no. NASW-4851 between RIAME MAI and NASA. Technical Report NASW-4851, RIAME MAI, Apr. 1997.
- [26] H. Tang, J. Cheng, C. Liu, and T. M. York. Study of applied magnetic field magnetoplasmadynamic thrusters with particle-in-cell and Monte Carlo collision. ii. investigation of acceleration mechanisms. *Physics of Plasmas*, 19(073108), 2012. doi:10.1063/1.4737104.
- [27] H. Tahara, Y. Kagaya, and T. Yoshikawa. Effects of applied magnetic fields on performance of a quasisteady magnetoplasmadynamic arcjet. *Journal of Propulsion and Power*, 11(2):337–342, 1995. doi:10.2514/3.51430.
- [28] H. Tahara, Y. Kagaya, and T. Yoshikawa. Performance and acceleration process of quasisteady magnetoplasmadynamic arcjets with applied magnetic fields. *Journal of Propulsion and Power*, 13(5):651–658, 1997. doi:10.2514/2.5216.
- [29] R. M. Myers, M. Mantenieks, and J. Sovey. Geometric effects in applied-field MPD thrusters. In *21st International Electric Propulsion Conference*, AIAA-90-2669, Cleveland, OH, July 18–10, 1990.
- [30] R. R. John and S. Bennett. Final report: Arcjet technology research and development. Technical Report NASA CR-54687/RAD-TR-65-37, AVCO Corporation, NASA Contract NAS 3-5900, Dec. 1965.
- [31] S. Bennett, G. Enos, R. John, and W. Powers. Final report: Magnetoplasmadynamic thrust research. Technical Report NASA CR-72345/AVSSD-0272-67-RR, AVCO Missiles, Space, and Electronics Group, NASA Contract NAS 3-8907, May 1967.
- [32] J. D. Huba. *NRL Plasma Formulary*, page 28. Naval Research Laboratory, Washington, D.C., 2016.
- [33] R. M. Myers, A. J. Kelly, and R. G. Jahn. Energy deposition in low-power coaxial plasma thrusters. *Journal of Propulsion*, 7(5):732–739, 1991. doi:10.2514/3.23386.

- [34] G. Serianni, N. Vianello, F. Paganucci, and P. Rossetti. Plasma diagnostics in an applied field MPD thruster. In *27th International Electric Propulsion Conference*, IEPC-2001-135, Pasadena, CA, Oct. 15–19, 2001.
- [35] V. B. Montgomery and J. Terrell. Some useful information for the design of air-core solenoids. Technical Report AF 19 (604)-7344, Solid State Sciences Division, Air Force Office of Scientific Research (OAR), Dec. 1961.
- [36] A. V. Arefiev and B. N. Breizman. Magnetohydrodynamic scenario of plasma detachment in a magnetic nozzle. *Physics of Plasmas*, 12(043504), 2005. doi: 10.1063/1.1875632.
- [37] J. M. Little and E. Y. Choueiri. Divergence of a propulsive plasma flow expanding through a magnetic nozzle. In *31st International Electric Propulsion Conference*, IEPC-2009-260, Ann Arbor, MI, Sept. 20–24, 2009.
- [38] E. Ahedo and M. Merino. On plasma detachment in propulsive magnetic nozzles. *Physics of Plasmas*, 18(053504), 2011. doi:10.1063/1.3589268.
- [39] H. Maecker. Plasmaströmungen in lichtbögen infolge eigenmagnetischer kompression (plasma jets in arcs in a process of self-induced magnetic compression). *Zeitschrift für Physik*, 141(1):198–216, 1955.
- [40] R. G. Jahn. *Physics of Electric Propulsion*, chapter 8, pages 240–244. Dover Publications, Inc., Mineola, NY, 1968.
- [41] J. Gilland and G. Johnston. MPD thruster performance analytic models. In *Space Technology and Applications International Forum*, Albuquerque, NM, Feb. 2–5, 2003.
- [42] L. K. Rudolph. *The MPD Thruster Onset Current Performance Limitation*. PhD thesis, Princeton University, Sept. 1980.
- [43] V. Kim, T. Tikhonov, and S. Semenikhin. The second quarterly report on the stages ## 3-4 of the contract on the research studies no. NASA-4851 between RIAME MAI and NASA. Technical Report NASW-4851, RIAME MAI, Jan. 1995.
- [44] P. J. Turchi. *The Cathode Region of a Quasi-Steady Magnetoplasmadynamic Arcjet*. PhD thesis, Princeton University, Sept. 1970.
- [45] A. P. Bruckner and R. G. Jahn. Spectroscopic studies of the exhaust plume of a quasi-steady MPD accelerator. Technical Report 1041, NASA Research Grant NGL 31-001-005, 1972.
- [46] H. Tobari, A. Ando, M. Inutake, and K. Hattori. Characteristics of electromagnetically accelerated plasma flow in an externally applied magnetic field. *Physics of Plasmas*, 14(093507), 2007. doi:10.1063/1.2773701.

- [47] D. Ichihara, T. Uno, H. Kataoka, J. Jeong, A. Iwakawa, and A. Sasoh. Ten-ampere-level, applied-field-dominant operation in magnetoplasmadynamic thrusters. *Journal of Propulsion and Power*, 33(2):360–369, 2017. doi:10.2514/1.B36179.
- [48] S. Yokota, D. Ichihara, H. Kataoka, S. Harada, and A. Sasoh. Steady-state, applied-field, rectangular MPD thrusters. In *33rd International Electric Propulsion Conference*, IEPC-2013-246, Washington, D.C., Oct. 6–10, 2013.
- [49] F. Paganucci, P. Rossetti, M. Andrenucci, V. B. Tikhonov, and V. A. Obukhov. Performance of an applied field MPD thruster with a pre-ionization chamber. In *33rd Plasmadynamics and Lasers Conference*, AIAA-2002-2103, Maui, HI, May 20–23, 1964. doi:10.2514/6.2002-2103.
- [50] N. Koyama, T. Suzuki, T. Kubota, and H. Tahara. Performance characteristics of steady-state MPD thrusters with permanent magnets and multi hollow cathodes for in-space propulsion. In *33rd International Electric Propulsion Conference*, IEPC-2013-094, Washington, D.C., Oct. 6–10, 2013.
- [51] J. S. Sovey and M. A. Mantenieks. Performance and lifetime assessment of magnetoplasmadynamic arc thruster technology. *Journal of Propulsion*, 7(1):71–83, 1991. doi:10.2514/3.23296.
- [52] R. M. Myers. Applied-field MPD thruster geometry effects. Technical Report NASA CR-187163/AIAA-91-2342, Sverdum Technology, Inc., Lewis Research Center Group, NASA Contractor Report 187163, Aug. 1991.
- [53] H. Kurtz. *Integrale Messungen an einem Axialsymmetrischen Elektronmagnetischen Plasmabeschleuniger (Triebwerksmodell X-13) (Integral Measurements on an Axial-symmetric Electromagnetic Plasma Thruster (Model X-13))*. PhD thesis, Deutsche Forschungs und Versuchsanstalt für Luft und Raumfahrt, Aug. 1971.
- [54] R. E. Jones. Results of large vacuum facility tests of an MPD arc thruster. *AIAA Journal*, 4(8):1455–1456, 1966. doi:10.2514/3.3705.
- [55] G. Krülle and E. Zeyfang. Preliminary conclusions of continuous applied field electromagnetic thruster research at DFVLR. In *AIAA 11th Electric Propulsion Conference*, AIAA-75-417, New Orleans, LA, Mar. 19–21, 1975. doi:10.2514/6.1975-417.
- [56] G. L. Cann, R. A. Moore, R. L. Harder, and P. F. Jacobs. High specific impulse thermal arcjet thruster technology part II: Performance of Hall arc jets with lithium propellant. Technical Report AFAPL-TR-65-48, Part II, Electro-Optical Systems, Inc., Jan. 1967.
- [57] G. L. Cann, R. L. Harder, and R. A. Moore. Hall current accelerator. Technical Report NASA CR-54705/EOS 5470-Final, Electro-Optical Systems, Inc., Feb. 1966.

- [58] A. D. Kodys and E. Y. Choueiri. A critical review of the state-of-the-art in the performance of applied-field magnetoplasmadynamic thrusters. In *41st AIAA/ASME/SAE/ASEE Joint Propulsion Conference and Exhibit*, AIAA-2005-4247, Tucson, AZ, July 11–13, 2005. doi:10.2514/6.2005-4247.
- [59] G. Krülle, M. Auweter-Kurtz, and A. Sasoh. Technology and application aspects of applied field magnetoplasmadynamic propulsion. *Journal of Propulsion*, 14(5):754–763, 1998. doi:10.2514/2.5338.
- [60] D. R. Lev and E. Y. Choueiri. Scaling of efficiency with applied magnetic field in magnetoplasmadynamic thrusters. *Journal of Propulsion and Power*, 28(3):609–616, 2012. doi:10.2514/1.B34194.
- [61] H. Tahara, H. Yasui, Y. Kagaya, and T. Yoshikawa. Development of a quasi-steady MPD arcjet thruster for near-earth missions. In *19th AIAA/DGLR/JSASS International Electric Propulsion Conference*, AIAA-87-1001, Colorado Springs, CO, Mar. 11–13, 1987. doi:10.2514/6.1987-1001.
- [62] G. I. Barenblatt. *Scaling, Self-Similarity and Intermediate Asymptotics*, chapter 1, pages 28–63. Cambridge University Press, New York, NY, 1996.
- [63] A. Akira, A. Masashi, S. Yukiko, I. Masaaki, H. Kunihiko, Y. Mikirou, I. Atsushi, T. Hiroyuki, and Y. Tsuyoshi. Spectroscopic studies of a high mach-number rotating plasma flow. *J. Plasma Fusion Res.*, 4:373–378, 2001.
- [64] R. M. Myers. Plume characteristics of MPD thrusters: A preliminary examination. Technical Report AIAA-89-2832, NASA Contractor Report 185130, 1989.
- [65] J. M. Little and E. Y. Choueiri. Thrust and efficiency model for electron-driven magnetic nozzles. *Physics of Plasmas*, 20(103501), 2013. doi:10.1063/1.4824613.
- [66] R. Albertoni, P. Rossetti, F. Paganucci, M. Andrenucci, M. Zuin, E. Martinez, and R. Cavazzana. Experimental study of a 100-kW class applied-field MPD thruster. In *32nd International Electric Propulsion Conference*, IEPC-2011-110, Wiesbaden, Germany, Sept. 11–15, 2011.
- [67] R. Albertoni, F. Paganucci, P. Rossetti, and M. Andrenucci. Experimental study of a hundred-kilowatt-class applied-field magnetoplasmadynamic thruster. *Journal of Propulsion and Power*, 29(5):1138–1145, 2013. doi:10.2514/1.B34688.
- [68] R. Albertoni. Personal Correspondence, Oct. 9, 2016.
- [69] V. Kim, T. Tikhonov, and S. Semenikhin. The first quarterly report on the stage ## 3 A of the contract on the research studies no. NASW-4851 between RIAME MAI and NASA. Technical Report NASW-4851, RIAME MAI, Apr. 1996.

- [70] G. Popov, V. Kim, T. Tikhonov, S. Semenikhin, and M. Tibrina. The fourth (final) quarterly report on the milestones (a) (4) and (a) (5) (D) of SoW of contract no. 960938 between RIAME MAI and JPL. Technical Report 960938, RIAME MAI, Dec. 1998.
- [71] W. J. Coogan and E. Y. Choueiri. A method for measuring the applied-field thrust component of plasma thrusters. *Journal of Propulsion and Power*, 2018. Accepted for Publication.
- [72] W. J. Coogan, M. A. Hepler, and E. Y. Choueiri. Measurement of the applied-field component of the thrust of a lithium Lorentz force accelerator. In *52nd AIAA/SAE/ASEE Joint Propulsion Conference*, AIAA-2016-4537, Salt Lake City, UT, July 25–27, 2016. doi:10.2514/6.2016-4537.
- [73] W. J. Coogan and E. Y. Choueiri. Applied-field topology effects on the thrust of an MPDT. In *35th International Electric Propulsion Conference*, IEPC-2017-182, Atlanta, GA, Oct. 8–12, 2017.
- [74] K. Takahashi, T. Lafleur, C. Charles, P. Alexander, and R. W. Boswell. Axial force imparted by a current-free magnetically expanding plasma. *Physics of Plasmas*, 19(083509), 2012. doi:10.1063/1.4747701.
- [75] T. W. Haag. Design of a thrust stand for high power electric propulsion devices. In *25th Joint Propulsion Conference*, AIAA-89-2829, Monterey, CA, July 10–12, 1989. doi:10.2514/6.1989-2829.
- [76] D. B. Fradkin and D. J. Roehling. Thrust stand performance measurements of a lithium fueled applied field MPD arcjet. In *13th Symposium on the Engineering Aspects of Magnetohydrodynamics*, Stanford, CA, Mar. 26–28, 1973.
- [77] D. B. Fradkin and D. J. Roehling. Experiments in the new LASL MPD arcjet test facility. Technical Report LA-5199-MS, Los Alamos, Feb. 1973.
- [78] R. A. Moore, G. L. Cann, and L. R. Gallagher. High specific impulse thermal arcjet thrustor technology part I: Performance of Hall arc jets with lithium propellant. Technical Report AFAPL-TR-65-48, Part I, Electro-Optical Systems, Inc., June 1965.
- [79] G. L. Cann, R. A. Moore, P. F. Jacobs, and L. R. Gallagher. High specific impulse thermal arcjet thrustor technology. Technical Report AFAPL-TR-65, Electro-Optical Systems, Inc., Sept. 1965.
- [80] W. Grossman Jr., R. V. Hess, and H. A. Hassan. Experiments with a coaxial Hall current plasma accelerator. *AIAA Journal*, 3(6):1034–1039, 1965. doi:10.2514/3.3050.
- [81] W. Grossman Jr., R. V. Hess, and H. A. Hassan. Experiments with a co-axial Hall current plasma accelerator. In *AIAA 4th Electric Propulsion Conference*, AIAA-64-700, Philadelphia, PA, Aug. 31–Sept. 2, 1964. doi:10.2514/6.1964-700.

- [82] M. A. Mantenieks, J. S. Sovey, R. M. Myers, T. W. Haag, P. Raitano, and J. E. Parkes. Performance of a 100 kW class applied field MPD thruster. In *25th Joint Propulsion Conference*, AIAA-89-2710, Monterey, CA, July 10–12, 1989. doi:10.2514/6.1989-2710.
- [83] R. M. Myers. Electromagnetic effects in an applied-field magnetoplasmadynamic thruster. *Journal of Propulsion and Power*, 11(2):343–350, 1995. doi:10.2514/3.51431.
- [84] R. M. Myers. Applied-field MPD thruster performance with hydrogen and argon propellants. *Journal of Propulsion and Power*, 9(5):781–784, 1993. doi:10.2514/3.23691.
- [85] P. G. Mikellides, P. J. Turchi, and N. F. Roderick. Applied-field magnetoplasmadynamic thrusters, part 1: Numerical simulations using the MACH2 code. *Journal of Propulsion and Power*, 16(5):887–893, 2000. doi:10.2514/2.5656.
- [86] V. B. Tikhonov, S. A. Semenikhin, and J. E. Polk. Own magnetic field impact on MPD thrusters performance with external magnetic field. In *26th International Electric Propulsion Conference*, IEPC-99-176, Kitakyushu, Japan, Oct. 17–21, 1999.
- [87] H. Tahara, Y. Kagaya, and T. Yoshikawa. Hybrid MPD thruster with axial and cusp magnetic fields. In *20th International Electric Propulsion Conference*, IEPC-1988-058, Garmisch-Partenkirchen, West Germany, Oct. 3–6, 1988.
- [88] H. Tahara, F. Takiguchi, Y. Kagaya, and T. Yoshikawa. Performance characteristics and discharge features of a quasi-steady applied-field MPD arcjet. In *22nd International Electric Propulsion Conference*, IEPC-1991-073, Viareggio, Italy, Oct. 14–17, 1991.
- [89] D. Ichihara. Personal Correspondence, Jan. 6, 2017.
- [90] A. Sasoh and Y. Arakawa. Electromagnetic effects in an applied-field magnetoplasmadynamic thruster. *Journal of Propulsion and Power*, 8(1):98–102, 1992. doi:10.2514/3.23448.
- [91] A. Sasoh, A. E. Solem, and Y. Arakawa. Optimization of current distribution in an applied-field MPD thruster. In *20th International Electric Propulsion Conference*, IEPC-1988-057, Garmisch-Partenkirchen, West Germany, Oct. 3–6, 1988.
- [92] A. Boxberger and G. Herdrich. Integral measurements of 100 kW class steady state applied-field magnetoplasmadynamic thruster SX3 and perspectives of AF-MPD technology. In *35th International Electric Propulsion Conference*, IEPC-2017-339, Atlanta, GA, Oct. 8–12, 2017.
- [93] A. Boxberger, P. Jüstel, and G. Herdrich. Performance of 100 kW steady state applied-field mpd thruster. In *31st International Symposium on Space Technology and Science*, Matsuyama, Japan, June 3–9 2017.

- [94] T. Nakano, A. Ishiyama, Y. Shimizu, and K. Toki. Feasibility study of a low-power applied-field MPD arcjet. In *28th International Electric Propulsion Conference*, IEPC-2003-092, Toulouse, France, Mar. 17–21, 2003.
- [95] R. E. Jones and E. L. Walker. Status of large vacuum facility tests of MPD arc thruster. In *3rd Aerospace Sciences Meeting*, AIAA-66-117, New York, NY, Jan. 24–26, 1966. doi:10.2514/6.1966-117.
- [96] D. W. Esker, J. C. Kroutil, and R. J. Checkley. Radiation cooled MPD arc thruster. Technical Report NASA CR-72557/MDC-H296, McDonnell Research Laboratories, NASA Contract NAS 3-11518, July 1969.
- [97] V. Kim, T. Tikhonov, and S. Semenikhin. The first quarterly report on the stages ## 1-2 of the contract on the research studies no. NASA-4851 between RIAME MAI and NASA. Technical Report NASW-4851, RIAME MAI, Sept. 1994.
- [98] G. Popov, V. Kim, T. Tikhonov, S. Semenikhin, and M. Tibrina. The third quarterly report on the stages ## 3 “b” of the contract on the research studies no. NASA-4851 between RIAME MAI and NASA. Technical Report NASW-4851, RIAME MAI, Dec. 1996.
- [99] G. Popov, V. Kim, T. Tikhonov, S. Semenikhin, and M. Tibrina. The third quarterly report on the milestones (a) (3) and (a) (5) (C) of SoW of contract no. 960938 between RIAME MAI and JPL (items 6 and 7 of delivery schedule). Technical Report 960938, RIAME MAI, June 1996.